INVERSE MODELING FOR RETRIEVAL OF OPTICAL PROPERTIES OF SEA WATER AND ATMOSPHERIC AEROSOLS FROM REMOTE SENSING REFLECTANCE

CHANG CHEW WAI
(B.Sc (Hons), NUS)

A THESIS SUBMITTED
FOR THE DEGREEE OF DOCTOR OF PHILOSOPHY

DEPARTMENT OF PHYSICS

NATIONAL UNIVERSITY OF SINGAPORE

2007

Acknowledgement

I would like to express my sincere thanks and gratitude to numerous people who has helped me in the completion of this work. Without them, it would not be possible for me to finish this work.

First and foremost, I would like to thank my supervisors, Dr. Liew Soo Chin and Professor Lim Hock for their help, guidance, patience and encouragement along the path of this study.

To my colleguges, especially Mr Kwoh Leong Leong, the director at Center for Remote Imaging, Sensing and Processing for being so gracious and supportive of my research. To Dr. Santo V. Salinas Cortijo whom has encouraged. To the Ocean Colour teamates, Mr. He Jiang Cheng, Ms. Narvada Dewkurun, Ms. Alice Heng and Mr. Chew Boon Ning who have supported my study with much sweat and hard work.

To Tropical Marine Science Insitute (TMSI), Dr. Michael Holmes and Ms. Alice Ilaya Gedaria whom has been our collaborator in Ocean colour work for many years.

To Maritime and Port Authority (MPA) of Singapore for graciously permitting me to perform our field measurements (Permit No. 0174/05, 0070/06, 0157/07and 0153/05)

To my family and my church family, especially my brother, Chew Hung who has encouraged me relentlessly and helped me vet through the language of some parts of the thesis. And to my beloved wife, Laura who has selflessly supported me throughout the course of my research.

Last but not least to the ONE, Jesus who has been my Strength to lean on.

Contents

Summary

In this study an algorithm was developed to correct satellite imagery using cloud and shadow image features without the assumption of atmospheric optical properties as input for the visible bands. The method was able to retrieve optical properties of the atmosphere from hyperspectral satellite imagery. The atmospheric correction scheme was also able to perform atmospheric correction on high spatial resolution satellite (Ikonos) and high spectral resolution satellite (Hyperion) imagery. The atmospheric correction results from Ikonos data was validated by field measurements of water reflectance, while that from Hyperion was compared with corrected reflectance by well-known atmospheric correction scheme (TAFKAA).

An inversion algorithm was also developed to retrieve optical properties of both shallow and deep turbid waters in Singapore. The inversion algorithm uses spectral windows where light has the least transmittance in water to minimize the influence from the sea bottom. This algorithm was validated by in-situ measurements of absorption and scattering coefficients performed in the area of interests in the coastal waters of Singapore.

The algorithm to retrieve absorption and backscattering coefficients termed as IOPs was developed for the turbid coastal waters of Singapore. The algorithm was designed to retrieve IOPs in the presence of contributions from the sea bottom reflection to the remote sensing reflectance. The results were validated by in-situ measurements and further substantiated with a simulated dataset, which covers a wide range of IOPs and remote sensing reflectance of water. This dataset

has been used as a benchmark for evaluating retrieval algorithms for IOPs. The algorithm was also tested against one that used the full spectral window to evaluated the validity of using selected spectral window.

Optical properties of aerosols such as optical thickness and scattering transmittance, were retrieved from satellite imageries. An atmospheric correction scheme was used to correct the atmospheric effects by aerosol and gas absorption. The scheme made use of cloud and shadow features in high spatial and spectral resolution images, such as those collected with Ikonos and Hyperion satellite respectively. The radiances over cloud and shadows were used to derive the path radiances with minimal inputs, such as aerosol optical thickness and type.
This correction scheme is able to to derive water reflectance with small errors in spite of large uncertainties in radiometric calibrations for these two satellite instruments. Optical properties such as path reflectance, scattering transmittance and gaseous transmittance were also derived. The accuracy of these properties are directly related to how well the atmospheric correction has been performed. The validation for the Ikonos derived water reflectance was done by comparision with concurrent field measurements. For the validation of HYPERION data, it was compared to well known atmospheric correction schemes such as TAKFAA and one that corrects for Rayleigh scattering.

The optical properties of atmospheric transmittance, optical thickness and aerosol type were derived by fitting the derived path reflectance to look-up tables bearing these parameters from TAFKAA. The scattering and gaseous transmittance was also derived from the corrected cloud radiance, which is divided, by extra-terrestrial irradiance. The scattering transmittance obtained

from these two methods was compared for additional validation.

The algorithm was able to perform atmospheric correction without the assumption of atmospheric properties necessary with other methods that used cloud and shadow image features. In addition, the method was able to derive optical properties of the atmosphere such as optical thickness, aerosol type and transmittance. Optical properties of water were retrieved with a split window approach that avoids spectral bands where the sea bottom and the attenuating effect of shallow water contributes to the water reflectance.

List of Figures

List of Tables

List of Symbols

Symbol	Description	Units
$R_{rs}(\lambda)$	Above Remote Sensing Reflectance	Sr^{-1}
$L_w(\lambda)$	Water Leaving radiance	$Wm^{-2}Um^{-1}Sr^{-1}$
$E_d(\lambda)$	Downwelling Irradiance	$Wm^{-2}Um^{-1}$
$r_{rs}(\lambda)$	Underwater Remote Sensing Reflectance	Sr^{-1}
$\rho_w(\lambda)$	Water leaving reflectance	$-$
$F_d(\lambda)$	Extra-Terrestial Solar Irradiance	$Wm^{-2}Um^{-1}$
$L_{TOA}(\lambda)$	Top-of-atmosphere radiance	$Wm^{-2}Um^{-1}Sr^{-1}$
$L_{path}(\lambda)$	Path radiance	$Wm^{-2}Um^{-1}Sr^{-1}$
$T_s^{\uparrow}(\lambda)$	Upward Scattering Transmittance	$-$
$T_g^{\uparrow}(\lambda)$	Upward Gaseous Transmittance	$-$
$\rho_{TOA}(\lambda)$	Top-of-atmosphere Reflectance	$-$
$\rho_r(\lambda)$	Rayleigh Path Reflectance	$-$
$\rho_a(\lambda)$	Aerosol Path Reflectance	$-$
$a_w(\lambda)$	Absorption coefficient of pure water	m^{-1}
$a_g(\lambda)$	Absorption coefficient of CDOM	m^{-1}
$a_\phi(\lambda)$	Absorption coefficient of Phytoplankton	m^{-1}
$b_w(\lambda)$	Backscattering of Pure water	m^{-1}
$b_{bp}(\lambda)$	Backscattering of Suspended Particulates	m^{-1}
$L_c(\lambda)$	Cloud top radiance	$Wm^{-2}Um^{-1}Sr^{-1}$
$L_s(\lambda)$	Shadow area radiance	$Wm^{-2}Um^{-1}Sr^{-1}$

Chapter 1

Introduction

Satellite imagery over the ocean can be used to derive important optical properties of both the atmosphere and the ocean. The optical properties from the ocean can be used to relate to water quality parameters such as turbidity. The optical properties of the atmosphere such as optical thickness can also be used as a proxy to quantify the amount of suspended particulates in the atmosphere. Satellite imagery is able to offer large spatial coverage of these parameter and would be advantageous for monitoring purposes.

This thesis describes several several techniques to derive optical properties of the atmosphere and ocean using radiance measured by satellite sensors. This techniques are known as inverse modeling techniques where physical quantities can be inferred from the measured data, in this case the radiance from satellite imagery. Atmospheric effects were removed by an algorithm, which uses cloud and shadow image features without the assumption of atmospheric optical properties as input for the visible spectral bands. The method is able to retrieve optical properties of the atmosphere from hyperspectral satellite imagery. It should be pointed out that

the satellite sensors used here were not designed specifically for ocean colour remote sensing. Ocean viewing sensors usually demand high Signal to Noise Ratio (SNR) and accurate radiometric calibration. The atmospheric correction results from IKONOS data was validated by field measurements of water reflectance, while those from Hyperion data were compared with retrieved reflectances by a well known atmospheric correction scheme, such as (TAFKAA). The optical properties from ocean, in this case turbid coastal waters of Singapore, were derived. The retrieval algorithm used spectral windows where the bottom reflectance has least contribution to the measured signals. Validation was done with in-situ measurements of optical properties, such as the absorption and scattering coefficients measured in field trips made in Singapore waters. The method was also applied to atmospherically corrected hyperspectral images. The hyperspectral images were corrected by the cloud and shadow method developed in this thesis.

The main purpose of atmospheric correction of satellite imagery over the ocean is to derive the underlying water reflectance in the midst of the dominating path reflectance which arises from the multiple scattering of solar radiation by molecules and particulates in the atmosphere. In this work an atmospheric correction scheme was implemented on two types of satellite images, the IKONOS and Hyperion. IKONOS has high spatial resolution of 4 meters in the multispectral mode, Hyperion has high spectral resolution. While Hyperion has has 220 spectral bands covering the wavelength range of 400-2500 nm. For ocean colour remote sensing, it is sufficient to use the visible bands (400-900 nm) which have 10 nm bandwidth. Both sensors' radiometric calibration do not meet the requirements of 95 $\%$ accuracy for ocean colour application. It is known that with an accuracy of 95 $\%$, errors of up to 50 $\%$ would occur for retrieved water reflectance (Reinersman et al., 1998). The signal recorded from clouds and shadows present in

the images were used to derive atmospheric parameters that is needed to perform atmospheric correction. In this approach the values of the calibration constants were not used for channels in the visible spectral region but only in the near infrared region. The error incurred would be less and expected to be limited to the calibration error in this channel only.

The standard atmospheric correction schemes for ocean viewing sensors typically use huge lookup tables. The generation of these lookup tables requires extensive computations to build look-up tables (Gordon, 1978; Gordon & Clark, 1981; Gordon & Wang, 1994b). The look-up tables were constructed with numerous models of aerosol and atmospheric parameters as inputs to radiative transfer codes. In this work, minimal computations were used and most of the information needed to perform atmospheric correction is obtained from the image itself, hence relinquishing much of the need to have information input like aerosol type, amount and water vapour content. Furthermore, the optical properties of the atmosphere were derived from imaging data.

An algorithm was also developed here to retrieve inherent optical properties (IOPs) from water reflectance. Water reflectance is mainly influenced by IOPs such as absorption and backscattering coefficients. Numerous algorithms have been formulated to retrieve such properties from water reflectance (Lee et al., 1994, 1998a,b, 2002; Hoge & Lyon, 1996; Hoge et al., 1999a,b; Wang et al., 2005). Such algorithms usually use the whole visible spectral range to derive the IOPs. The usage of the whole visible spectra range in principle would allow IOPs over the whole spectra range to be derived. However when the water is shallow, the reflectance of the sea floor would contribute to the total reflectance measured.

In this study, an algorithm was implemented to tackle this problem by selecting spectral windows to minimize the influence from the sea bottom. A matrix inversion technique was used to derive the IOPs from these spectral windows. The algorithm developed in this study is also able to derive the IOPs over the whole visible spectral region despite the omission of spectral windows where light is more penetrable in water.

The algorithm to retrieve IOP was calibrated and validated using in situ measurements in the area of study in Singapore waters. In this case, islands with coral reefs were chosen and measurements were made around these areas. The parameters measured include absorption, attenuation and backscatttering coefficients. Radiometric measurements of the water leaving radiance were made and water reflectance was then derived based on standard protocols (Mueller et al., 2003). From the absorption and attenuation coefficients, the visibility could be estimated. Moreover from such measurements the dominant bio-optical components could be deduced. Such bio-optical components are :phytoplankton, CDOM , detritus and suspended sediments.

The measured optical parameters also provided a deeper understanding on the types of water in the area of study. It is of interest to examine how far the water sampled deviate from case 1 waters where most algorithms have been developed to retrieve optical properties over case 1 waters (O'Reilly et al., 1998). There are several definitions for case 1 waters and not all are uniform (Lee & Hu, 2006). However, it is generally known that the IOPs are largely dependent on the concentration for chlorophyll in phytoplankton (Preisendorfer, 1976). From the radiometric measurements, a simple evaluation was done to see if the waters sampled belonged to

the Case-1 type of waters. The resulting data was also made to achieve measurements (Werdell & Bailey, 2005) around the world and compare to the Singapore waters.

Chapter 2 gives a brief overview of the equations describing the radiative transfer of light through the atmosphere and ocean. An overview for the various IOPs and how they are related to the water leaving reflectance measured by satellite or handheld sensors will be covered.

In Chapter 3, experimental results from field measurements made in the area of interests are presented. It is found that that the water with large absorption coefficient also has large high backscattering coeffcient. The water leaving reflectance measured also exhibits a strong resemblance to water which has high absorption and backscattering coefficients. This was evident from the spectral shape and magnitude of the reflectance spectra. Two criteria were tested on field measured data to see if they belonged to Case-1 or Case-2 waters. A brief discussion would be made on the problems faced in the field measurements, which may provide useful information for other co-workers performing measurements in similar environment.

Chapter 4 describes the atmospheric correction scheme implemented on Hyperion and IKONOS images. The algorithm makes use of cloud, water and shadow image features in an image. The corrected reflectance from IKONOS images was compared to field measured reflectance as validation. For corrected Hyperion data , it was compared to data corrected by an atmospheric correction package, TAFKAA. It is a well known atmospheric correction code developed by NRL for hyperspectral remote sensing of ocean color (Gao et al., 2000; Montes et al., 2003; Mobley et al., 2005). Apart from correcting atmospheric effects, one of the important param-

eters that can be retrieved by the cloud and shadow method are atmospheric properties, such as atmospheric transmittance and aerosol type. In the implementation, two separate methods were used to derive the properties. One was fitting the derived path reflectance to TAFKAA generated data and obtaining the scattering transmittance, aerosol type and loading. The other was making use of the corrected cloud radiance and normalizing it with extraterrestrial solar irradiance. The properties derived by the two independent methods were compared and shown to coincide well, hence suggesting validity of these two approaches.

Lastly, chapter 5 discusses the retrieval of IOPs from the reflectance of shallow and deep waters by implementing the algorithm on spectral regions which is opaque to light. This algorithm is known as SWIM (Split-window inversion method). SWIM was applied to three different data sets. The first data-set was simulated and was used as a benchmark for many algorithms. This data set was reported recently in an IOCCG report (Lee, 2005). The data-set was generated by using a numerical radiative transfer code known as HYDROLIGHT, which had been used extensively for developing IOPs retrieval algorithm (Lee et al., 1998a,b; Albert & Mobley, 2003). Our algorithm was also implemented on field measured reflectance and was validated with in-situ measurements. The abililty of SWIM to reduce the contribution of sea floor reflectance and hence to increase the accuracy of IOPs retrieved was also evaluated. This was done by implementing an algorithm known as MIM (Matrix inversion method) even for spectral regions where light is not opaque. The errors of the retrieved IOPs were compared to the method developed in this thesis. The comparision was done on field measured data and HYROLIGHT simluated data which included a sea bottom at different depths. The comparision showed that SWIM is indeed able to retrieve IOPs with smaller errors. The atmosphere-corrected Hyperion

data was used for algorithm test.

Chapter 2

Remote Sensing of Sea Water Reflectance

2.1 Introduction

The radiance signal measured by a sensor on a satellite platform consists of light reflected by the earth surface and also light scattered from the atmosphere. In order to obtain the radiance emanating from the ocean, there is a need to correct for the effects of the atmosphere. The light signal that emanates from the ocean is also attenuated due to scattering and absorption by molecules and particulates. The first step in atmospheric correction is to compute the parameters describing such effects.

After the water leaving radiance has been derived from the total radiance measured at the top-of-atmosphere, water optical properties such as absorption and scattering coefficients can be retrieved. The optical properties of sea water are dependent on the contributions from the various optically active constituents. These various constituents are found at different abundance level and dependent on geographical and climatoral factors. Models used to retrieve these opti-

cal properties are usually built on semi-analytical equations that relate them to remote sensing reflectance (Gordon et al., 1988; Lee et al., 1998a; Gordon et al., 1988; Mobley, 1994, 1995).

2.1.1 Remote sensing reflectance of water

The radiance emanating from the surface of water is known as the water leaving radiance, $L_w(\lambda)$. The radiance is dependent on the amount of downwelling light at the surface and the reflectivity of the water. The remote sensing reflectance of water which would be used extensively in this thesis is defined as,

$$R_{rs}(\lambda) = \frac{L_w(\lambda)}{E_d(\lambda)} \tag{2.1}$$

where $E_d(\lambda)$ is the downwelling light at the surface of water. Due to transmittance across the water-air boundary, and the internal reflection effect, the water reflectance measured just below the water surface would be different from $R_{rs}(\lambda)$, which is the reflectance measured just above the water surface. $R_{rs}(\lambda)$ relates to the under water remote sensing reflectance $r_{rs}(\lambda)$ (Lee et al., 1998a; Gordon et al., 1988; Mobley, 1994),

$$R_{rs}(\lambda) = \frac{\zeta r_{rs}(\lambda)}{(1 - \Gamma r_{rs}(\lambda))} \tag{2.2}$$

where ζ and Γ are parameters dependent on viewing angle and water properties while $r_{rs}(\lambda)$ is the underwater remote sensing reflectance. The transmission of light from air to water and water to air is accounted for in Eq.(2.2) by ζ while the internal reflection of light from water to air is accounted for by $1 - \Gamma r_{rs}(\lambda)$. The term ζ is given as ,

$$\zeta = \frac{t^+ t^-}{n^2} \tag{2.3}$$

where t^+ is the diffuse transmittance of light from water to air and t^- is the diffuse transmittance of light from air to water. n is the refractive index of water.

The underwater remote sensing reflectance is related to the absorption coefficient of water $a_{tot}(\lambda)$ and backscattering coefficient $b_b(\lambda)$ (Gordon et al., 1988),

$$r_{rs}(\lambda) = g_0 u(\lambda) + g_1 u(\lambda)^2 \tag{2.4}$$

where

$$u(\lambda) = \frac{b_b(\lambda)}{b_b(\lambda) + a_{tot}(\lambda)} \tag{2.5}$$

The quadratic relation in Eq.(2.4) was obtained using monte carlo simulation (Gordon et al., 1988) and the terms g_0 and g_1 are dependent on the scattering phase function of the suspended particles in water (Lee & Carder, 2001). This quadratic form relating $r_{rs}(\lambda)$ and $u(\lambda)$ has been widely used (Lee et al., 1998a,b) in IOPs retrieval algorithms.

From Eq.(2.2) - Eq.(2.5), it can be seen how the absorption coefficient $a_{tot}(\lambda)$ and $b_b(\lambda)$ backscattering coefficient are related to water leaving radiance $L_w(\lambda)$. The water leaving reflectance is usually written as (assuming $L_w(\lambda)$ is lambertian),

$$\rho_w = \frac{\pi L_w(\lambda)}{F_d(\lambda)} \tag{2.6}$$

where $F_d(\lambda)$ is the extra-terrestial solar irradiance. The water reflectance can also be written as,

$$\rho_w(\lambda) = \pi R_{rs}(\lambda) \tag{2.7}$$

The next section will show how the water leaving radiance is related to the signal measured by the satellite sensor.

2.2 Signal Measured from space

The top-of-atmosphere (TOA) radiance, $L_{TOA}(\lambda)$, that is measured by the sensor over the ocean is a sum of several terms (Gordon & Wang, 1994a; Gordon, 1997),

$$L_{TOA}(\lambda) = T_g^{\uparrow}(\lambda)\left[T_s^{\uparrow}(\lambda)L_w(\lambda) + L_{glint}(\lambda)\right] + T_g^{\uparrow\downarrow}(\lambda)L_{path}(\lambda) \tag{2.8}$$

where $T_s^{\uparrow}(\lambda)$ is the upward transmittance due to atmospheric scattering, $T_g^{\uparrow}(\lambda)$ is the upward transmittance due to gaseous absorption and $T_g^{\uparrow\downarrow}(\lambda)$ the upward and downward transmittance due to gaseous absorption. The path radiance, $L_{path}(\lambda)$ results from scattering in the atmosphere. The component due to specular reflection of the direct sunlight is the term $L_{glint}(\lambda)$. For remote sensing purposes, the sunglint term is usually ignored as sunglint contaminated images are usually discarded due to the signal overwhelming the image (Gordon, 1997). It is to note that the transmittance terms are dependent on the sun and view angle of the sensor, the upward direction is dependent on the view angle while the downward on the sun angle.

A diagram of radiance measurement from a satellite is illustrated in Figure 2.1 where the different lines show the signal measured at the sensor. Ray 1 is depicted by $L_{path}(\lambda)$, ray 2 shows the sunglint reflected spectrally off the sea surface. Ray 3 shows light being scattered along the path as it reaches the water body and backscattered out of water and scattered along the way to the sensor. The scattering along the path as it reaches the sensor is termed as diffuse transmittance, $T_s^{\uparrow}(\lambda)$.

The water leaving radiance, $L_w(\lambda)$, emanating from the ocean is influenced by both environmental conditions and also the inherent optical properties (IOPs) of water. These environmental

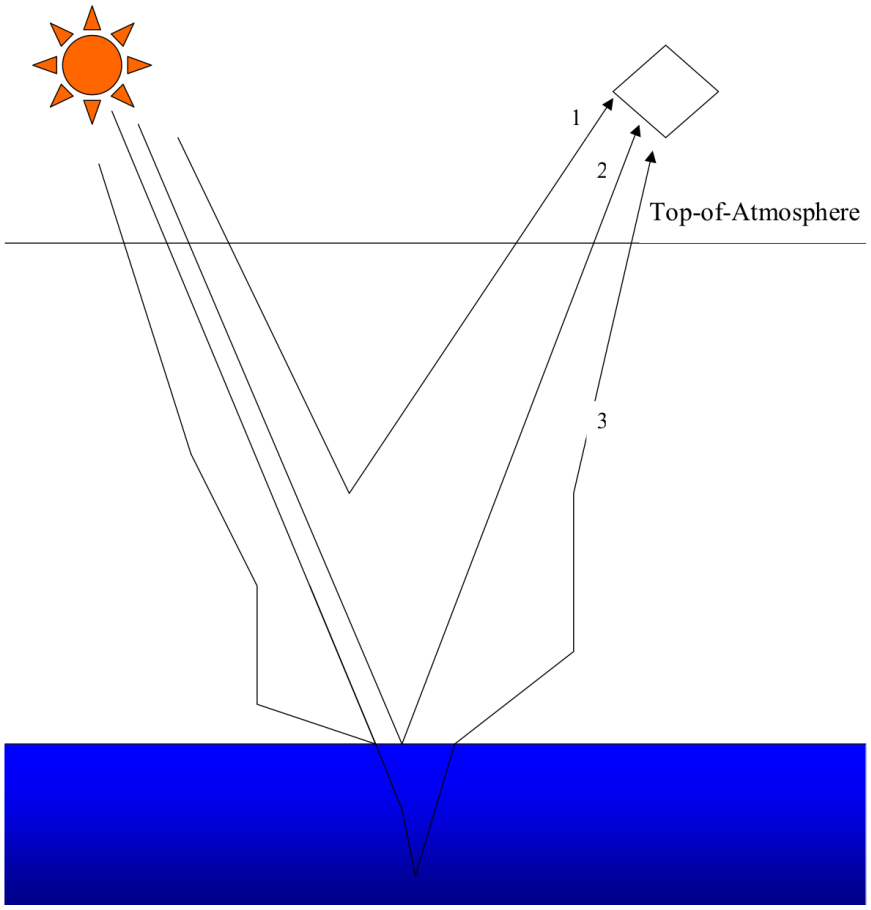

FIGURE 2.1: Schematic Diagram showing radiance measured by sensor

factors include wind speed, downwelling light, sea state, etc. One of the more notable during the field influcences was incoming storm or light drizzle which can alter the downwelling light field at the point of measurements. One of the challenges in remote sensing of water is to remove the signal which arises due to light interaction with the atmosphere. This procedure is called atmospheric correction. In most cases, the total signal consists largely of the path radiance, $L_{path}(\lambda)$. Typically 90 $\%$ of the signal is from $L_{path}(\lambda)$ and makes the task of deriving $L_w(\lambda)$ difficult. The problem is further complexed by several transmittance terms that need to be modeled correctly. Proper retrieval of the remaining 10 $\%$ involves accurate and extensive

modeling of the various terms in Eq.(2.8). This equation is usually converted into reflectance units before actual atmospheric correction is implemented. Each component will be briefly discussed in subsequent sections.

2.2.1 Conversion to reflectance

Radiance measured by the sensor is recorded in digital counts. The raw digital count is multiplied by a calibration factor to yield radiance. It is converted to reflectance units by,

$$\rho_{TOA}(\lambda) = \frac{\pi L_{TOA}(\lambda)}{F_d(\lambda)\cos(\theta_s)} \tag{2.9}$$

where $F_d(\lambda)$ is the extra-terrestial solar irradiance and $\cos(\theta_s)$ is the cosine of the sun angle , θ_s.

From Eq.(2.8), the TOA reflectance can be written as,

$$\rho_{TOA}(\lambda) = T_g^{\uparrow\downarrow}(\lambda)\left[T_s^{\uparrow\downarrow}(\lambda)\rho_w(\lambda) + \rho_{path}(\lambda)\right] \tag{2.10}$$

where,

$$\rho_w = \frac{\pi L_w(\lambda)}{T_s^{\downarrow} F_d(\lambda)\cos(\theta_s)} \tag{2.11}$$

and

$$\rho_{path} = \frac{\pi L_{path}(\lambda)}{F_d(\lambda)\cos(\theta_s)} \tag{2.12}$$

The total reflectance is affected by the error in calibration constant for each wavelength channel. A small 5% error in the calibration constant would imply a similar error in converting to reflectance units, hence propagating the errors to the retrieved water reflectance. For clear

ocean waters, water reflectance contributes about 10 % to the total reflectance. A small calibration error of about 5 % would translate to about 50 % error in the derived water reflectance (Reinersman et al., 1998).

2.2.2 Atmospheric transmittance

One of the parameters to be computed to perform atmospheric correction is the transmittance of the atmosphere. The transmittance reduced the amount of light reaching the earth surface and back to the sensor. The term $T_s^{\uparrow\downarrow}(\lambda)$ is the transmittance arising from scattering of light in atmosphere with air molecules and particulates. This term is determined by the amount of air molecules and aerosol particles in the atmosphere. The scattering due to air molecules is known as Rayleigh scattering.

The scattering transmittance can be computed using radiative transfer codes. Two examples are MODTRAN (Berk et al., 1987) and 6S (Vermote et al., 1997). The input parameters include the zenith and azimuth angle of both the sun and sensor. The particle size distribution of the aerosol and its optical properties such as refractive index are also needed. These properties of aerosol are needed to compute the phase function and the single scattering albedo using MIE scattering. Most radiative transfer codes have preset aerosol models such as Maritime, Urban and Continental at different relative humidity. The widely used size distribution and refractive index of these various types of aerosols could be found in Shettle & Fenn (1979). Apart from the types of aerosol, the concentration of the particulates are also needed. The concentration of aerosol particles determines the visibility in the sky. The concentration is related to the aerosol optical thickness at a reference wavelength (usually about 550 nm) is used in radiative transfer

codes to indicate the amount of aerosol present in the atmosphere.

In this study, the atmospheric correction algorithm implemented was able to obtain the aerosol type and optical thickness. This was done by using pre-computed transmittance and path reflectance values and fitted it to that derived from the implemented correction algorithm. The models used were coastal-A, Maritime and Urban at relative humidity of 80 %, 90 % and 98 %. The models used would not affect the atmospheric correction algorithm as such inputs are not needed for the implementation.

The other term $T_g^{\uparrow\downarrow}(\lambda)$ is due to the absorption of light by gaseous species such as water vapour, carbon dioxide, nitrous oxide, carbon monoxide and methane. The absorption due to various species can be computed by a line-by-line algorithm (Rothman et al., 2005) commonly implemented in various atmospheric correction codes (Gao & Davis, 1997; Gao et al., 2000; Montes et al., 2003). The concentration of each gaseous species is needed to compute the absorption or rather, the transmittance. The concentration of each species is quite constant apart from water vapour which varies temporally and spatially. In order to compute the transmittance, the concentration of water vapour and its vertical profile is needed. This makes the task of correcting water vapour absorption difficult. The transmittance with gaseous absorption features can be seen in Figure 2.2.

The transmittance was computed with the 6S radiative transfer code (Vermote et al., 1997). Atmospheric profiles of tropical, mid-latitude summer and mid-latitude winter standard atmospheres (McClatchey et al., 1972) were used to generate the transmittance. The profiles includes

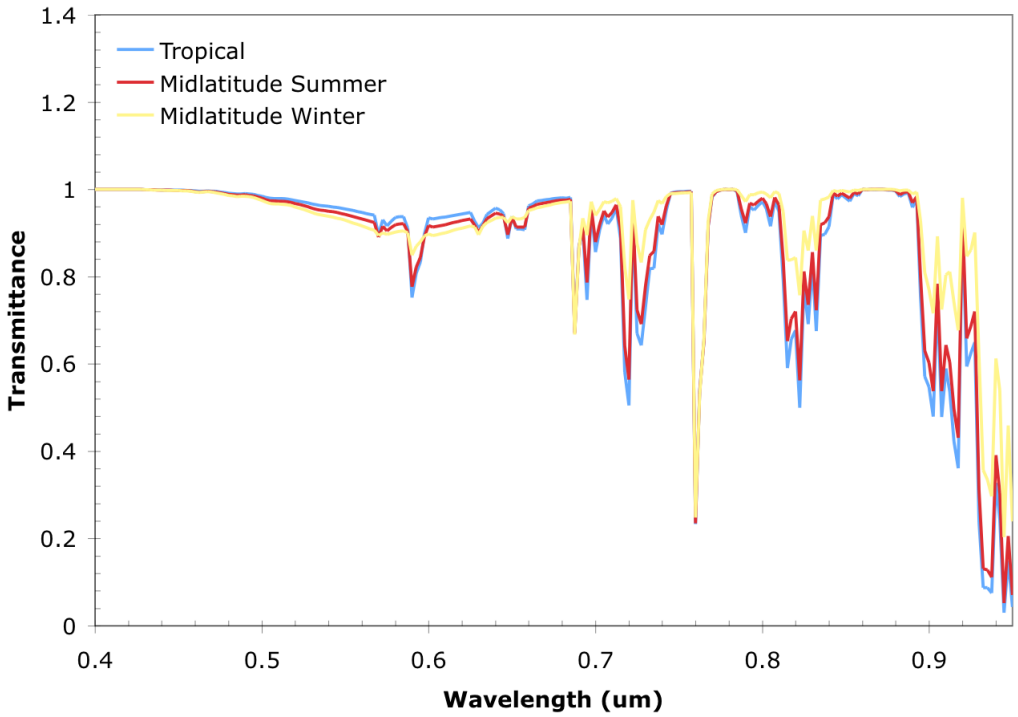

FIGURE 2.2: Atmospheric Transmittance due to gaseous absorption

the vertical distribution of air pressure, temperature, concentration of water vapour and ozone.

From Figure 2.2, variability could be seen for water absorption centered at 720, 860 and 920 nm. This variability is due to the different vapour amounts. Several methods use the band ratios of well known water vapour bands (reflectance) to derive the water vapour amount in the atmosphere(Gao et al., 1993; Kaufman & Gao, 1992).

2.2.3 Path reflectance

The path reflectance, $\rho_{path}(\lambda)$, consists of light that is scattered by air molecules and particulates in the atmosphere and it constitutes a huge part of the top-of-atmosphere reflectance. Path

reflectance can be written as a linear sum of several components (Gordon, 1997),

$$\rho_{path}(\lambda) = \rho_r(\lambda) + \rho_a(\lambda) + \rho_{ra}(\lambda) \tag{2.13}$$

where $\rho_r(\lambda)$ is the rayleigh path reflectance, $\rho_a(\lambda)$ is the aerosol path reflectance and $\rho_{ra}(\lambda)$ takes account of interaction between due to mixed layer scattering of aerosol and molecules. The concentration for molecules is quite constant hence the values of $\rho_r(\lambda)$ can be determined quite accurately (Vermote & Tanre, 1992; Gordon et al., 1988; Gordon & Wang, 1992).

This aerosol path reflectance $\rho_a(\lambda)$ varies temporally and spatially depending on the particle concentration and the aerosol model. In order to compute $\rho_a(\lambda)$ accurately to correct for atmospheric effects, the correct optical thickness and aerosol model need to be determined.

The term $\rho_{ra}(\lambda)$ can also be computed (Deschamps et al., 1983) with some radiative transfer codes like 6S (Vermote et al., 1997).

2.3 Atmospheric correction

The brief description of the various atmospheric terms pave the way to derive the water reflectance. The water reflectance can be obtained by rearranging Eq.(2.10),

$$\rho_w(\lambda) = \frac{\rho_{TOA}/T_g^{\uparrow\downarrow}(\lambda) - \rho_{path}(\lambda)}{T_s^{\uparrow\downarrow}(\lambda)} \tag{2.14}$$

The main atmospheric term to be modeled is the $\rho_{path}(\lambda)$ term since it contributes significantly to the total reflectance. One of the difficulties is to be able to estimate the correct aerosol model and optical thickness in order to model the term $\rho_{path}(\lambda)$. Usually aerosol models from Shettle

& Fenn (1979) are used as input models for aerosols.

The development of atmospheric correction schemes over the ocean stems from the first ocean colour sensor, CZCS back in 1977. The sensor was launched upon the possibility of retrieving chlorophyll concentration of phytoplankton from measurements of upwelling light radiance (Clarke et al., 1970). The atmospheric correction implemented (Gordon, 1978) on CZCS assumes single scattering and the water leaving radiance to be negligible at near infra-red spectral bands. The reflectance at these spectral bands were fitted to pre-computed path reflectance corresponding to different aerosol models and optical thickness.

With a similar approach, the atmospheric correction (Gordon & Wang, 1994b) was implemented on SEAWIFS and MODIS which have higher SNR as compared to the CZCS and additional waveband at 860 nm. The same assumption is that, the signal from the water is zero at longer wavelengths due to strong absorption by water. This is also known as the dark pixel assumption. For the implementation in SEAWIFS and MODIS, multiple scattering of light with aerosol was assumed. From the two channels centered at 760 nm and 860 nm, the ratio of these two channels was used to estimate the aerosol type and also optical thickness from a pre-generated database of aerosol models. With that, the path reflectance and the scattering transmittance were obtained from a lookup table which was then used for atmospheric correction.

The dark pixel assumption, however, is not valid where highly backscattered water is present. The signal from the water surface is not zero and would result in errors due to atmospheric correction (Siegel et al., 2000; Hu et al., 2000). There are methods implemented to overcome

this problem. For Case-1 water where the optical properties are dependent on chlorophyll, an iterative method is used where initial values of chlorophyll concentration is derived and used to obtain the water leaving reflectance at the NIR, on the assumption that the water leaving reflectance is zero. In this initial estimation the aerosol model and optical thickness is derived. After which the estimated chlorophyll concentration is used to compute the water leaving reflectance at the NIR spectral bands and the optical thickness was derived with the consideration of this contribution from water. This process is repeated until the values obtain for chlorophyll concentration converged (Siegel et al., 2000).

Another approach uses the area of an image where the water leaving reflectance is very small to derive the aerosol model using the SEAWIFS approach. The derived model was used as an input to the algorithm. With this model the optical thickness and backscattering coefficient of water were used to fit the signal from areas of the image where the water leaving reflectance is not zero (Hu et al., 2000).

In recent years, with the advent of hyperspectral sensors such as Hyperion and AVIRIS, atmospheric correction schemes are needed to retrieve the water reflectance from the imagery. There are many methods developed over the years to perform atmospheric correction of hyperspectral images. TAFKAA has been widely used for hyperspectral images in littoral zones and coastal waters (Montes et al., 2003; Davis et al., 2002). The earlier version of TAFKAA is based on ATREM (Gao et al., 1997) which was built from 6S (Vermote et al., 1997) and does not take into account of surface effects. The recent version takes into account of surface effects (Ahmad & Fraser, 1982) which includes surface glint and wind roughened surface. This version of

TAFKAA is used in this thesis. TAFKAA uses pre-ran look-up tables of atmospheric optical properties such as path reflectance, scattering transmittance and albedo. These parameters were computed with inputs, such as, aerosol model, optical thickness and wind speed.

The look-up tables employed in various atmospheric scheme available in TAFKAA were selectable by user options. The atmospheric correction could be implemented on a pixel by pixel basis, by assuming that the signal from certain bands in the NIR arises from atmospheric scattering only. The signal was fitted to pre-computed path reflectance and was used to fit this reflectance in the NIR. It also allows user intervention to key in aerosol model, optical thickness, wind speed and concentration of atmospheric gases. In this study, TAFKAA will be used as a benchmark to estimate the atmospheric correction scheme employed for HYPERION.

In this thesis, an atmospheric correction algorithm is developed which uses radiance detected over cloud and shadow areas in satellite imagery. The algorithm is able to derive the water reflectance without any assumptions of atmospheric conditions such as optical thickness and aerosol model. Furthermore, the conversion to top-of-atmosphere is not required in the visible spectrum. The algorithm is also able to derive optical properties of the atmosphere such as aerosol model, path reflectance, optical thickness and transmittance from hypersepctral sensor. The atmospheric correction would be performed over two sensors, one which is of high spatial resolution sensor (Ikonos) and the other a hyperspectral sensor (HYPERION).

2.4 Inherent Optical Properties

As shown in earlier sections, the water leaving radiance, $L_w(\lambda)$, is dependent on the the absorption and backscattering coefficients of water. These coefficients are known as inherent optical properties of water and affect the radiance emanating from the surface of waters. Inherent optical properties are not affected by environmental conditions (Preisendorfer, 1976). The absorption and backscattering coefficients are affected by the concentration of various constituents in water such as CDOM(Coloured Dissolved Organic Matter), detritus, phytoplankton and suspended sediments. Each constituent has its own absorption and backscattering coefficient. The optical properties of water is usually expressed as a linear sum of the contributions from various constituents including water itself.

2.4.1 Absorption coefficient of Seawater

Absorption of light by sea water is determined by various optically active constituents. The total absorption coefficient, $a_{tot}(\lambda)$, is a linear combination of the various absorption coefficients of CDOM $a_{cdom}(\lambda)$, detritus $a_{det}(\lambda)$, phytoplankton, $a_{\phi}(\lambda)$ and water $a_w(\lambda)$ itself. The absorption of sea water is given as a linear sum of the various components (Prieur & Sathyendranath, 1981; Roesler et al., 1989; Carder et al., 1991),

$$a(\lambda) = a_w(\lambda) + a_{\phi}(\lambda) + a_{det}(\lambda) + a_{cdom}(\lambda) \tag{2.15}$$

To accurately describe the absorption properties, especially the spectral variation over the wavelength of 400 nm - 800 nm, thorough in-situ investigation has to be made over area of interests.

2.4.2 Absorption coefficient of water

The absorption of pure water has been measured extensively by many co-workers in the field. In recent years, measurements were made with integrating cavity absorption meter (Pope & Fry (1997); Fry et al. (1992)), underwater spectroradiometer (Baker & Smith (1982)) and photothermal technique (Sogandares & Fry (1997)). Measurements from Pope & Fry (1997) were often used in the field of ocean optics. The absorption of water is shown in Figure 2.3.

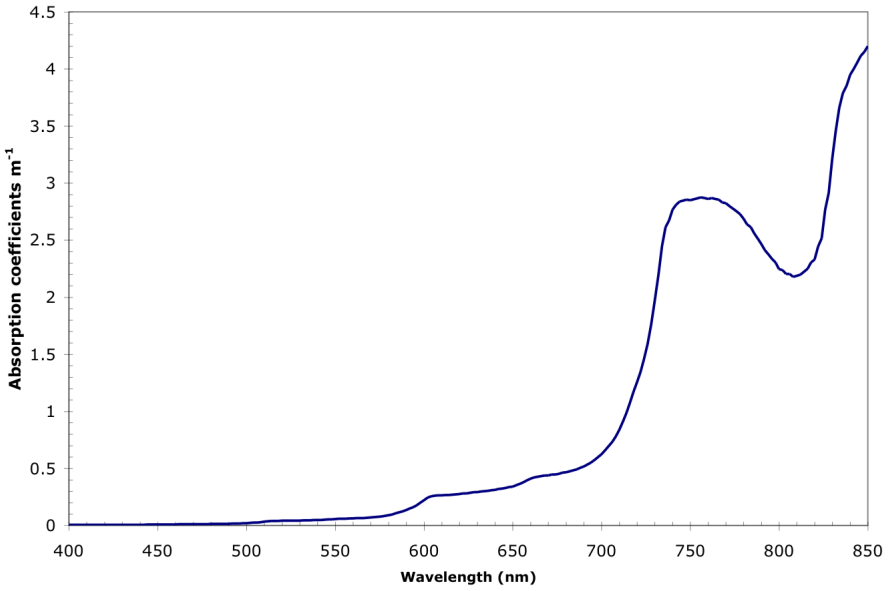

FIGURE 2.3: Absorption coefficient of Water

Water has very low absorption for wavelengths less than 600 nm hence, the absorption of the various bio-optical components are more important for this wavelength range. The absorption of water starts to increase dramatically after 700 nm. The high values of water absorption imply

that the light that will be backscattered would be negligible at longer wavelengths.

2.4.3 Absorption coefficient of Phytoplankton

Phytoplankton are living organisms that undergo photosynthesis by light absorption in visible spectral region. The absorption is most pronounced at the blue and red region of the visible spectrum.

Since phytoplankton are living organisms, their absorption properties are highly dependent on their physiological state. Their physiological state affects the absorption properties of the phytoplankton by packaging effect (Morel & Bricaud, 1981; Roesler et al., 1989). The absorption properties are characterized by the specific absorption coefficient and is a measure of the absorption of phytoplankton per unit volume per unit concentration.

One such model for absorption by phytoplankton (Lee, 1994) is expressed as,

$$a_\phi(\lambda) = a_\phi(440)a_0(\lambda) + a_\phi(440)\ln(a_\phi(440))a_1(\lambda) \tag{2.16}$$

where $a_0(\lambda)$ and $a_1(\lambda)$ are basis functions. $a_\phi(440)$ is a measure of chlorophyll concentration in water. The model allows adjustments to be made to the absorption of phytoplankton due to self shading effect by the second term in the equation. This model has been used quite extensively, especially in the generation of test data for algorithm development (Lee, 2005). Absorption spectra of phytoplankton generated using this model are illustrated in Figure 2.4

2.4.4 Absorption coefficient of CDOM and detritus

CDOM is dissolved organic matter while detritus is non-living inorganic particulate material. They both exhibit high absorption in the UV region. In coastal waters, the main source of

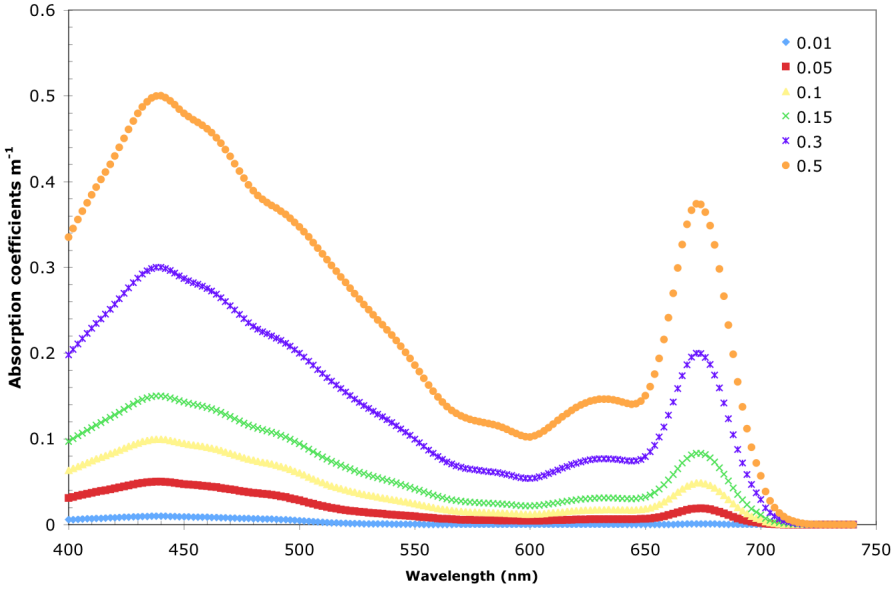

FIGURE 2.4: Absorption coefficients of phytoplankton. The spectra are generated with different values of $a_\phi(440)$ at 0.01, 0.05, 0.10, 0.15, 0.3 and 0.5 m^{-1}

CDOM and detritus not only comes from the decay of phytoplankton but also from inland fresh water draining into the ocean. Their absorption coefficients decrease exponentially with wavelength which is expressed (Bricaud et al., 1981) as,

$$a_g(\lambda) = a_g(440)e^{s(440-\lambda)} \tag{2.17}$$

where S is the spectral slope which governs the exponential decrease with respect to wavelength. For retrieval purposes, the contribution from CDOM and detritus are usually expressed together as one term as shown in Eq.(2.17) as both exhibit similar exponential spectral decay. Studies have been conducted extensively (Bricaud et al., 1981; Zepp & Schlotzhauer, 1981; Højerslev & Aas, 2001) throughout the world to find the value of S which characterize the spectral variation of this term. Many independent studies (Zepp & Schlotzhauer, 1981; Bricaud

et al., 1981; Højerslev & Aas, 2001) suggested values between 0.014 nm $^{-1}$ and 0.015 nm $^{-1}$ for the value of S. However, other values of S were also reported from around the world suggesting that values of S are dependent on the location where it was sampled.

2.5 Backscattering coefficient

The backscattering coefficient of sea water depends on the amount of phytoplankton and suspended sediment present. It governs the amount of light scattered out of the water. Light scattering in oceanic waters is mostly forward biased and typically 1.803 $\%$ is backscattered measured (Petzold, 1972) for coastal waters. The total backscattering coefficient is a linear sum of the backscattering of water and suspended particulates in water and is given as,

$$b_b(\lambda) = b_{bw}(\lambda) + b_{bp}(\lambda) \tag{2.18}$$

where $b_{bw}(\lambda)$ is the backscattering of water and $b_{bp}(\lambda)$ is the backscattering coefficient of suspended particles.

A higher backscattering coefficient would mean that the reflectance of the water is higher as more light scatters out of the water. For coastal water, the backscattering is usually higher as compared to open waters due to higher concentration of suspended sediment.

2.5.1 Backscattering coefficient of Water

The backscattering coefficient of water can be seen in Figure 2.5 whereby the magnitude is very low and consists of a small part of the total backscattering of coastal water.

The backscattering of water is only a small apart of the total backscattering for coastal waters.

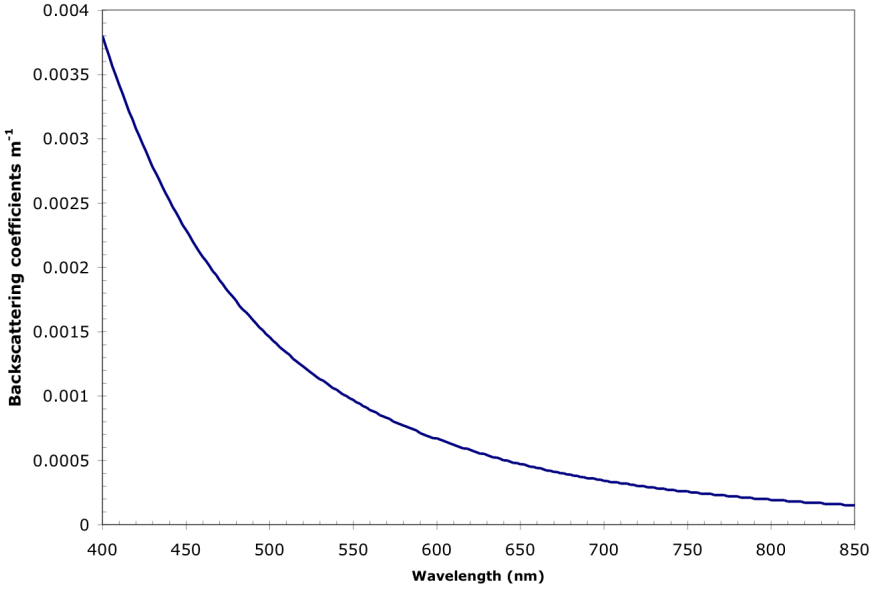

FIGURE 2.5: Backscattering coefficient of water

2.5.2 Backscattering coefficient of suspended particulates

Apart from the absorptive effects of various constituents in water, the suspended particulates in water such as phytoplankton and sediment affects the signal of the water leaving reflectance. The backscattering coefficient is usually modeled by (Morel & Prieur, 1977),

$$b_{bp}(\lambda) = b_{bp}(550)(\frac{550}{\lambda})^{Y} \tag{2.19}$$

where Y governs the spectral behaviour of $b_{bp}(\lambda)$ and $b_{bp}(550)$ is the backscattering coefficient of suspended particles at 550 nm.

2.6 Case-1 water

Sea Waters are classified into either Case-1 or Case-2 waters according to their optical properties (Morel & Prieur, 1997). For Case-1 water, the inherent optical properties are largely dependent on the concentration of phytoplankton (Preisendorfer, 1976). The absorption and backscattering coefficients are paramterized by the concentration of chlorophyll found in water (Gordon & Morel, 1983; Sathyendranath & Arnone, 2000). For example, the absorption coefficient of phytoplankton at 440 nm (Prieur & Sathyendranath, 1981),

$$a_{\phi}(440) = 0.06C^{0.65} \tag{2.20}$$

where C is the concentration of chlorophyll-a.

Backscattering coefficient of suspended particles (Gordon & Morel, 1983) is,

$$b_{bp}(\lambda) = B[chl-a]^{0.62}\frac{550}{\lambda} \tag{2.21}$$

where B represents empirical values of 0.3,1.0 and 5.0, ranging from open to turbid waters. These relationships are empirical and can be used to compute optical properties of water.

For Case-1 waters, the backscattering is expressed as a function of the concentration of chlorophyll in phytoplankon. However in the remote sensing of Singapore coastal waters, the value of $b_{bp}(550)$ was set as a parameter to be retrieved hence, decoupling the dependency on C as the central parameter for the IOPs for various constituents found in water.

For Case-2 waters, the IOPs of water are not solely determined by the amount of C but on the various constituents optical properties. In later chapters that the waters surveyed in field trips

are Case-2 Waters, the amount of C was found in small amounts as evident from the small absorption of phytolplanton. As such, the absorption coefficient of phytoplankon, CDOM and detritus were set as parameters to be retrieved from the measured $R_{rs}(\lambda)$ instead of using C as the key parameter to be retrieved.

Chapter 3

Quantifying Optical Properties of Surveyed Waters

3.1 Introduction

This project aims to develop algorithms for retrieval of water optical properties from remote sensing reflectance applicable to turbid coastal sea waters. Several field trips were conducted in Singapore coastal waters to collect field data. The use of field-measured data were for testing and validating the algorithms. Though ultimately the algorithms would be applied to reflectance data measured by sensors on satellite platforms, the use of field-measured reflectance spectra would allow testing and validating of the retrieval algorithms without having to worry about the influences of the intervening atmosphere that would be present in satellite data. The field data collected include the above-surface water reflectance measured by a hand-held spectroradiometer and the absorption and scattering coefficients of sea water measured by a submersible absorption-attenuation meter.

The field measured water reflectance was found to be bright and the total scattering and backscattering coefficients measured concurred the high values found. The measured absorption is indicative of high CDOM loading and little phytoplankton absorption. This conclusion came from the low absorption peak at 675 nm which is characteristic of phytoplankton absorption. The exponential decreasing spectral behaviour of the absorption coefficients measured indicates the presence of CDOM absorption. A further decomposition of the total absorption into phytoplankon and CDOM components further indicate that the absorption is indeed dominated by CDOM with little contribution by phytoplankton. The field measured reflectance was also used to determine the deviation of the Singapore coastal waters from Case-1 type waters.

3.2 Study Site

The field trips were conducted in the vicinity of two islands, Pulau Hantu and Pulau Semakau which are located about 10 nautical miles southwest of the Singapore main island see Figure 3.1. Pulau Hantu is a favorite site for diving while Pulau Semakau has been developed into an off-shore landfill. P. Semakau was originally a lush mangrove island, and most of the island's natural environment and biodiversity have been preserved. The water depth in the study site ranges from less than 1 m to 20 meter. This range of water depth is especially useful in the study of the effects of the bottom reflectance on the retrieval algorithms.

Pulau Hantu consists of of two islands separated by a lagoon. The lagoon is about 100 m wide and the bottom is mostly sandy. The waters is relatively clear near Pulau Hantu. The sea bottom

is visually discernible where the water depth is 3 m or less. The visibility of the water near Pulau Semkau is considerably lower. Typically, the absorption coefficient measured at Pulau Hantu is about 0.3 m^{-1} to 0.4 m^{-1} while that at Pulau Semakau is about 0.7 m^{-1} to 1.0 m^{-1}. The wide range of water depth will provide dataset that will be useful to test IOPs retrieval algorithms, especially in this study, where spectral windows were selected to minimize the bottom effect.

Six field trips were conducted between 2005 to 2006. There are 24 sampling sites where coninc dental IOPs and water reflectance measurement are made. However there are only 22 sites where water reflectance measurements coincides with IOPs measurements. There were some points that were sampled on the first field trip, which is located at cyreene reefs. The location at this point is marked out by the yellow square in Figure 3.1(a). However they will not be included in this section for discussion but the IOPs and reflectance would be used for the validation of the IOP retrieval algorithm.

The details of the position , water depth and time of sampling are shown.

TABLE 3.1: Details of field measurements P.Hantu

S/N	Date, Time (GMT +8)	Lat	Long	Depth (m)
H1A	2005-10-18, 9:56	N.A	N.A	11
H1B	2005-10-18, 10:28	1.2276 N	103.7489 E	2.5
H1C	2005-10-18, 10:53	1.2236 N	103.7508 E	1.9
H1D	2005-10-18, 10:53	1.2244 N	103.7466 E	2.7
H1E	2005-10-18, 11:30	1.2231 N	103.7498 E	3.5
H2A	2006-03-10, 10:37	1.2247 N	103.7468 E	1.3
H2B	2006-03-10, 11:32	1.2220 N	103.7476 E	24.0
H2C	2006-03-10, 15:33	1.2229 N	103.7499 E	9.4
H2D	2006-03-10, 16:24	1.2271 N	103.7513 E	8.0
H3A	2006-05-16, 10:41	1.2292 N	103.7498 E	17.0
H3B	2006-05-16, 13:36	1.2231 N	103.7509 E	3.0

The sampling sites (S/N) shown in Table 3.1 and Table 3.2 are labeled according to the sampling locations for which they were sampled. For example, S1A represents the first field trip for P.Semakau while H1A represents the first trip at P. Hantu. For some of the points the Latitude and Longitude were not available and hence labeled as N.A. The Sonar depths are sounded and given in the column for depth. The points at cyreen reefs are shown Table 3.3.

TABLE 3.2: Details of field measurements P.Semakau

S/N	Date, Time (GMT +8)	Lat	Long	Depth (m)
S1A	2005-06-10, 12:35	1.2080 N	103.7540 E	3.0
S1B	2005-06-10, 13:00	N.A	N.A	5.4
S1C	2005-06-10, 15:05	1.2141 N	103.7485 E	6.0
S2A	2005-06-30, 10:16	1.2036 N	103.7546 E	5.0
S2B	2005-06-30, 10:45	1.2099 N	103.7516 E	5.0
S2C	2005-06-30, 11:07	1.2050 N	103.7536 E	6.7
S2D	2005-06-30, 11:30	1.1985 N	103.7570 E	10.0
S2E	2005-06-30, 14:15	1.2097 N	103.7554 E	5.5
S2F	2005-06-30, 14:42	1.2068 N	103.7527 E	5.0
S2G	2005-06-30, 15:08	1.2174 N	103.7548 E	4.7
S2H	2005-06-30, 15:25	1.2140 N	103.7540 E	3.0
S3A	2005-07-29, 15:25	1.2080 N	103.7533 E	3.9
S3B	2005-07-29, 15:42	1.2137 N	103.7568 E	2.0

TABLE 3.3: Details of field measurements Cyreene Reefs

S/N	Date, Time (GMT +8)	Lat	Long	Depth (m)
M1A	2005-06-10, 10:00	1.2553 N	103.7549 E	10.1
M1B	2005-06-10, 10:32	1.2559	103.7545 E	9.2
M1C	2005-06-10, 10:59	1.2586 N	103.7658 E	6.8

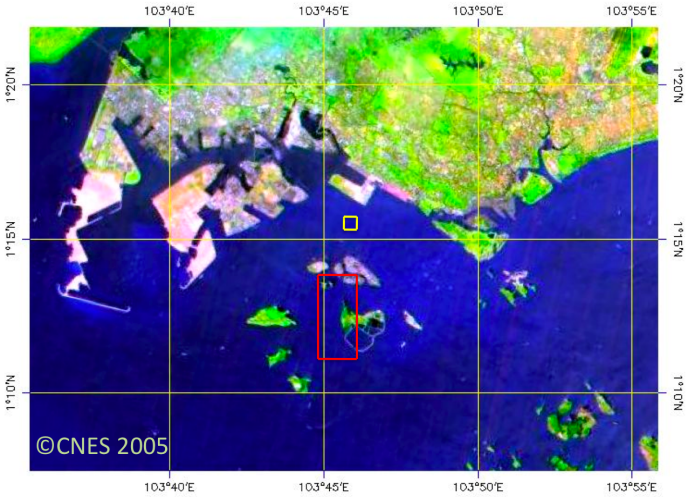

(a) Location of Study Site

(b) Satelite Image of Study Site

FIGURE 3.1: Locations of Study Site

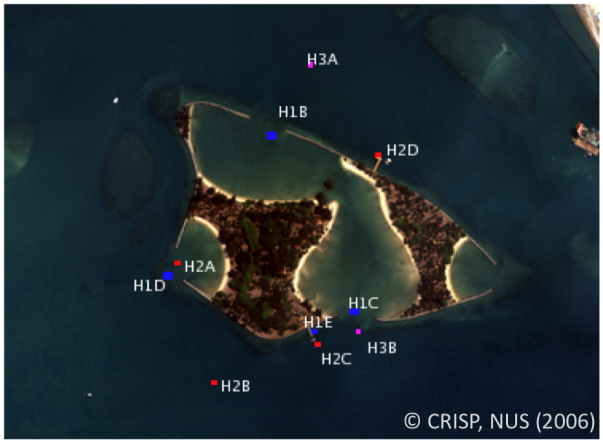

(a) Field points at P.Hantu

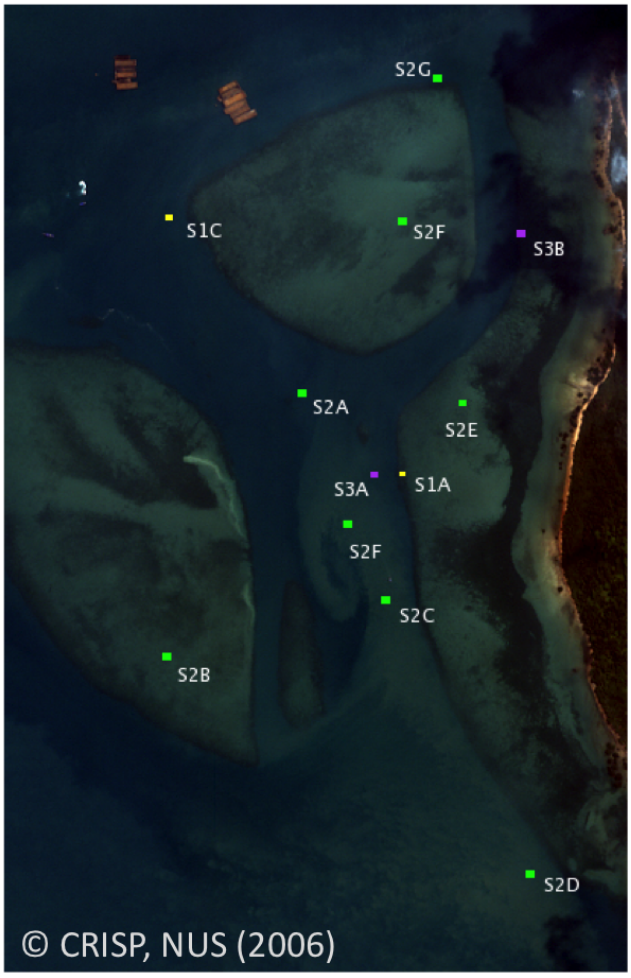

(b) Field points at P.Semakau

FIGURE 3.2: Field Measured points

3.3 Measurement of water reflectance

Field trips were conducted usually between 9 am to 12 noon, and resumed from 1.30 pm to 5pm to avoid measurements when the sun zenith angle is less than 20^0 as recommended (Mobley, 1999). This is to reduce contamination due to sunglint and to minimize the variability of the reflected skylight from the sea surface.

A hand-held spectroradiometer (GER1500, Spectra Vista Inc.) was used to measure the upwelling radiance, $L_u(\lambda)$, emanating from the water surface. The spectroradiometer consists of a silicon based detector array with 512 channels. The spectral range of the equipment is from 350 nm to 1050 nm with a nominal band width of 1.5 nm. The measured raw data is digitized to 16 bits. The spectrometer is fitted with a 3^0 field of view fore-optics. The measured radiance $L_u(\lambda)$ also includes the sky radiance $L_{sky}(\lambda)$ reflected off the water surface,(Mobley, 1999; Koepke, 1984; Fougnie et al., 1999; Austin, 1974),i.e

$$L_u(\lambda) = L_w(\lambda) + \rho L_{sky}(\lambda) \tag{3.1}$$

where $L_u(\lambda)$ is the upwelling radiance emanating from the water surface. ρ is the proportionality factor that relates the radiance measured when the detector views the sky to the reflected sky radiance measured when the detector views the sea surface (Mobley, 1999) .

The remote sensing reflectance of water (Mobley, 1999) is defined as

$$R_{rs}(\lambda) = \frac{L_w(\lambda)}{E_d(\lambda)} \tag{3.2}$$

where $E_d(\lambda)$ is the downwelling irradiance at the surface of water.

The remote sensing of water is given,

$$R_{rs}(\lambda) = \frac{L_u(\lambda)}{E_d(\lambda)} - \rho\frac{L_{sky}(\lambda)}{E_d(\lambda)} \tag{3.3}$$

In order to obtain $R_{rs}(\lambda)$, the values of $L_u(\lambda)$, $L_{sky}(\lambda)$, $E_d(\lambda)$ and ρ need to be measured or estimated. In field trips, $L_u(\lambda)$, $L_{sky}(\lambda)$ and $E_d(\lambda)$ were measured. The measurements were made with the boat positioned between 90^0 (Carder & Steward, 1985; Lee et al., 1997) to 135^0 (Mobley, 1999; Fougnie et al., 1999) relative to the sun azimuth angle. However this was typically diffcult as the boat though anchored was subjected to strong underlying tidal currents. The measurements of $L_u(\lambda)$ from the water surface were made with sensor view angle of about 30^0 (Carder & Steward, 1985; Lee et al., 1997) to give $L_u(\lambda)$ on a diving platform which provides easy and close access to the sea water, likewise, with the same angle to the vertical, $L_{sky}(\lambda)$ was measured. $E_d(\lambda)$ was not measured directly but the measurements were made on a white lambertian plate (Spectralon^{TM}) with known reflectance as a reference. The radiance reflected off the reference plate and is subjected to the same irradiance is measured. The irradiance is then given by (Mueller et al., 2003; Mobley, 1999),

$$E_d(\lambda) = \frac{\pi L_g(\lambda)}{R_g} \tag{3.4}$$

where $L_g(\lambda)$ is the radiance measured from white reflectance plate and R_g is the reflectance of the plaque which is 0.97. The measurements are illustrated in Figure 3.3

In order to derive $R_{rs}(\lambda)$, ρ needs to be estimated and this term is dependent on environmental conditions such as cloud cover, wind speed, sea state and also downwelling light field at the sea

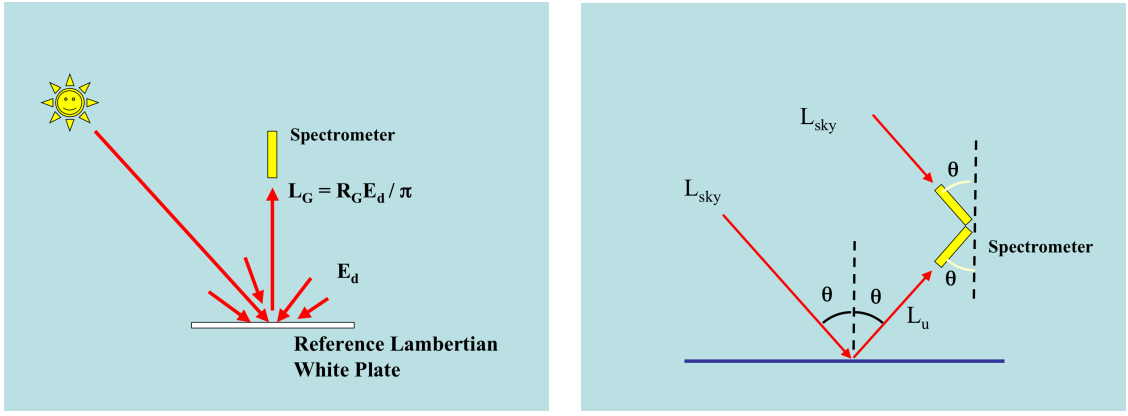

(a) Measurement of $E_d(\lambda)$ (b) Measurement of $L_u(\lambda)$

FIGURE 3.3: Schematic Diagram of Measurements

surface (Mobley, 1999). The value of ρ is reported to range from 0.02 to 0.028 for view angle of 30 to 40 under uniform sky radiance distribution (Austin, 1974). Other studies recommend a wide range of values to be used under different environmental conditions. This term was found to be ranging from 0.026 to 0.043 for view angle of 40^0 under different wind conditions (Mobley, 1999). In this study a value of 0.022, following the recommendation by SeaWifs protocol (Mueller & Austin, 1995) was used. For a relatively calm sea surface, this value is also the theoretical Fresnel reflectance for a view angle of 30^0.

At each sampling site, seven or more sets of $L_u(\lambda)$, $L_{sky}(\lambda)$ and $L_G(\lambda)$ were acquired. The averaged values were used to derive $R_{rs}(\lambda)$ according to Eq.(3.3). For each set of spectrum, the outliers were removed by rejecting values which differed from the mean value by 5%. Typical measurements are shown in Figure 3.4.

In most cases even with the removal of the reflected skylight from the total signal to yield $R_{rs}(\lambda)$ there is still residual remaining (Mobley, 1999). This is due to in exact estimation

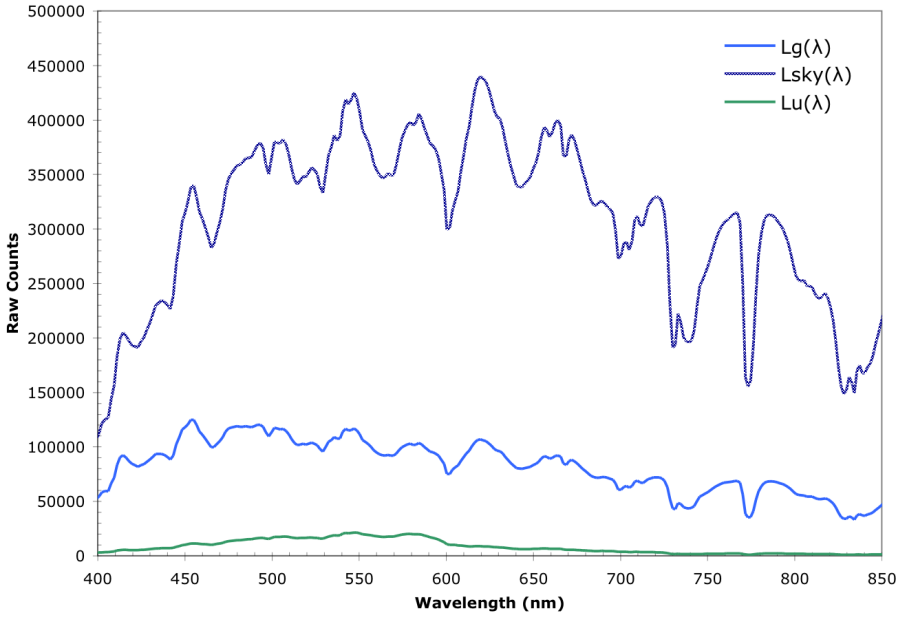

FIGURE 3.4: Typical radiance measurements obtained

in ρ which is highly variable since the water surface reflecting the sky light is usually not perfectly smooth. There has been recommendations of zeroing the residual amount by simply subtracting a constant value from the reflectance (Carder & Steward, 1985). The assumption is that the residual amount is spectrally flat and that the water is dark at wavelength above 750 nm. Any non-zero reflectance value at 750 nm can be considered to be the residual value and this can be subtracted to yield true reflectance. However for turbid waters, or waters with high backscattering, this method may not work (Sydor & Arnone, 1997; Sydor et al., 1998; Lee et al., 1997) since the $R_{rs}(\lambda)$ is not necessarily zero at 750 nm. There has been recommendations to use longer wavelengths for the residual offset (Hooker et al., 1999). In this work the longest wavelength possible was used to perform the residual offset. Because of the large noises for

bands beyond 820 nm, the residual offset was performed at 820 nm.

3.4 In-situ measurements of absorption and attenuation coefficients of water

The inherent optical properties (IOPs) of sea water measured during the field trips were the absorption and attenuation coefficients. These parameters were measured using a submersible absorption-attenuation meter (AC-9, WetLabs) at 9 wavelengths ranging from 412 nm to 715 nm. The scattering coefficient is subsequently obtained from the difference between the attenuation and absorption coefficients. The AC-9 is mounted in a cage together with a pump which draws sea water into the two measuring tubes of the instrument (Figure 3.5). The cage is attached to a 10-m rope for deployment into the water. There is also an additional safety line attached directly to the AC-9 equipment. A backscattering meter (BB2F, WetLab) for measuring backscattering coefficient was also mounted in the casing together with the AC-9. However, the BB2F malfunctioned most of the time and therefore was not used subsequently in this study.

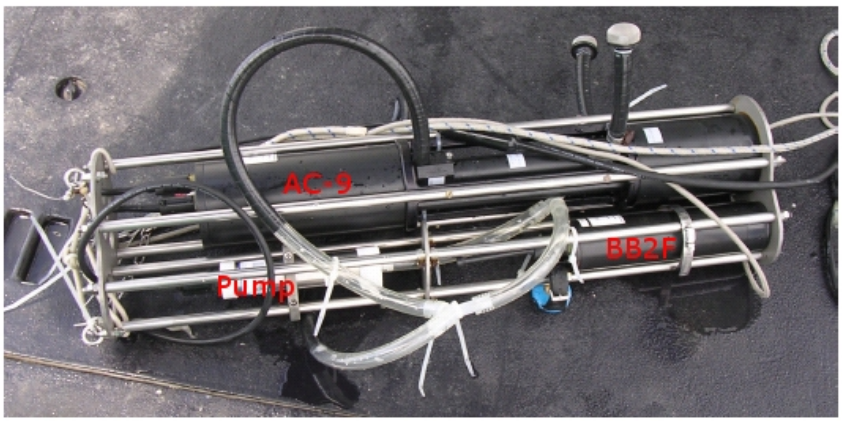

FIGURE 3.5: The Cage encasing the equipments

3.4.1 Absorption and Attenuation Measurements

The AC-9 is a spectrophotometer that measures light from a built-in incandescent source transmitted through water inside two 25-cm long flow tubes as shown in Figure 3.6. Water is pumped into these two tubes by a submerged pump. One of the tubes is coated black in the interior wall while the other tube has a highly reflective wall. The non-reflective tube measures the attenuation coefficient while the reflective tube measures the absorption coefficient. A filter wheel splits the light into 9 wavelength bands centered at 412, 440, 488, 510, 532, 555, 650, 676 and 715 nm with a bandwidth of about 10 nm . The AC-9 instrument is powered by a lead-acid battery on-board the ship via a submersible cable which also provides the communication and data transfer link between the instrument and a laptop computer.

The raw data from the attenuation and absorption channels can be viewed real-time on the

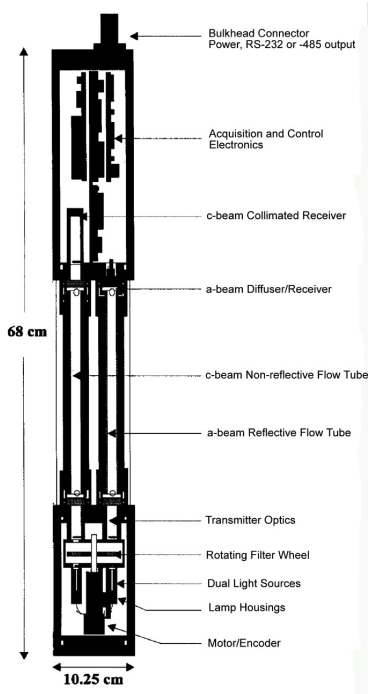

FIGURE 3.6: Schematic diagram of AC-9 from the manual

laptop using a graphical user interface program provided by WETLABS. The absorption and attenuation coefficients measured by the AC-9 have been zeroed by the corresponding coefficients of pure water at 25^0C. Therefore corrections need to be made for salinity and temperature at which the measurements have been made. Absorption of water is affected by salinity (Pegau et al., 1997) and temperature (Pegau & Zaneveld, 1993). They are corrected by using salinity dependence coefficients given by the manufacturer (Zaneveld et al., 1992) and temperature dependence coefficients (Pegau et al., 1997). The raw data is first corrected for temperature and salinity effects. The data from the absorption channel are also corrected for scattering effects (Zaneveld et al., 1992) due to light being scattered by suspended particles out of the path while traveling from the transmitter optics to the detectors, resulting in an over estimation of the absorption. One of the key points to note is that the absorption at 715 nm channel was due to pure water alone and an offset is made such that the absorption coefficient is zero at 715 nm. The details of the data processing and correction procedures are described in Appendix A .

3.4.2 Inherent optical properties of waters at study area

The measured absorption and attenuation coefficients are shown in Figure 3.7 from the six field trips.

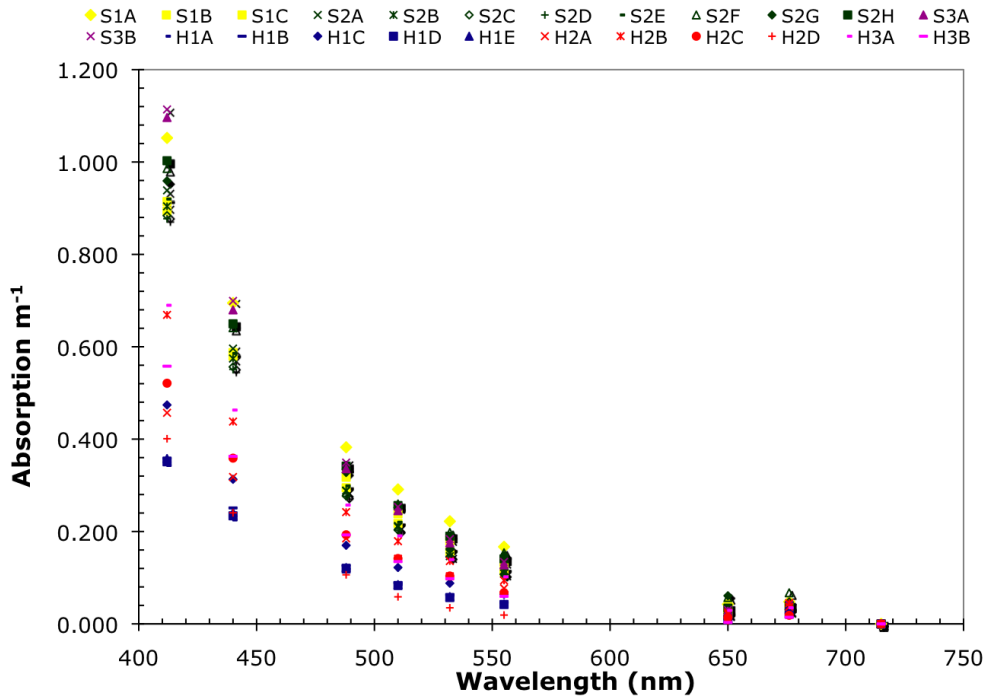

(a) AC-9 measured absorption coefficient

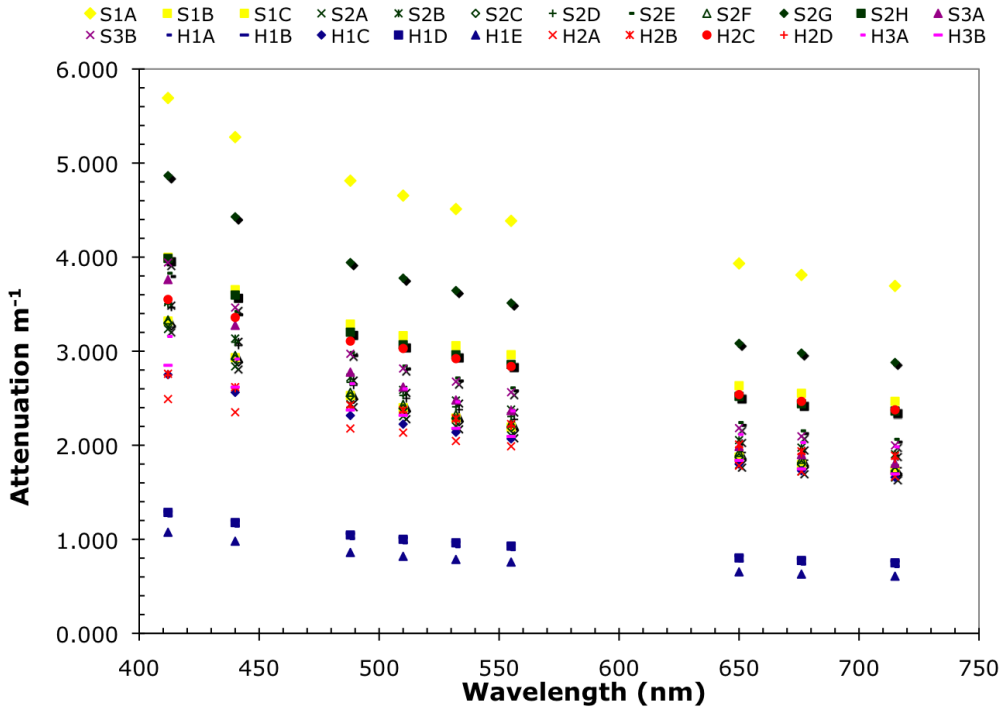

(b) AC-9 measured attenuation coefficient

FIGURE 3.7: Absorption and attenuation Measurements made with AC-9

In Figure 3.7(a), the absorption spectra are seen to cluster into two groups. The group wth higher absorption coeffcients were sampled from P. Semakau and ranged from 0.9 m^{-1} to 1.1 m^{-1} at 412 nm. The other group from P. Hantu ranged from 0.35 m^{-1} to 0.7 m^{-1} at 412 nm. The two bands of absorption indicates that the absorption coefficients at these two locations are different. The low absorption value at the wavelength of 675 nm suggests that the amount of phytoplankton is low. Thus, the absorption coefficients of sea water in these two locations are dominated by CDOM. The water near P. Semakau has higher CDOM content.

The attenuation coefficients do not separate into distinct groups of optical properties sampled. This is due to the fact that the scattering coefficient dominates the attenuation. There were three exceptions seen by the outliers from S1A, H1D and H1E. The majority of the attenuation coefficients fall in the range of 2.4 m^{-1} -4.0 m^{-1} at 412 nm. Thus, the waters are considered turbid with characteristic attenuation length (i.e. inverse of the attenuation coefficient) ranging from 0.25 m to about 0.4 m.

The scattering coefficient is the difference between the attenuation and absorption coefficients. As discussed in the previous chapters, the remote sensing reflectance of water is dependent on the scattering phase function. The Petzold phase function (Petzold, 1972) is widely used as a good estimate of the sea water scatttering phase function in the absence of actual measurements. For the Petzold phase function, the backscattering coefficient is 1.83 $\%$ of the scattering coefficient value. This approximation is used to calculate backscattering coefficient from the measured scatterring coefficient. The total scattering coefficients are shown in Figure 3.8(a) and backscattering coefficients in Figure 3.8(b).

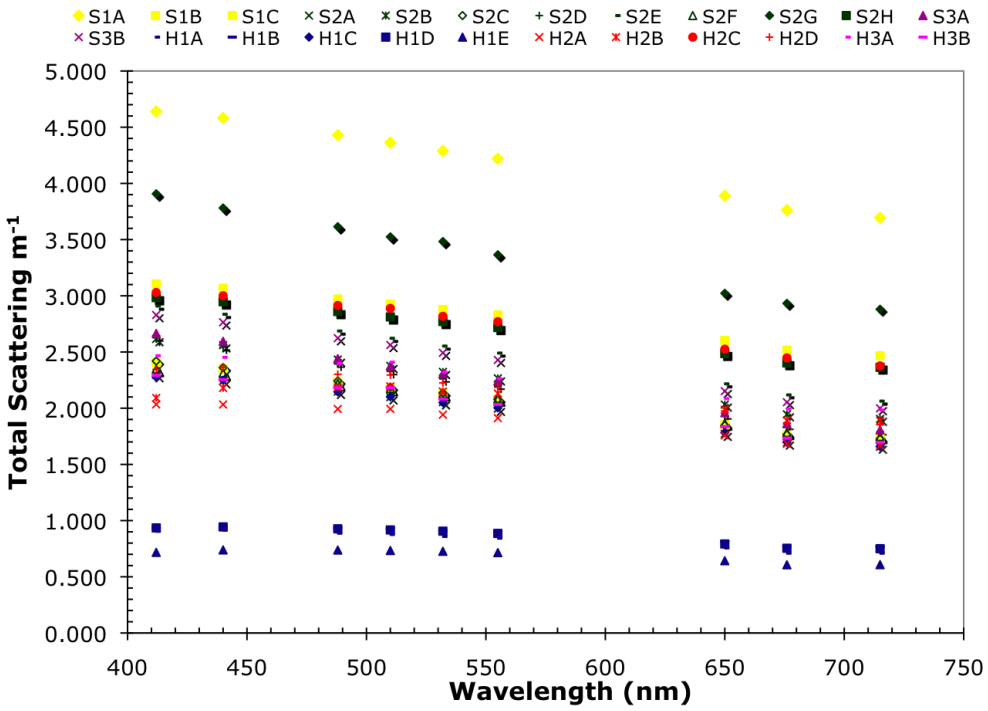

(a) AC-9 measured total scattering coefficients

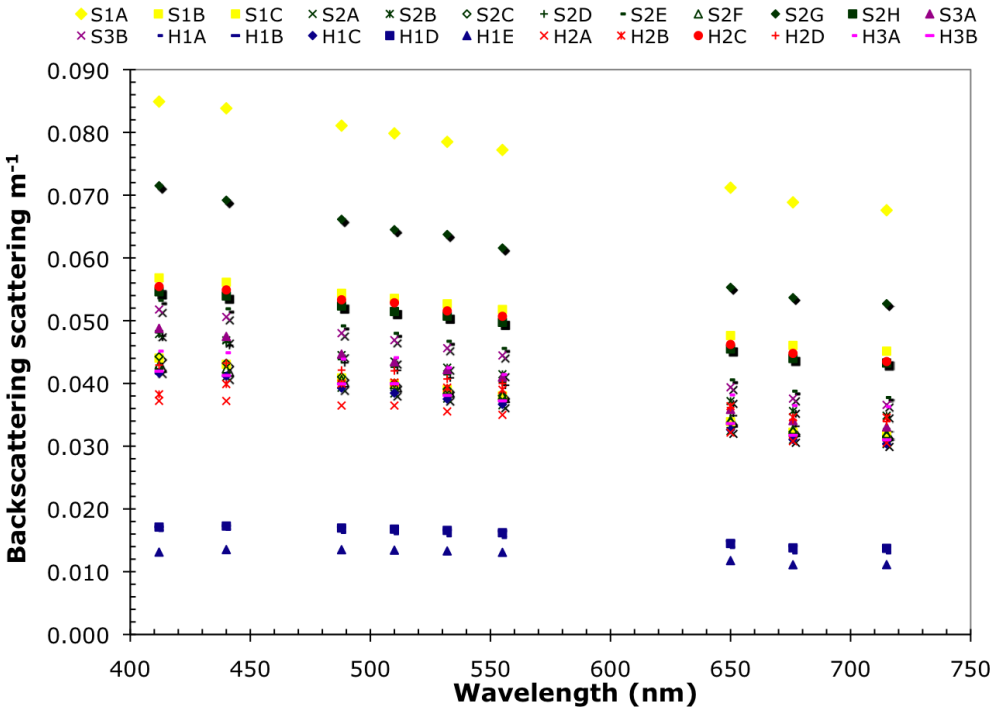

(b) Backscattering coefficients

FIGURE 3.8: Scattering and backscattering(estimated) measurements made with AC-9

The backscattering coefficients show that the water is highly reflective with backscattering coefficients found to be in the range 0.03 m $^{-1}$- 0.06 m $^{-1}$ at 550 nm.

3.4.3 Measured remote sensing reflectance

The remote sensing reflectance spectrums measured at 22 sites are shown in Figure 3.9 .

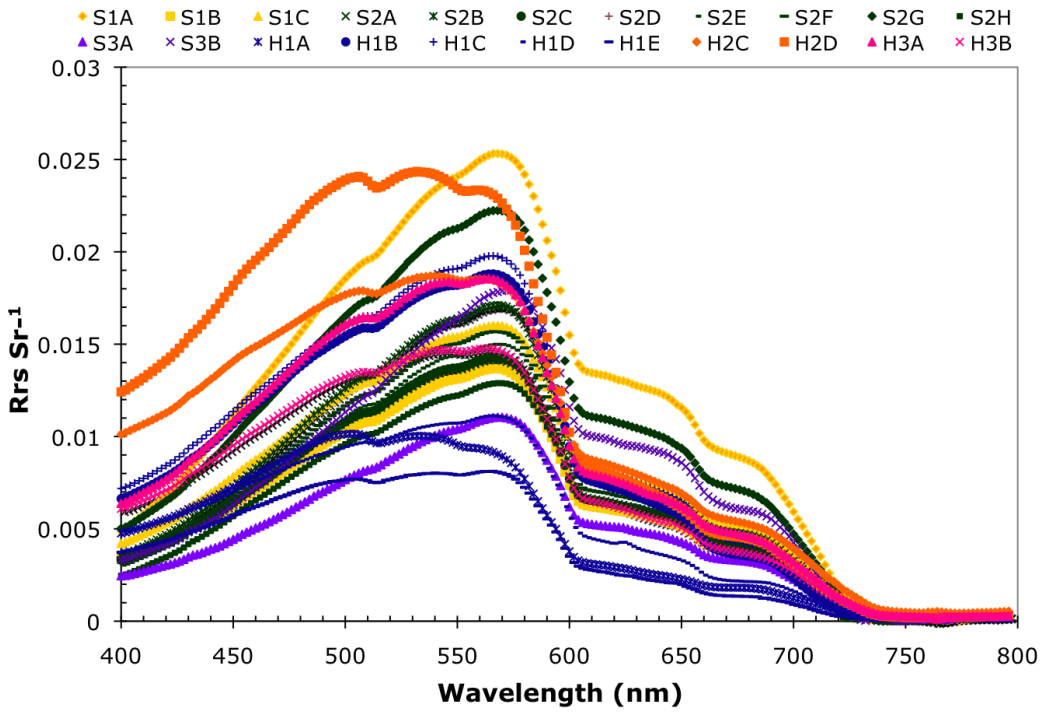

FIGURE 3.9: Field Measurements of $R_{rs}(\lambda)$

As observed from Figure 3.9 many spectra have peaks located around 550 nm. This gives the green colour seen visually. However for the reflectance measured in P. Hantu, especially at sites H2C, H2D, H1A and H1B, the peaks for the reflectance were observed to be slightly shifted to the shorter wavelengths i.e at 520 nm, illstrated in Figure 3.10.

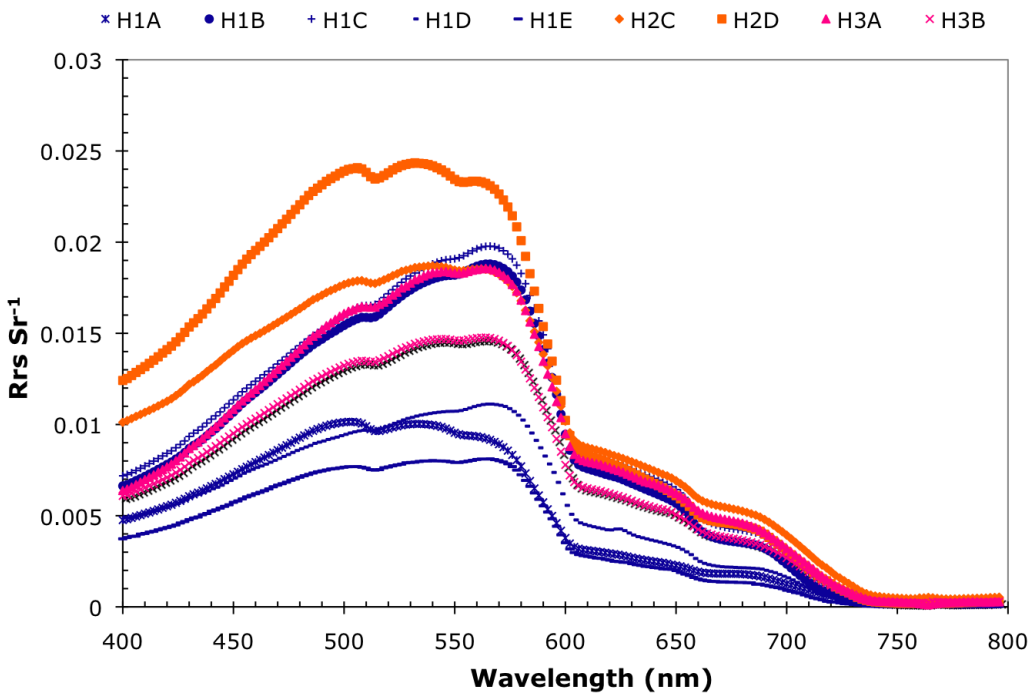

FIGURE 3.10: Field Measurements of $R_{rs}(\lambda)$ at P.Hantu

For H2C and H2D, the absorption coeffcients at 440 nm are 0.350 and 0.240 m^{-1} respectively. These values are lower than those found near P. Semakau and other sites near P. Hantu and could explain the shift of the peak of the reflectance. Sites H1A and H1B have much lower backscattering coefficients at 0.016 m^{-1} and 0.017 m^{-1} which accounts for the much lower reflectance and a flatten peak compared to other reflectance measured near P.Semkau and other site near P.Hantu. So far, the observations could be seen are only qualitative in nature. Neverthelss, an algorithm has been developed to derive the IOPs of the turbid waters from the reflectance measured in a later chapter.

3.5 Optical Properties of constituents

From the absorption coefficients measured, it is possible to decompose it into several components due to different optically active constituents: CDOM, detritus and phytoplankton. CDOM and detritus exhibit similar exponential spectral shape across the wavelength. Thus it is diffcult to resolve the two components. They are usually lumped together as one component. For simplicity of notation, this component will be referred to as the CDOM though it also contains the detritus component.

The measured absorption coefficients were fitted with the absorption models for CDOM (Bricaud et al., 1981) and phytoplankton i.e,

$$a(\lambda) = a_g(\lambda) + a_\phi(\lambda) \tag{3.5}$$

with,

$$a_g(\lambda) = a_g(440)\exp^{s(440-\lambda)} \tag{3.6}$$

and

$$a_\phi(\lambda) = a_\phi(440)a_0(\lambda) + a_\phi(440)\ln(a_\phi(440))a_1(\lambda) \tag{3.7}$$

The fitting parameters are $a_g(\lambda)$, $a_\phi(\lambda)$ and S. These parameters are adjusted until the minimum least square error between the measured and modelled absorption coefficients is obtained. The error function is,

$$\chi = \sum_{i=1}^{8}[a_{model}(\lambda_i) - a_{ac9}(\lambda_i)]^2 \tag{3.8}$$

where a_{model} is the modelled absorption coefficient and a_{ac9} is the absorption coefficient measured by AC-9. The subscript is the wavelength index. Only 8 wavelength channels are used since the nineth channel (715 nm) has been adjusted to zero. An example of the results of decomposition is shown in Figure 3.11.

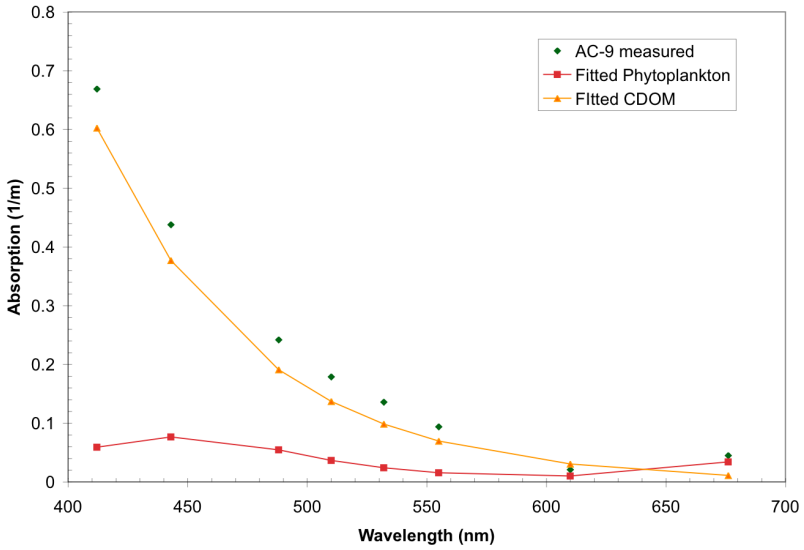

FIGURE 3.11: Example of fitted CDOM and Phytoplankton absorption, site H2D

The derived values of $a_g(440)$, $a_\phi(440)$ and S from P. Hantu and P. Semakau are shown in Table 3.4 and Table 3.5 respectively.

The derived values of $a_g(440)$, $a_\phi(440)$ and S shown in Table 3.4, indicate high amount of CDOM as compared to phytoplankon. For most of the values, the ratio of $a_g(440)$ to $a_\phi(440)$ averages to about 6 times more. However, there are exceptions seen for H1A and H2D where

TABLE 3.4: Derived values of $a_g(440)$, $a_\phi(440)$ and S from P. Hantu sites

S/N	$a_g(440)$ m^{-1}	$a_\phi(440)$ m^{-1}	S nm^{-1}
H1A	0.1848	0.0576	0.0167
H1B	0.2074	0.0492	0.0158
H1C	0.2721	0.0628	0.0157
H1D	0.1976	0.0473	0.0166
H1E	0.1999	0.0513	0.0167
H2A	0.2763	0.0634	0.0135
H2B	0.3947	0.0773	0.0151
H2C	0.3439	0.0226	0.0140
H2D	0.1560	0.0897	0.0272
H3A	0.4375	0.0509	0.0140
H3B	0.3590	0.0177	0.0151

the ratio is less, but $a_g(440)$ is still 3 and 1.5 times more than $a_\phi(440)$. On the whole, CDOM could be seen as the dominating absorption component for sites at P.Hantu.

Table 3.5 shows the derived $a_g(440)$, $a_\phi(440)$ and S values. The values of $a_g(440)$ domainates the absorption coefficient as seen from the table. The ratio of $a_g(440)$ to $a_\phi(440)$ is at least 15 for all the sites.

The spectral slope, S derived for waters near both P.Semkau and P.Hantu is (0.0153 $\pm$ 0.0003) nm^{-1} and (0.0150 $\pm$ 0.0003)nm^{-1}, except for one outlier from P. Hantu. The spread of S is confined to narrow range from 0.014 to 0.017 nm^{-1} as indicated in Figure 3.12 . The similar-

TABLE 3.5: Derived values of $a_g(440)$, $a_\phi(440)$ and S from P. Semakau sites

S/N	$a_g(440)$ m^{-1}	$a_\phi(440)$ m^{-1}	S nm^{-1}
S1A	0.7082	0.0233	0.0134
S1B	0.5748	0.0370	0.0154
S1C	0.5938	0.0230	0.0138
S2A	0.5830	0.0373	0.0160
S2B	0.5742	0.0286	0.0153
S2C	0.5543	0.0317	0.0156
S2D	0.5495	0.0329	0.0155
S2E	0.5848	0.0325	0.0151
S2F	0.6160	0.0703	0.0144
S2G	0.6086	0.0593	0.0145
S2H	0.6555	0.0276	0.0143
S3A	0.6781	0.0418	0.0160
S3B	0.6914	0.0466	0.0158

ity in S indicates that the CDOM probably came from the same source. The values of S for both locations are the same, however one outlier with a value of 0.0245 nm^{-1} from P.Hantu was taken out. The high spectral slope suggests that the CDOM is composed largely of fulvic acid as corresponding to the values reported from field measurements made around the world (Carder et al., 1989).

As seen in Figure 3.13, the absorption coefficient of phytoplankton lies within the range 0.0177

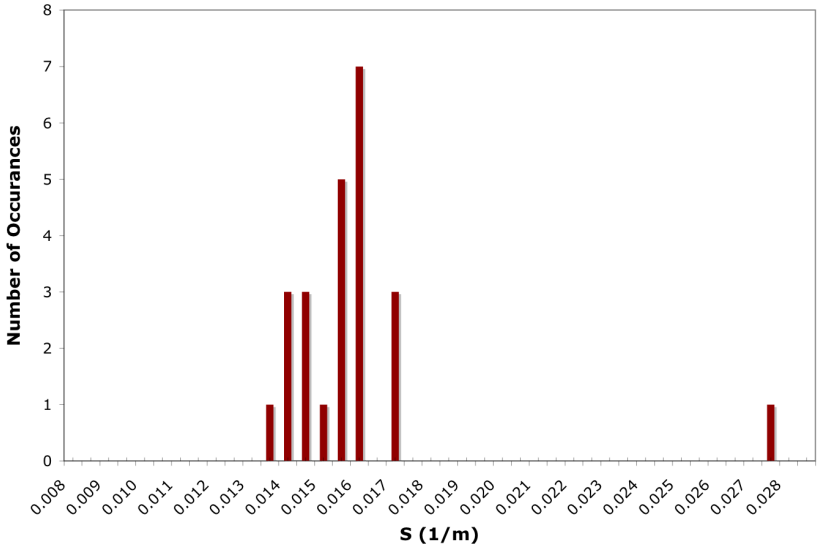

FIGURE 3.12: Histogram of derived S

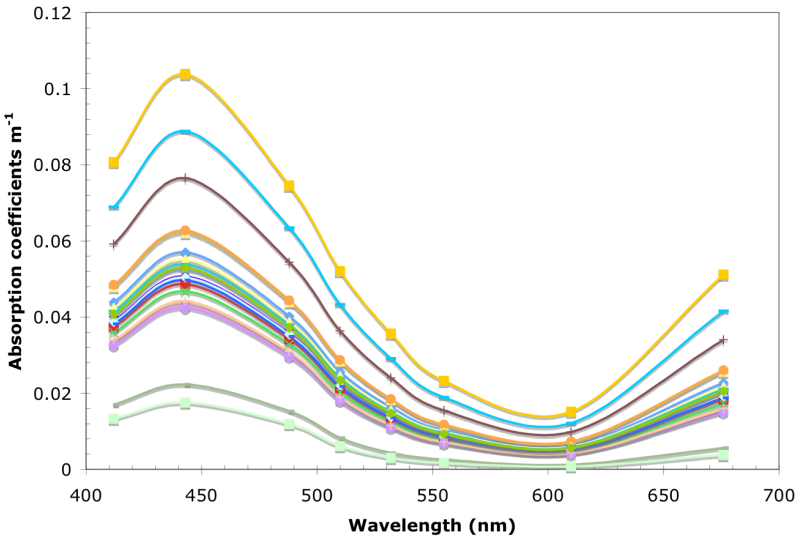

FIGURE 3.13: Exampled of fitted CDOM and Phytoplankton absorption

to 0.0897 m^{-1} at 440 nm. This range is indicative of the small amount of phytoplankon in the sites sampled. The amount of CDOM absorption is many times more than that of phytoplankon as seen from Table 3.4 and Table 3.5.

The backscattering coefficients obtained from the total scattering coefficients were fitted to the backscattering model for particulates, modeled,

$$b_{bp}(\lambda) = b_{bp}(555)(\frac{555}{\lambda})^{Y} \tag{3.9}$$

The parameter Y generally indicates the size of the particles responsible for backscattering. The fitting paramter of Y was adjusted until the error between the modelled and measured is minmized. The error function is shown is defined as,

$$\chi = \sum_{i=i}^{8} [b_{bbp}^{modeled}(\lambda_i) - b_{bbp}^{measured}(\lambda_i)]^2 \tag{3.10}$$

The value for derived Y is calculated to be (0.407 $\pm$ 0.100) and (0.557 $\pm$ 0.09) from the sites at P. Hantu and P. Semakau respectively.

The historgram is shown in Figure 3.14 where the two clusters of derived Y can be seen. Though the values of Y from these two sites are different, the values are still quite close. There is a small overlap of these two clusters of values as seen from the histogram and the deviation of each value. A complete list of derived Y and measured $b_{bp}(550)$ can be seen in Table 3.6 and Table 3.7.

From Table 3.6 and Table 3.7, the waters are highly backscattering with high values of $b_{bp}(555)$ at both sites. Though there are three sites with $b_{bp}(555)$ with values of about 0.016 m^{-1}, the rest

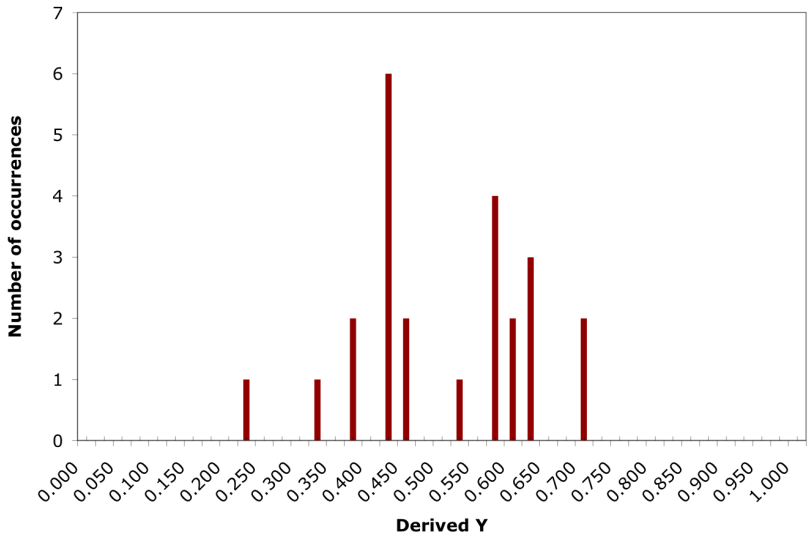

FIGURE 3.14: Histogram of derived Y

of the sites have high values ranging from 0.03 to 0.08 m^{-1}. The values of Y suggests that the particles responsible for the high scattering are slightly different at both locations, but should be quite similar given the closeness and the overlap of the derived Y values.

TABLE 3.6: Values of $b_{bp}(555)$ and Y from P. Hantu sites

S/N	$b_{bp}(555)$ m-1	Y
H1A	0.080	0.408
H1B	0.039	0.589
H1C	0.054	0.409
H1D	0.038	0.580
H1E	0.043	0.570
H2A	0.040	0.603
H2B	0.042	0.682
H2C	0.047	0.609
H2D	0.040	0.523
H3A	0.064	0.555
H3B	0.052	0.418

TABLE 3.7: Values of $b_{bp}(555)$ and Y from P. Semakau sites

S/N	$b_{bp}(555)$ m^{-1}	Y
S1A	0.043	0.685
S1B	0.046	0.614
S1C	0.016	0.444
S2A	0.017	0.357
S2B	0.038	0.560
S2C	0.017	0.401
S2D	0.014	0.311
S2E	0.034	0.362
S2F	0.038	0.215
S2G	0.053	0.424
S2H	0.042	0.430
S3A	0.043	0.415
S3B	0.039	0.563

3.6 Case-1 or Case 2 Waters?

Case-1 waters have inherent optical properties determined by only one parameter, i.e. the phytoplankon concentration (Preisendorfer, 1976). As descrbed in chapter 2, this means that the absorption coefficients of CDOM and phytoplankon as well as the backscattering coefficients of suspended particles are parameterized by the concentration of phytoplankon. In a recent paper, Lee & Hu (2006) examined how Case-1 waters is distributed in the world by two criterion. These two criteria were obtained by calculating values of $R_{rs}(\lambda)$ using values of C (Lee & Hu, 2006) and obtaining them with band ratios of $R_{rs}(\lambda)$. The relationship between $R_{rs}(\lambda)$ and C were obtained by using an iterative process where the corresponding values of $R_{rs}(\lambda)$ and $a_{tot}(\lambda)$ were derived based on measurements of diffuse attenuation (Morel & Maritorena, 2001). The main aim of the iterative process was to use the measured C and corresponding diffuse attenuation values to build a relationship to calculate $R_{rs}(\lambda)$ from C (Morel & Maritorena, 2001).

The two criteria are ,

$$RR_{12}^{CS1} = 0.9351 + \frac{0.113}{RR_{53}} - \frac{0.0217}{RR_{53}^2} + \frac{0.003}{RR_{53}^3} \tag{3.11}$$

and

$$R_{rs}(555)^{CS1} = 0.0006 + 0.0027RR_{53} - 0.0004RR_{53}^2 - 0.0002RR_{53}^3 \tag{3.12}$$

where,

$$RR_{12} = \frac{R_{rs}(412)}{R_{rs}(443)} \tag{3.13}$$

and

$$RR_{53} = \frac{R_{rs}(555)}{R_{rs}(490)} \tag{3.14}$$

These equations were fitted empirically using the generated values of $R_{rs}(\lambda)$ for Case-1 waters. $R_{rs}(555)^{CS1}$ and RR_{12}^{CS1} are the values for exact Case-1 type water that will be predicted by Eq.(3.11) and Eq.(3.12). These two criterion are functions of the band ratios of the reflectance of Case-1 waters at different wavelengths. The first criterion states that for Case-1 water, the band ratio for reflectance at 412 over 443 nm can be predicted by its band ratio RR_{53}. The second states that the reflectance at 553 nm can be predicted by the band ratio for certain reflectance wavelengths.

In order to locate Case-1 waters with the criterion, the variation of RR_{12} predicted by Eq.(3.11) was allowed up to 10 $\%$ and $R_{rs}(555)$ in Eq.(3.12) up to 50 $\%$ as recommended (Lee & Hu, 2006).

These criteria are shown by the shaded area in Figure 3.15(a) and Figure 3.15(b). The test was also repeated on SEABASS data which is a repositry of in situ optical and radiomteric measurements around the world. This essentially means that for Case-1 waters, they must fall within the shadow area as shown in Figure 3.15(a) and Figure 3.15(b).

As seen from the two figures, the points in triangle which denote the measurements made in our field expeditions lie outside the stipulated range of Case-1 waters. The small amount of phytoplankon in the previous section also suggests that the waters sampled are not Case-1, since it cannot be used as a parameter to compute the optical properties of other components. For the SEABASS data (Werdell & Bailey, 2005), half of the points lie in the region of the

shaded area which indicates that they belong to Case-1 waters.

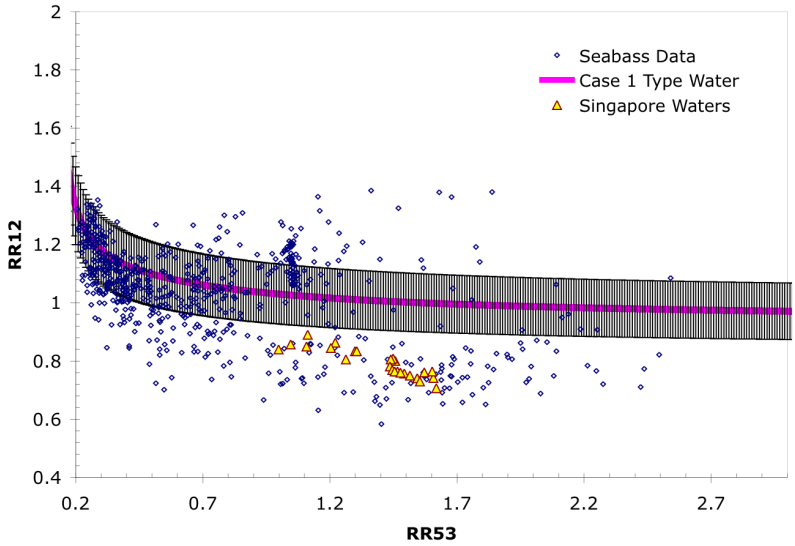

(a) Critera one for Case-1 Waters

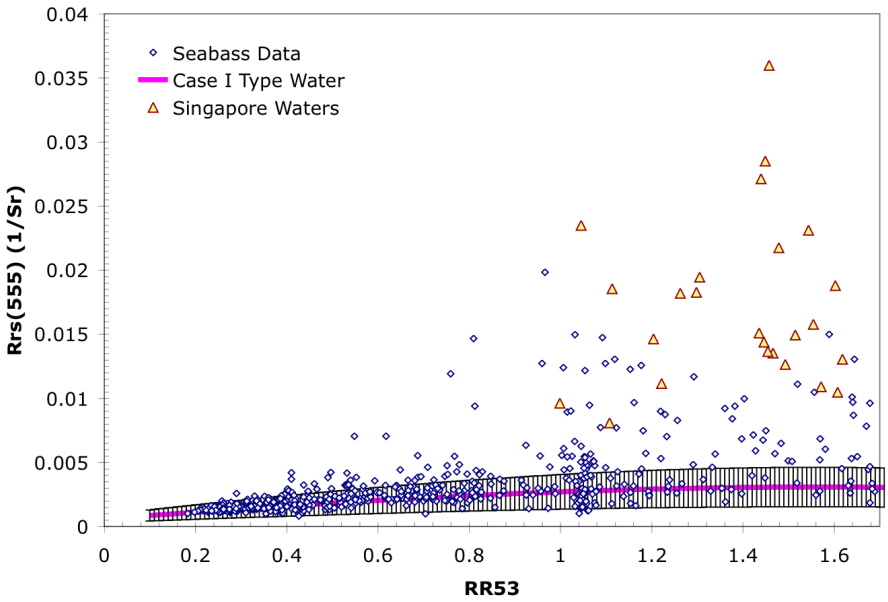

(b) Critera two for Case-1 Waters

FIGURE 3.15: Criterions for Case-1 Waters

3.7 Conclusions

The process of carrying out field measurements on small research vessels involves significant manpower and coordination effort. Moreover environmental conditions such as rapidly changing cloud cover, sudden thunderstorms, passing marine vehicle made the radiometric measurements unusable at times. The in situ measurements were affected by passing marine vessels and strong underwater currents. Despite these setbacks, a good number of measurements were still obtained. Discussion on the faced will be described in Appendix B.

The waters surveyed were high in CDOM absorption and particulate backscattering, this was seen in the section where the measured coefficients were decomposed into various components. The low absorption peak at 675 nm suggests that phytoplankton was not found in great abundance in our waters. The small amount of $a_\phi(\lambda)$ compared to $a_g(\lambda)$ further showed the dominance of CDOM in the waters surevyed. The similar values of S derived show that the CDOM is of a similar origin. The two groups Y values suggest that the particulates at the two locations are slightly different as there is an overlap of the values derived from the historgram in Figure 3.14. As expected, the waters in Singapore is not Case-1 where concentration of phytoplankton covaries with the other optically constituents of water. In Section 3.6 the reflectances were evaluated with the two criteria proposed by (Lee & Hu, 2006) to determine whether the waters tested are Case-1 waters.

This would mean that the absorption and backscattering coefficients cannot be paramterized by C. This makes the retrieval of IOPs from the waters more complex, as both absorption and

backscattering coefficients are not expressed by empirical relations with C as the key parameter.

The radiometric measurements of reflectance provided field measured spectra to develop algorithms to retrieve the IOPs. Even though there are many algorithms that has been published to retrieve IOPs from non Case-1 waters, an in-house algorithm was developed to retrieve the IOPs from reflectance measurements around the coastal waters of Singapore especially over shallow waters. The measured IOPs would be useful as valiation for algorithms developed for retrieval and the algorithm to be discussed in later chapters.

Chapter 4

Cloud and Shadow Method To Retrieve Atmospheric Properties

This chapter describes the development and implementation of an atmospheric correction scheme for satellite imagery acquired by a high spatial resolution multispectral sensor (Ikonos) and a hyperspectral imaging sensor (Hyperion). The scheme makes use of the radiance detected over cloud, shadow and water features in the image. Similar methods that use such features have been implemented on AVIRIS which is an airborne hyperspectral sensor (Mustard et al., 2001). Another method uses cloud and shadow image features to calibrate the AVIRIS sensor (Reinersman et al., 1998). However assumptions for atmospheric conditions such as the ratio of direct solar irradiance to the diffuse skylight irradiance have to be assumed. This assumption is needed to derive the path radiance which is the main component of the total signal detected. In the scheme reported here for Ikonos and Hyperion, this assumption is overcome by deriving the path radiance from the radiance over the features. This method also attempts to retrieve the water leaving reflectance by using less stringent assumptions at the near infrared band (NIR)

to derive the cloud reflectance which is used to scale the water leaving reflectance. A previous method (Mustard et al., 2001) also used cloud and shadow features to derive the water reflectance spectral shape only.

Another advantage of this method is that it does not require the calibration constants for the conversion of raw digital counts to radiance in the whole visible spectrum. Only the calibration constant at one NIR band is needed. The stability of sensor calibration conversion is very important for remote sensing of ocean where the signal constitutes at most 10 $\%$ of the total signal (Gordon & Clark, 1981; Gordon, 1987). For sensors that is calibrated with a 5 $\%$ uncertainty for radiance would result in about 50 $\%$ error in the retrieved water leaving reflectance (Reinersman et al., 1998). Thus stringent requirements on the sensor radiometric calibration accuracy are necessary. In this study, the information needed to perform atmospheric correction comes mainly from the imagery with minimal inputs from ancillary sources such as solar irradiance, water vapour content, aerosol model, optical thickness and calibration constants for conversion of raw counts into radiance. The only ancillary data needed are the calibration constants, and extraterrestrial solar irradiance at one NIR band.

For the validation of the atmospheric scheme implemented on Ikonos imagery, concurrent field measurements for the water leaving reflectance were compared to the reflectance spectra from the Ikonos imagery after atmospheric correction. For the Hyperion images captured a few years back no field measurements are available for validation. The results from the cloud and shadow atmospheric correction scheme are compared with those obtained from more established ones such as TAFKAA.

The cloud and shadow method implemented also allows atmospheric properties such as aerosol model, optical thickness and scattering transmittance to be derived from the path radiance obtained. The aerosol model and optical thickness were obtained by fitting the derived path radiance from the scheme to pre-computed parameters. The total atmospheric transmittance was derived from the corrected cloud radiance.

4.1 Algorithm Formulation

Figure 4.1 is a schematic diagram that illustrates the cloud, shadow and water features used in this atmospheric correction scheme. In the diagram a cloud casts a shadow on the water surface. The term $L_c(\lambda)$ denotes the radiance reflected from the cloud and detected by the sensor. $L_t(\lambda)$ and $L_s(\lambda)$ denote the radiance from the water and shadow area respectively. For the water surface outside the shadow, the downwelling irradiance has two components: the direct solar component $E_{dir}(\lambda)$ and the diffuse skylight $E_{sky}(\lambda)$. The shadowed area only has the diffuse downwelling irradiance, $E_{sky}(\lambda)$.

The top-of-atmosphere radiance detected over a water pixel outside the shadow can be written as,

$$L_t(\lambda) = \frac{T^{\uparrow}(\lambda)E_{dir}(\lambda)\rho_w(\lambda)}{\pi} + \frac{T^{\uparrow}(\lambda)E_{sky}(\lambda)\rho_w(\lambda)}{\pi} + T_g^{\uparrow\downarrow}(\lambda)L_{path}(\lambda) \tag{4.1}$$

where $T^{\uparrow}$ is the total upward transmittance and $T_g^{\uparrow\downarrow}(\lambda)$ denotes the two way gaseous transmittance. The water reflectance is denoted by ρ_w and $L_{path}(\lambda)$ is the path radiance.

For a water surface under cloud shadow, the radiance measured is,

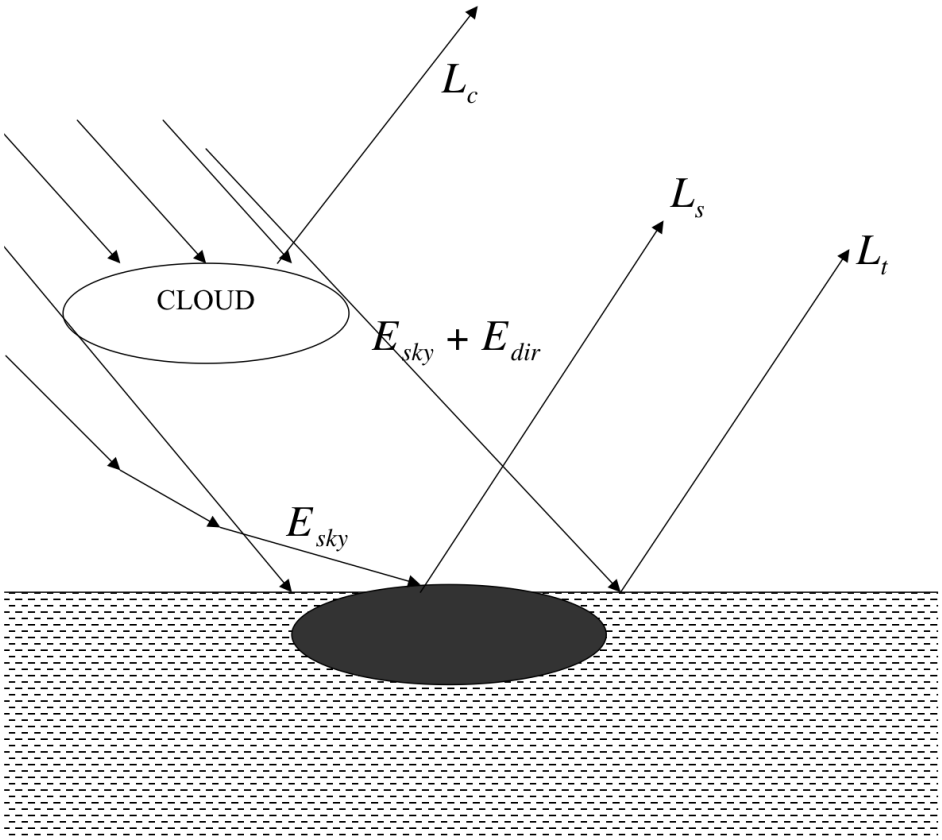

FIGURE 4.1: Figure depicting the scenario with cloud and shadow features

$$L_s(\lambda) = \frac{T^{\uparrow}(\lambda)E_{sky}(\lambda)\rho_w(\lambda)}{\pi} + T_g^{\uparrow\downarrow}(\lambda)L_{path}(\lambda) \tag{4.2}$$

The radiance reflected off the cloud top and detected by the satellite sensor is,

$$L_c(\lambda) = \frac{T^{\uparrow}(\lambda)E_{dir}(\lambda)\rho_c(\lambda)}{\pi} + \frac{T^{\uparrow}(\lambda)E_{sky}(\lambda)\rho_c(\lambda)}{\pi} + T_g^{\uparrow\downarrow}(\lambda)L_{path}(\lambda) \tag{4.3}$$

where $\rho_c(\lambda)$ is the cloud reflectance.

The main problem in deriving the water reflectance is to find $T_g^{\uparrow\downarrow}(\lambda)L_{path}(\lambda)$ which is the path radiance term.

Subtracting Eq.(4.1) from Eq.(4.2), we get

$$L_t(\lambda) - L_s(\lambda) = \frac{T^{\uparrow}(\lambda)E_{dir}(\lambda)\rho_w(\lambda)}{\pi} \tag{4.4}$$

and Eq.(4.1) is rewritten as,

$$L_t(\lambda) - L_p^{'}(\lambda) = \frac{T^{\uparrow}(\lambda)(E_{dir}(\lambda) + E_{sky}(\lambda))\rho_w(\lambda)}{\pi} \tag{4.5}$$

with,

$$L_p^{'}(\lambda) = T_g^{\uparrow\downarrow}(\lambda)L_{path}(\lambda) \tag{4.6}$$

The next step is to define a parameter, α,

$$\alpha = 1 + \frac{E_{sky}(\lambda)}{E_{dir}(\lambda)} \tag{4.7}$$

This parameter is the ratio of the total downward irradiance at the surface to the direct irradiance. It is an indicator of the amount of sky light that is generated by scattering in the atmosphere due to molecular or particulate scattering. Eq.(4.4) and Eq.(4.5) can be combined to give,

$$L_t(\lambda) - L_p^{'}(\lambda) = \alpha(L_t(\lambda) - L_s(\lambda)) \tag{4.8}$$

hence $L_p'(\lambda)$ is given by,

$$L_p'(\lambda) = L_t(\lambda) - \alpha(\lambda)(L_t(\lambda) - Ls(\lambda)) \tag{4.9}$$

Note that on the right-hand side of Eq.(4.9), both $L_t(\lambda)$ and $Ls(\lambda)$ are measured quantities. If derived value of $\alpha(\lambda)$ is known, $L_p'(\lambda)$ can be computed. This value can be obtained by assuming atmospheric conditions such as the aerosol type and optical thickness for radiative transfer codes to compute the ratio of sky light to direct sun solar beam (Mustard et al., 2001). In one

method the value of $E_{sky}(\lambda)/E_{dir}(\lambda)$ is given to be 0.707 by assuming a Lambertian sky (Reinersman et al., 1998).

In our approach, the value of $L'_p(\lambda)$ would be derived by assuming a value of $\alpha(\lambda)$ at the NIR, since the difference of $L_t(\lambda)$ and $L_s(\lambda)$ is small at the NIR. After which making use of a series of equations that relate the cloud reflectance to the difference of two different cloud patches, $L'_p(\lambda)$ is derived. This value was selected based on computed $\alpha(\lambda)$ values for different aerosol model and optical thickness and the range of $\alpha(\lambda)$ likely to be found at NIR. However in later sections, it would be shown that the choice of $\alpha(\lambda)$ does not have much influence on the $L'_p(\lambda)$ derived.

If $\rho_c(\lambda)$ is spectrally flat, then it is possible to obtain the absolute value of $\rho_w(\lambda)$ from Eq.(4.10) if value of $\rho_c(\lambda)$ is known.

$$\frac{\rho_w(\lambda)}{\rho_c(\lambda)} = \frac{L_t(\lambda) - L'_p(\lambda)}{L_t(\lambda) - L'_p(\lambda)} \tag{4.10}$$

4.1.1 Values of alpha

In this section, the values of $\alpha(\lambda)$ is examined using the COART(Coupled Ocean Atmosphere Radiative Transfer) code (Jin et al., 2006) which computes the amount of diffuse sky light and direct sun light arriving at the surface of water. Two aerosol types were used to generate values for α. These two types are MODTRAN maritime and MODTRAN urban which probably fit the profile in Singapore, which is highly urbanized and the images are over the ocean. The optical thickness at 550 nm was varied from 0.1 to 0.3 for the different aerosol models. The values of

α computed are shown in Figure 4.2

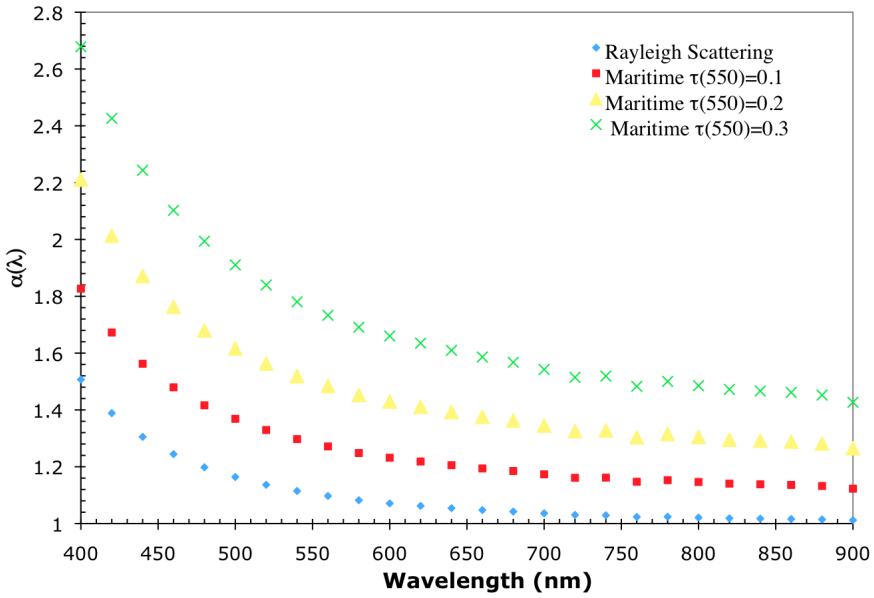

(a) Value of $\alpha(\lambda)$ computed with Maritime aerosols

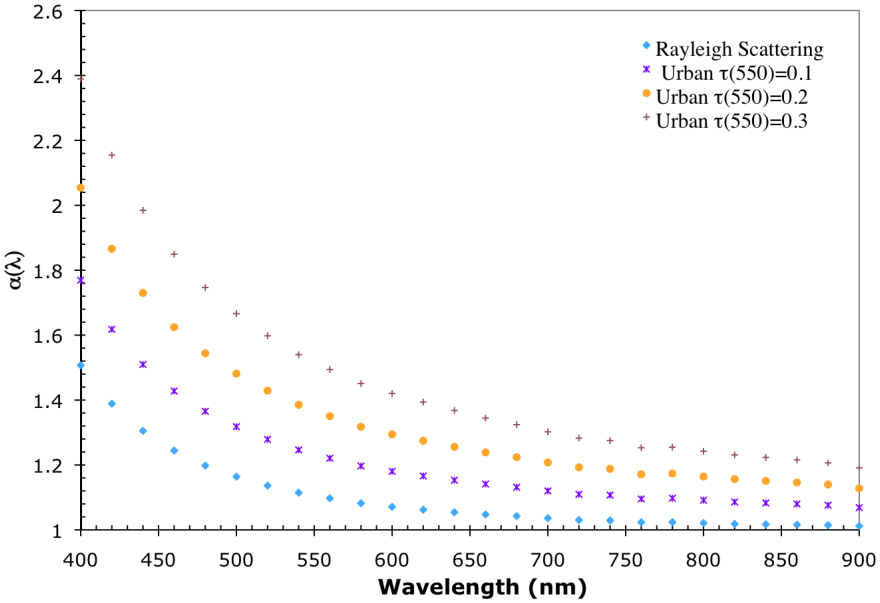

(b) Value of $\alpha(\lambda)$ computed with Urban aerosols

FIGURE 4.2: Computed $\alpha(\lambda)$ for Maritime and Urban aerosol types and optical thickness, $\tau(550)$

As the optical thickness increases, the value of $\alpha(\lambda)$ increases. This is due to increasing amount of diffuse skylight resulting from more scattering of light with aerosol. Under very low aerosol loading, the values of $\alpha(\lambda)$ in the NIR approaches one. Even for higher aerosol loading, it was found to be less than 1.4 at wavelength longer than 700 nm.

4.1.2 Deriving L'_p

In this section, a new method is introduced to derive $L'_p(\lambda)$ using radiance detected over two cloud patches. Suppose that $L_{c1}(\lambda)$ is the radiance measured over a patch of cloud with reflectance $\rho_{c1}(\lambda)$ and $L_{c2}(\lambda)$ is the radiance over a second cloud patch, then it can be shown from Eq.(4.3),

$$\frac{L_{c_1}(\lambda)}{L_{c_1}(\lambda) - L_{c_2}(\lambda)} = \frac{\rho_{c_1}(\lambda)}{\rho_{c_{12}}(\lambda)} + \frac{L'_p(\lambda)}{L_{c_1}(\lambda) - L_{c_2}(\lambda)} \tag{4.11}$$

where,

$$\rho_{c_{12}}(\lambda) = \rho_{c1}(\lambda) - \rho_{c2}(\lambda) \tag{4.12}$$

Hence $L'_p(\lambda)$ cane be expressed as,

$$L'_p(\lambda) = L_{c1}(\lambda) - (L_{c_1}(\lambda) - L_{c_2}(\lambda)) \left[\frac{\rho_{c_1}(\lambda)}{\rho_{c_{12}}(\lambda)}\right] \tag{4.13}$$

Thus $L'_p(\lambda)$ can be computed if the ratio $\rho_{c_1}(\lambda)/\rho_{c_{12}}(\lambda)$ is known. A potential problem with this formulation is that if the values of $L_{c1}(\lambda)$ and $L_{c2}(\lambda)$ are comparable in value, the difference in the radiance will be equivalent to the noise of the sensor. To avoid this problem, the two cloud patches selected must be such that the difference in the cloud radiance is greated than the value of $L_s(\lambda)$, the radiance of the shadow pixels.

4.1.3 Estimating $\rho_{c_1}(\lambda)/\rho_{c_{12}}(\lambda)$

The value $\rho_{c_1}(\lambda)/\rho_{c_{12}}(\lambda)$ needs to be known before Eq.(4.13) can be used to calculate the value for $L'_p(\lambda)$. It has been shown in Figure 4.2, the values of $\alpha(\lambda)$ at NIR fall within the range of 1 to 1.4 for aerosol optical thickness at 550 nm varied from 0 to 0.3, except for the case of maritime aerosols with optical thickness of 0.3. To estimate $\rho_{c_1}(\lambda)/\rho_{c_{12}}(\lambda)$, we start with,

$$L'_p(\lambda) = L_t(\lambda) - \alpha(\lambda)\left[L_t(\lambda) - L_s(\lambda)\right] \tag{4.14}$$

A suitable wavelength λ_0 in the NIR region is chosen and assuming that

$$\alpha(\lambda_0) = 1.2 \tag{4.15}$$

Then, $L'_p(\lambda_0)$ can be calculated,

$$L'_p(\lambda_0) = L_w(\lambda_0) - \alpha(\lambda_0)\left[L_w(\lambda_0) - L_s(\lambda_0)\right] \tag{4.16}$$

and the ratio $\rho_{c_1}(\lambda_0)/\rho_{c_{12}}(\lambda_0)$ can be calculated at λ_0,i.e.

$$\frac{\rho_{c_1}(\lambda)}{\rho_{c_{12}}(\lambda)} = \frac{L_{c1}(\lambda_0) - L'_P(\lambda_0)}{L_{c1}(\lambda_0) - L_{c1}(\lambda 0)} \tag{4.17}$$

If the ratio $\rho_{c_1}(\lambda)/\rho_{c_{12}}(\lambda)$ is spectrally flat, i.e its value is relatively constant over the visible and NIR regions, the value estimated at λ_0 can be extrapolated to all wavelengths in the visible region,i.e

$$\frac{\rho_{c_1}(\lambda)}{\rho_{c_{12}}(\lambda)} \simeq \frac{\rho_{c_1}(\lambda_0)}{\rho_{c_{12}}(\lambda_0)} \tag{4.18}$$

$L'_p(\lambda)$ at all wavelengths in the visible and NIR regions can then be calculated as,

$$L'_p(\lambda) = L_{c1}(\lambda) - \left(L_{c_1}(\lambda) - L_{c_2}(\lambda)\right)\left[\frac{\rho_{c_1}(\lambda_0)}{\rho_{c_{12}}(\lambda_0)}\right] \tag{4.19}$$

It will be shown that the value of $L'_p(\lambda)$ obtained using this method is relatively insensitive to the value of $\alpha(\lambda_0)$ chosen, so long as $\alpha(\lambda_0)$ fall within the range of 1 to 1.4. Suppose that the uncertainty in $\alpha(\lambda_0)$ is $\Delta\alpha_0$, then the uncertainty in $L'_p(\lambda_0)$ is

$$\Delta L'_p(\lambda_0) = \Delta\alpha_0[L_t(\lambda_0) - L_s(\lambda_0)] \tag{4.20}$$

Uncertainty in $\rho_{c_1}(\lambda_0)/\rho_{c_{12}}(\lambda_0)$ is

$$\Delta\frac{\rho_{c_1}(\lambda_0)}{\rho_{c_{12}}(\lambda_0)} = \frac{-\Delta L'_p(\lambda_0)}{L_{c1}(\lambda_0) - L_{c2}(\lambda_0)} \tag{4.21}$$

and the uncertainty in the estimated $L'_p(\lambda)$ is

$$\Delta L'_p(\lambda) = -\Delta\frac{\rho_{c_1}(\lambda_0)}{\rho_{c_{12}}(\lambda_0)}\left(L_{c1}(\lambda) - L_{c2}(\lambda)\right) \tag{4.22}$$

$$\Delta L'_p(\lambda) = -\Delta\frac{\rho_{c_1}(\lambda_0)}{\rho_{c_{12}}(\lambda_0)}\left(\frac{L_{c1}(\lambda) - L_{c2}(\lambda)}{L_{c1}(\lambda_0) - L_{c2}(\lambda_0)}\right) \tag{4.23}$$

with substitution from Eq.(4.20),

$$\Delta L'_p(\lambda) = \Delta L'_p(\lambda_0)[L_w(\lambda_0) - L_s(\lambda_0)]\left(\frac{L_{c1}(\lambda) - L_{c2}(\lambda)}{L_{c1}(\lambda_0) - L_{c2}(\lambda_0)}\right) \tag{4.24}$$

It is to note that

$$L_t(\lambda_0) - L_s(\lambda_0) = \frac{L_t(\lambda_0) - L'_p(\lambda_0)}{\alpha(\lambda_0)} \tag{4.25}$$

so,

$$\frac{\Delta L'_p(\lambda)}{L'_p(\lambda)} = \left(\frac{\Delta\alpha_0}{\alpha(\lambda)}\right)\left(\frac{L_t(\lambda) - L'_p(\lambda_0)}{L'_p(\lambda)}\right)\left(\frac{L_{c1}(\lambda) - L_{c2}(\lambda)}{L_{c1}(\lambda_0) - L_{c2}(\lambda_0)}\right) \tag{4.26}$$

At NIR, water reflectance is small, so $L_t(\lambda_0)$ is practically equal to $L'_p(\lambda 0)$. Hence,

$$\frac{L_w(\lambda_0) - L'_p(\lambda_0)}{L'_p(\lambda)} \lll 1 \tag{4.27}$$

Furthermore, the cloud radiance is more or less spectrally flat, hence,

$$\frac{L_{c1}(\lambda) - L_{c2}(\lambda)}{L_{c1}(\lambda_0) - L_{c2}(\lambda_0)} \approx 1 \tag{4.28}$$

At most, $\Delta\alpha_0$ is $\pm$ 0.2 and $\alpha(\lambda_0) \approx 1.2$ so,

$$\left|\frac{\Delta\alpha_0}{\alpha(\lambda_0)}\right| \leqslant 0.2 \tag{4.29}$$

Suppose that ,

$$\frac{L_w(\lambda_0) - L'_p(\lambda_0)}{L'_p(\lambda)} \simeq 0.25 \tag{4.30}$$

which is an estimation based on remote sensing data for the Ikonos data. The uncertainty of $L'_p(\lambda)$ would be

$$\left|\frac{\Delta L'_p(\lambda)}{L'_p(\lambda)}\right| \approx 0.05 \tag{4.31}$$

4.1.4 Deriving water reflectance

Once $L'_p(\lambda)$ is known, the water radiance normalized by the cloud radiance derived from Eq.(4.3) and Eq.(4.1) can be expressed as,

$$\frac{\rho_w(\lambda)}{\rho_c(\lambda)} = \frac{L_t(\lambda) - L'_p(\lambda)}{L_c(\lambda) - L'_p(\lambda)} \tag{4.32}$$

and reflectance of water is,

$$\rho_w(\lambda) = \rho_c(\lambda)\frac{L_t(\lambda) - L'_p(\lambda)}{L_c(\lambda) - L'_p(\lambda)} \tag{4.33}$$

Note that up to this stage, all the calculations involving radiance can be done with the raw digital counts, without the need to convert to absolute radiance units. Since all the equations involve ratio of radiance values of each wavelength channel. Even if the digital counts have been converted to radiance, the results obtained would not be affected by accuracy of the calibration constants. The cloud reflectance can be calculated by

$$\rho_c(\lambda) = \frac{\pi(L_c(\lambda) - L'_p(\lambda))}{T_g^{\uparrow\downarrow}(\lambda)T_s^{\uparrow\downarrow}(\lambda)F_d(\lambda)\cos_{\theta_s}} \tag{4.34}$$

Now calibration constants are required to convert the digital counts to radiance for $L_c(\lambda)$ and $L'_p(\lambda)$. Any calibration errors would be propagated to $\rho_c(\lambda)$. Assuming that the cloud reflectance is spectrally flat, then only the calibration constant at one NIR band is needed and the calculated $\rho_c(\lambda)$ would be extrapolated to the visible band.

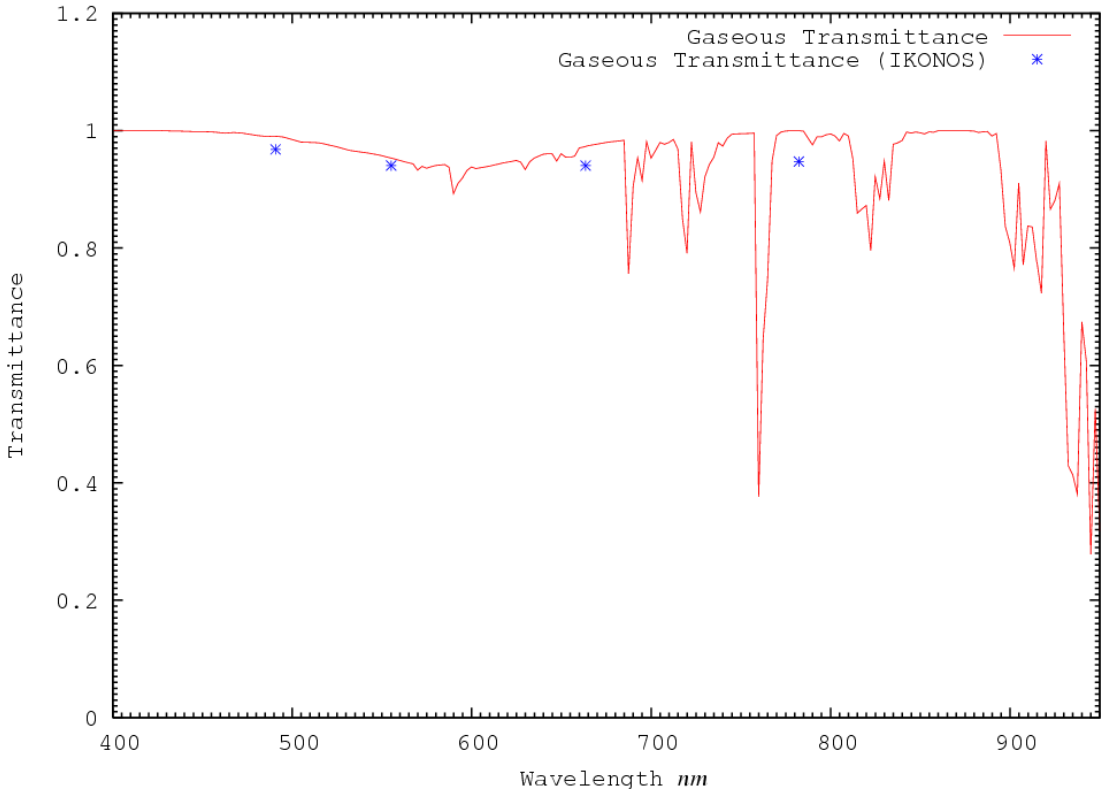

FIGURE 4.3: Atmospheric Transmittance

In order to obtain cloud reflectance, the values of $T_g^{\uparrow\downarrow}(\lambda)$ and $T_s^{\uparrow\downarrow}(\lambda)$ are needed. For Ikonos imagery, these values were computed using the 6S radiative transfer code (Vermote et al., 1997), by assuming a standard tropical atmospheric profile. The main concern would be the presence of absorption bands of water vapour and oxygen at the NIR bands. However, since the Ikonos has broad spectral bandwidths, the absorption features at NIR would be averaged out after convoluting with the band response function of Ikonos. Figure 4.3 shows the computed gaseous

transmittance spectrum and the transmittance of the Ikonos spectral bands. It is seen that the absorption features are indeed averaged out in the NIR band of Ikonos. For the Hyperion data, the transmittance at wavelengths near 850 nm is almost one, hence, this wavelength is used to calculate $\rho_c(\lambda)$.

For the Hyperion data, there is no need to estimate the absorption at the longer wavelength as it is known to be almost 1, hence reducing the possible errors that might arise from such an estimation.

4.1.5 Deriving aerosol type and optical thickness

In this section, parameters such as aerosol type and optical thickness will be shown to be retrieved from this atmospheric correction scheme. Starting from the cloud radiance in Eq.(4.3), we have

$$L_c(\lambda) - L_p^{'}(\lambda) = \frac{T_g^{\uparrow\downarrow}(\lambda) T_s^{\uparrow\downarrow}(\lambda) F_d(\lambda) \rho_c(\lambda)}{\pi} \tag{4.35}$$

and

$$L_p^{'}(\lambda) = \frac{T_g^{\uparrow\downarrow}(\lambda) F_d(\lambda) \rho_{path}(\lambda)}{\pi} \tag{4.36}$$

where $\rho_{path}(\lambda)$ is the path reflectance. Dividing the above two equations, the follwing is obtained,

$$\rho_c(\lambda) \frac{L_p^{'}(\lambda)}{L_c(\lambda) - L_p^{'}(\lambda)} = \frac{\rho_{path}(\lambda)}{T_s^{\uparrow\downarrow}(\lambda)} \tag{4.37}$$

The term $\rho_{path}(\lambda)/T_s^{\uparrow\downarrow}(\lambda)$ is the path reflectance divided by the scattering transmittance. It is possible to retrieve aerosol type and optical thickness from this term by matching with quantities computed using a radiative transfer code. Alternatively, a look-up table that matches the quantity $\rho_{path}(\lambda)/T_s^{\uparrow\downarrow}(\lambda)$ at each wavelength λ to the aerosol type and optical thickness can be

pre-computed and matched.

4.1.6 Obtaining Gaseous and Scattering Transmittance

With the path radiance subtracted from the cloud radiance, it is possible to retrieve gaseous and scattering transmittance. From Eq.(4.34),

$$\rho_c(\lambda) = \frac{\pi(L_c(\lambda) - L_p^{'}(\lambda))}{T_g^{\uparrow\downarrow}(\lambda)T_s^{\uparrow\downarrow}(\lambda)F_d(\lambda)} \tag{4.38}$$

For Hyperion, at long wavelength outside the water absorption band (eg. at 854 nm) where the transmittance factor $T_g^{\uparrow\downarrow}(\lambda)T_s^{\uparrow\downarrow}(\lambda)$ is approximately 1. The cloud reflectance can be computed at this wavelength. Assuming a spectrally flat cloud reflectance, the transmittance term at shorter wavelengths can be computed by,

$$T_g^{\uparrow\downarrow}(\lambda)T_s^{\uparrow\downarrow}(\lambda) = \frac{\pi(L_c(\lambda) - L_p^{'}(\lambda))}{\rho_c(\lambda)F_d(\lambda)} \tag{4.39}$$

Using knowledge of the dominant type of gaseous absorption in the visible to NIR spectral region would enable the derivation of each individual transmittance due to gaseous absorption and scattering. In the visible spectrum, the gaseous transmittance is almost one. At the NIR end, scattering transmittance is negligible while gaseous absorption dominates. This could be seen from Figure 4.3 that the gaseous transmittance dips at 600 nm and at 720 nm and beyond. The gaseous absorption features are well understood and can easily be computed. This implies that the scattering transmittance can be computed from the total transmittance.

4.2 Implementation of Algorithm for Ikonos

The atmospheric correction was implemented on Ikonos multi-spectral images with 4 spectral bands and 4 meter spatial resolution. The effective wavelengths are 490.8 nm, 555.2 nm, 663.5 nm and 782.3 nm. Two images acquired on 10 march 2006 and 28 June 2006 were used. These images were acquired at 11:38 am and 11:48 am Singapore time. For these two days, there were near concurrent field measurements of water leaving reflectance using the hand-held spectrometer. The two passes can be seen in Figure 4.4.

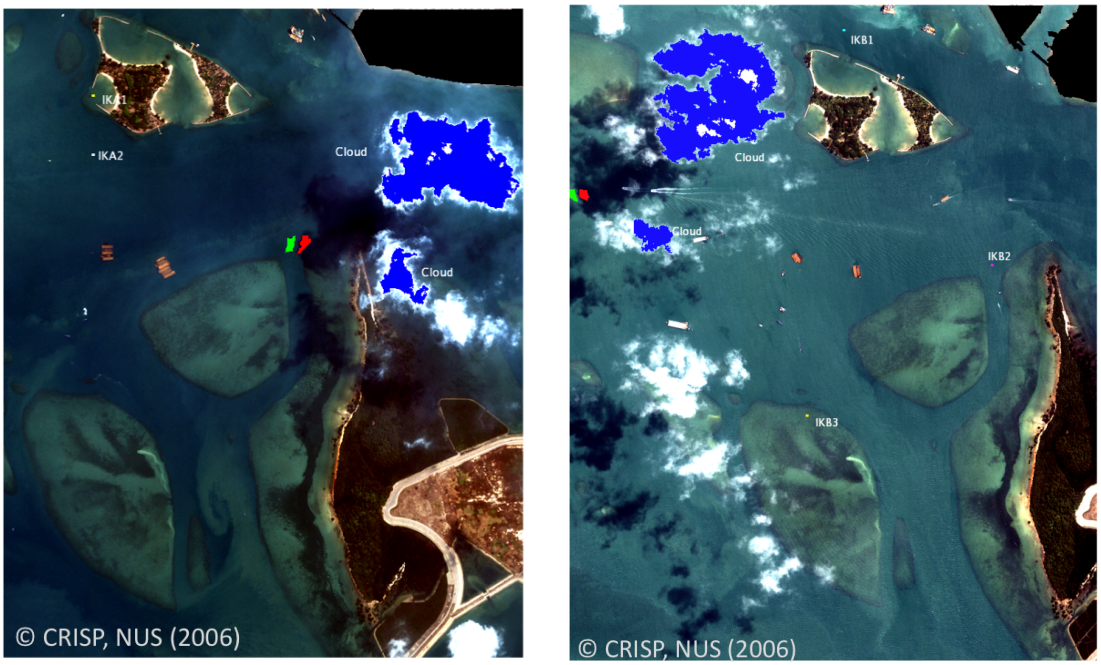

(a) Ikonos image (IK1) dated 10th March 2006, 11:38

(b) Ikonos image (IK2) dated 28th June 2006, 11:48

FIGURE 4.4: Ikonos image used for study

For Ikonos images, only the path radiance and water leaving reflectance were derived as the wide spectral bandwidths do not permit retrieval of atmospheric properties. The bandwidths are are 71.3 nm ,88.6 nm , 65.8 nm and 95.4 nm for the four spectral bands.

4.2.1 Selecting the cloud,shadow and water spectra

Radiance (in digital counts) of the spectral bands over cloud and shadow areas were collected from the two images. The blue regions in the images shown in Figure 4.4 are where the clouds spectra were collected. The shadow and water area are the red and green regions respectively. The radiance collected can be seen in Figure 4.5 and Figure 4.5(b) . The cloud spectra in raw count could be seen to be similar in spectral shape. For the cloud spectrums, at least 10000

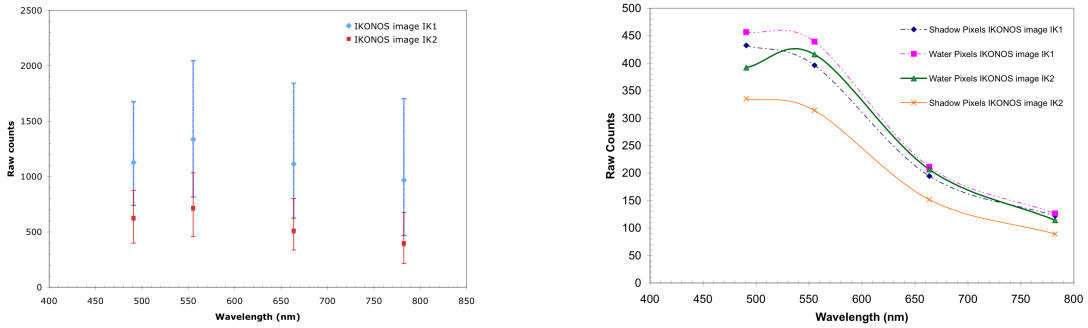

(a) Typical Spectrum of Cloud pixels (Ikonos) (b) Spectrum of Shadow and Water pixels (Ikonos)

FIGURE 4.5: Spectrums from Ikonos image (Cloud,Shadow and Water in Raw counts)

spectra were collected depending on the availability of clouds in the image. For the water and shadow spectra were averaged over an area of around 150 pixels. Extra care was taken to make sure that the water and shadow areas are adjacent with similar water properties.

4.2.2 Deriving the Path radiance

In this section, the path radiance $L'_p(\lambda)$ derived from the two Ikonos imageries is shown. The values of $L'_p(\lambda)$ were derived using three values of $\alpha(780)$:1.0, 1.2 and 1.4 The choice of $\alpha(780)$ had little effect on the the radiance derived as seen in Figure 4.6 and Figure 4.7.

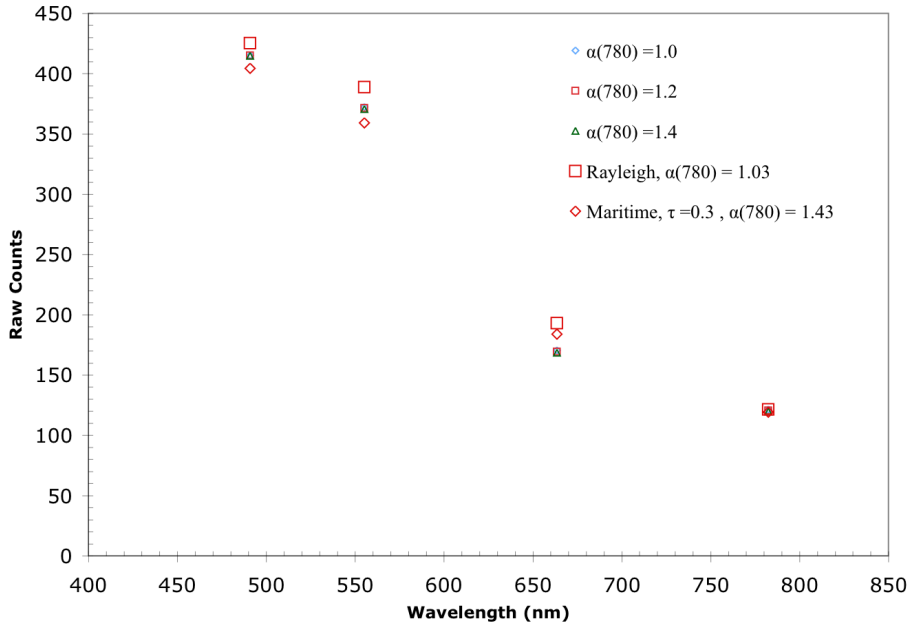

FIGURE 4.6: Derived $L'_p(\lambda)$from 100306 with different $\alpha(780)$ used

Figure 4.6 shows that $L'_p(\lambda)$ derived with different values of $\alpha(780)$ are practically the same. The path radiance was also computed using typical values of $\alpha(\lambda)$ obtained from the COART code shown in Figure 4.2 . Two cases were considered: Rayleigh scattering and maritime aerosol with 0.3 optical thickness at 550 nm. The results indicate that with a similar $\alpha(780)$

for Rayleigh scattering and Maritime Aerosols of Optical thickness of 0.3, the $L'_p(\lambda)$ are very different from the values using our new cloud and shadow method. In fact a spread of 15 counts were obtained for the $L'_p(\lambda)$ derived using typical $\alpha(\lambda)$ value derived from radiative transfer code. This may seem to be a negligible amount. However, the signal from the water pixels are low. For this case, the water leaving radiance is in the order of 50-60 counts, hence this spread would translate to about 20 $\%$ of the water leaving radiance.

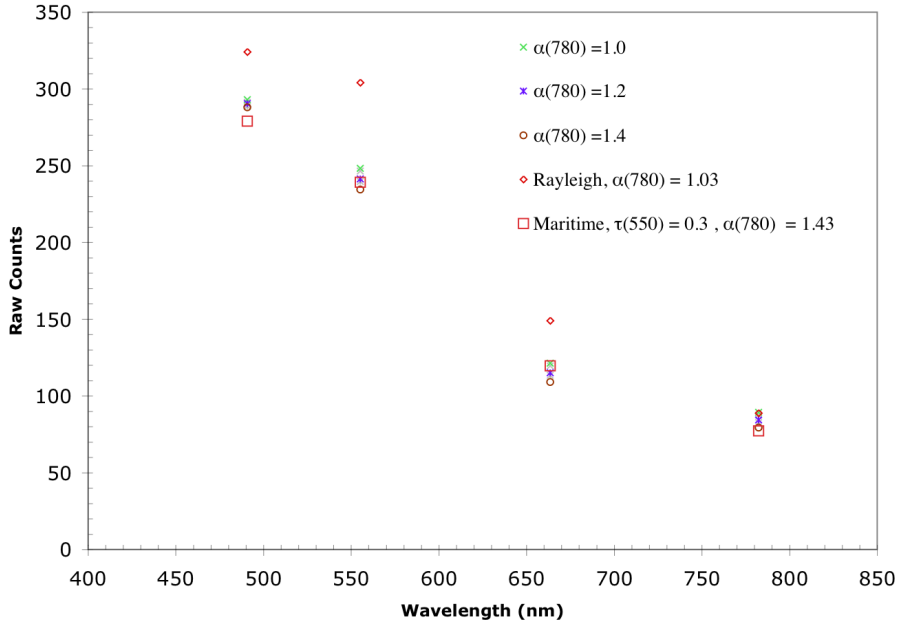

FIGURE 4.7: Derived $L'_p(\lambda)$from 280606 with different $\alpha(780)$ used

For the imagery IK2, the spread is even larger as seen in Figure 4.7. The $L'_p(\lambda)$ was derived from many cloud pairs assuming a value of 1.2 for , and the spread is shown in Figure 4.8.

From Figure 4.8 , the spectral shapes of the various derived path radiance are similar. The small

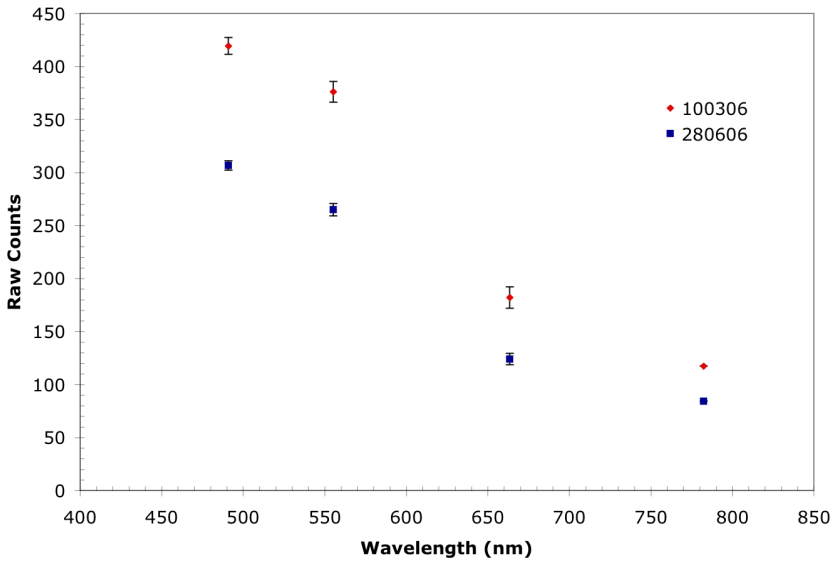

FIGURE 4.8: Derived $L'_p(\lambda)$ from the two images

error bar is an indicator that the derived radiance are close to each other and the algorithm is relatively stable with so many pairs of cloud spectrum tested.

The $\alpha(\lambda)$ values were examined, the derivation of $L'_p(\lambda)$ would means that the $\alpha(\lambda)$ values could be derived from Eq.(4.9). The values of $\alpha(\lambda)$ are shown in Figure 4.9 .

The derived value of $\alpha(\lambda)$ suggests that they are close to each other in-spite of different choice of $\alpha(780)$. However the values from IK2 suggest slight deviation for different values of $\alpha(780)$ used. It is seen that at the red wavelength, the values of $\alpha(\lambda)$ shot up.

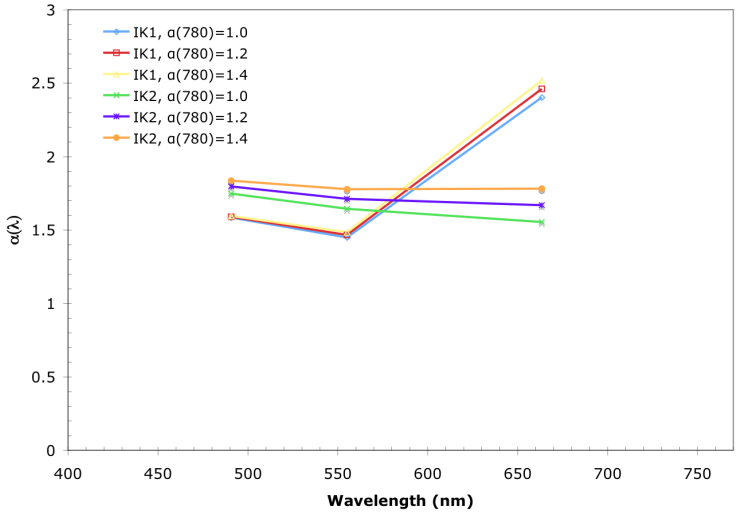

FIGURE 4.9: Derived $\alpha(\lambda)$ from the two images

4.3 Implementation of algorithm for Hyperion

The algorithm was implemented on a set of hyperspectral data from the Hyperion sensor. There are 70 channels from the visible to near infared region (356 nm to 1058 nm). The resolution of each pixel is about 30 m, and the image has a swath of 7.75 km. The image was acquired on 2 June 2001 at 03:41 UTC. A total of 1900 cloud pixels were used. As seen in Figure 4.11 , the radiance signals from cloud pixels are about 3 times as large as those from the water or shadow pixels. The range of raw counts from cloud pixels are indicated as the error bars in Figure 4.11(a). The shadow pixels are darker than the water pixels as expected. The shadow and water pixels radiance shown in Figure 4.11, were each being averaged over 100 pixels.

According to the mathematical formulation described in the previous section where $L'_p(\lambda)$ was derived, three values of $\alpha(854)$ computed were used to examine how the choice of $\alpha(854)$ would affect the results. Derived$L'_p(\lambda)$ are shown in Figure4.12. From this figure, it is observed that the values of $\alpha(854)$ does not have much influence on the values of $L'_p(\lambda)$ derived. The values derived are quite close, in fact the data points overlap with each other. The spread of the derived $L'_p(\lambda)$ with $\alpha(854)$ of 1.2 is shown in Figure 4.13. Likewise the $\alpha(\lambda)$ for rayleigh scattering and maritime optical thickness of 0.3 were used to compute the $L'_p(\lambda)$. The $L'_p(\lambda)$ derived for rayleigh scattering is far away from that derived by the cloud and shadow method. If the values of $\alpha(\lambda)$ for maritime aerosol with optical thickness of 0.3 were used, the difference in $L'_p(\lambda)$ from cloud and shadow method would be about 50 to 60 digital counts. This is about 40 $\%$ of the water radiance which is in the order of 200 counts. Hence a large error would be incurred in deriving the water reflectance. From Figure 4.13, it can also be observed that the

path radiance is not really reliable at wavelengths around 480 nm. This conclusion was made since path radiance has a exponential or power law function behavior, sloping down from 400 nm to 900 nm and there are any dips in the spectrum in the spectral range of (400 nm -440 nm). It appeared that the choice of values of $\alpha(854)$ does not affect the derived $L'_p(\lambda)$. This could be attributed to the fact that it has little effect on the estimated values of $L'_p(854)$.

FIGURE 4.10: Hyperion image used for implementation, with blue region denoting cloud areas sampled for test, the red and green region denoting the shadow and water region

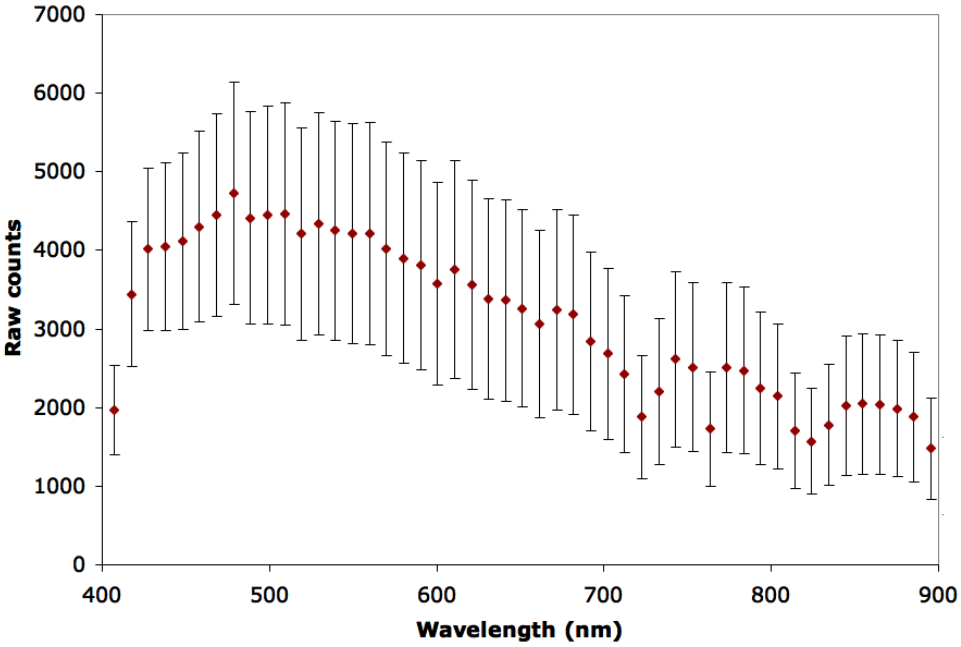

(a) Typical Spectrum of Cloud pixels

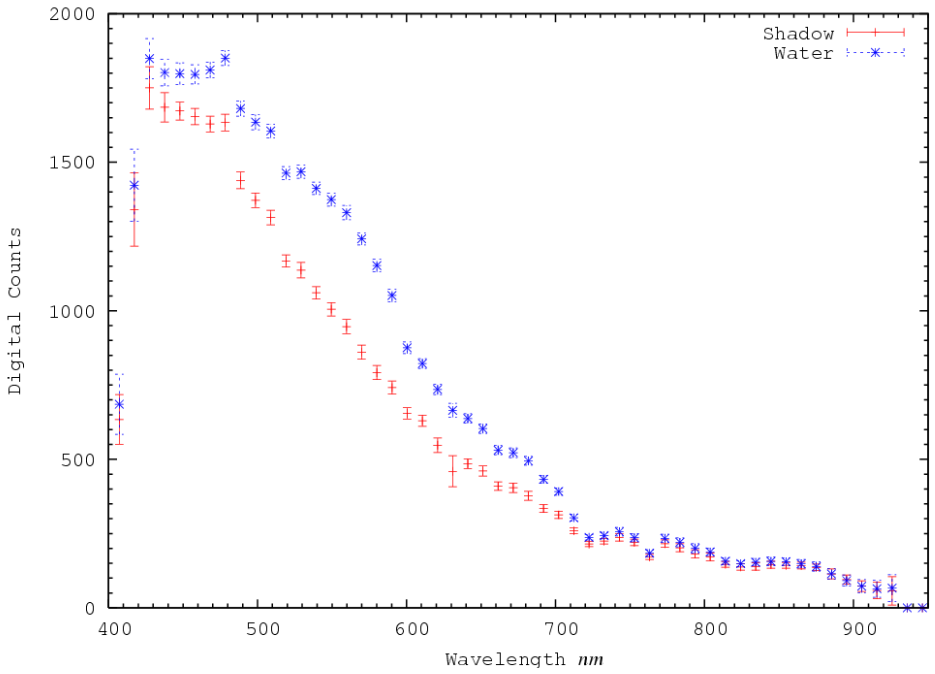

(b) Typical Spectrum of Shadow and Water pixels

FIGURE 4.11: Typical Spectrums from Hyperion image (Cloud, Shadow and Water in Raw counts)

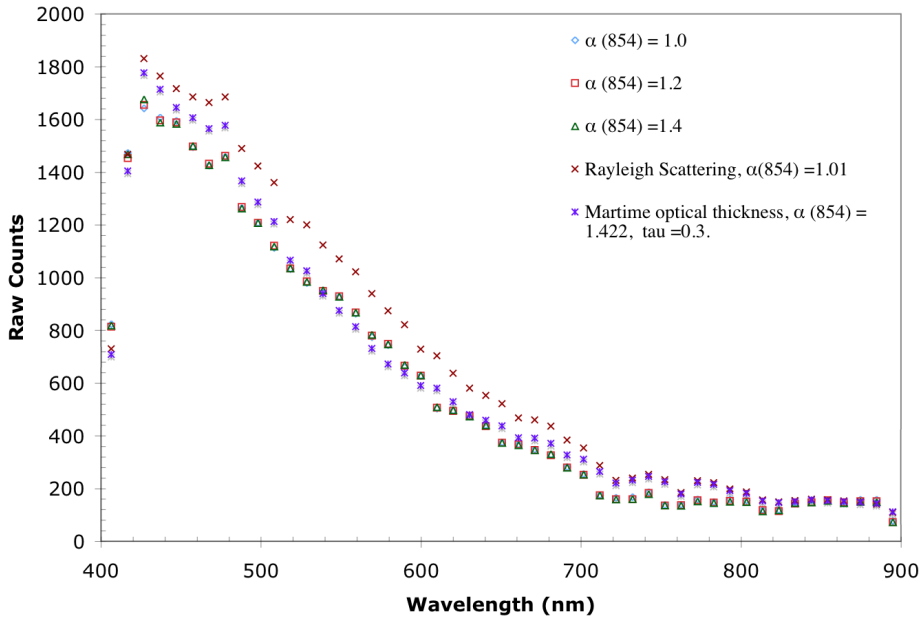

FIGURE 4.12: $L'_p(\lambda)$ derived with different values of $\alpha(854)$

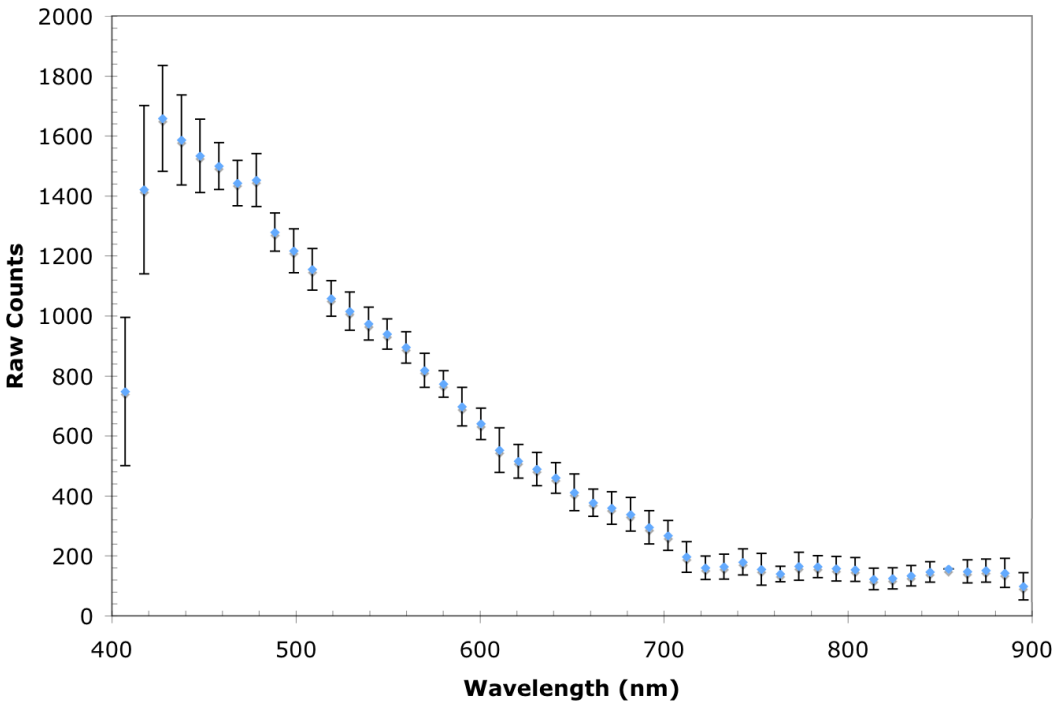

FIGURE 4.13: $L'_p(\lambda)$ derived

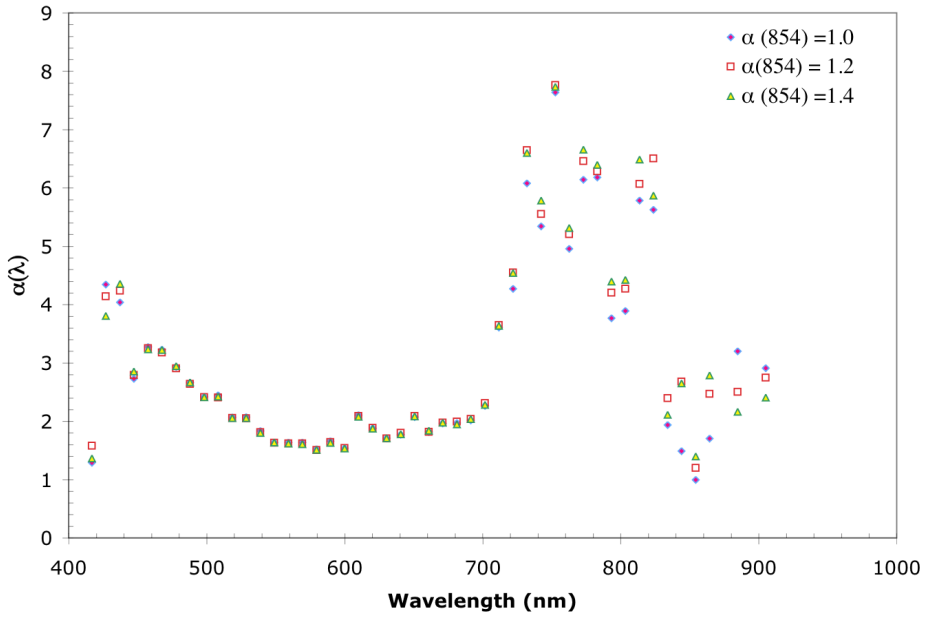

FIGURE 4.14: $\alpha(\lambda)$ derived

The values of $\alpha(\lambda)$ are shown in Figure 4.14 where the values are close to each other in spite of different values of $\alpha(854)$ used. However it can be seen that at wavelengths 600 nm and 700 nm beyond, $\alpha(\lambda)$ shot up and surprisingly coincides with the absorption due to atmospheric gases. This indicates that the values of $\alpha(\lambda)$ is plagued by gaseous absorption.

4.4 Results of atmospheric correction

4.4.1 Ikonos Image

Water leaving reflectance retrieved from two Ikonos images(Figure 4.15) using our cloud and shadow image was compared to field measurements made during field trips conducted over Singapore coastal waters. Five field measurement points were available which were made near the time of satellite image acquisition. Two of the points were sampled around the time image acquisition, while the measurements for three other points were made about 3 hours after the satellite imagery was acquired. The field measured reflectance spectra was aggregated to give the equivalent at the 4 spectral bands using Ikonos band response function (Peterson, 2001).

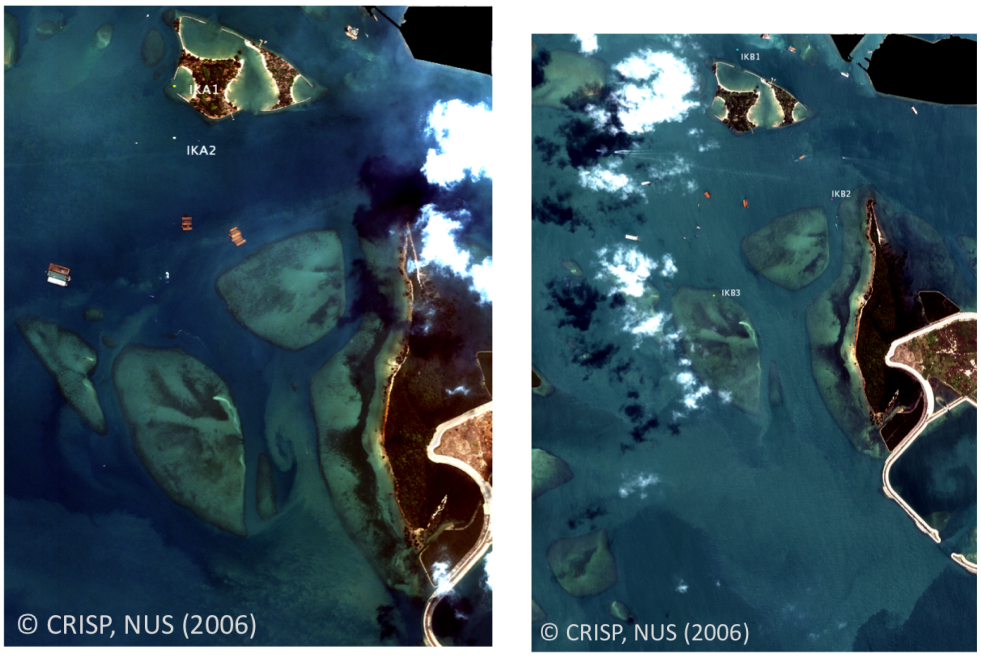

(a) Ikonos image (IKA) dated 10th March 2006, 11:38

(b) Ikonos image (IKB) dated 28th June 2006, 11:48

FIGURE 4.15: Ikonos images used for study

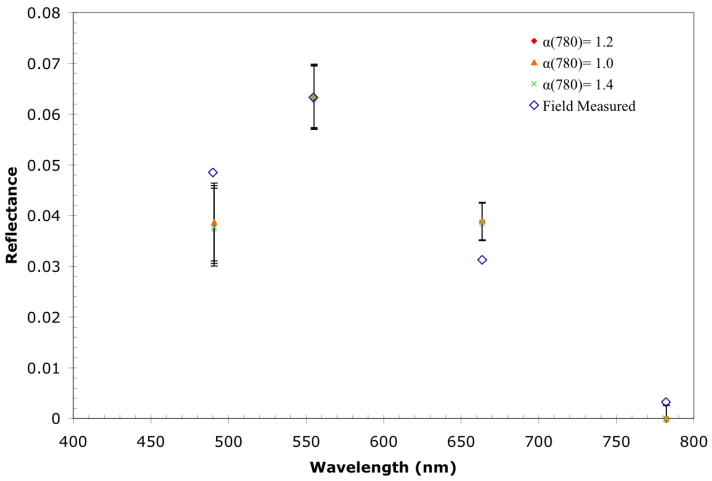

FIGURE 4.16: Pt IKA1 from image IKA, with derived reflectance with different value of $\alpha(780)$ and field measured reflectance

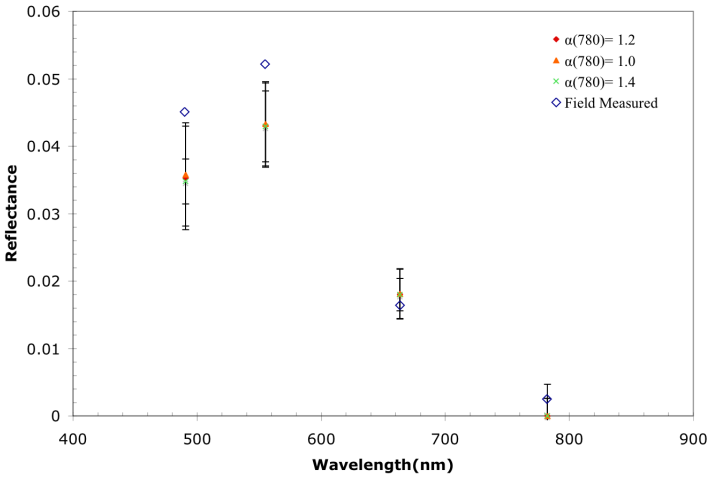

FIGURE 4.17: Pt IKA2 from image IKA, with derived reflectance with different value of $\alpha(780)$ and field measured reflectance

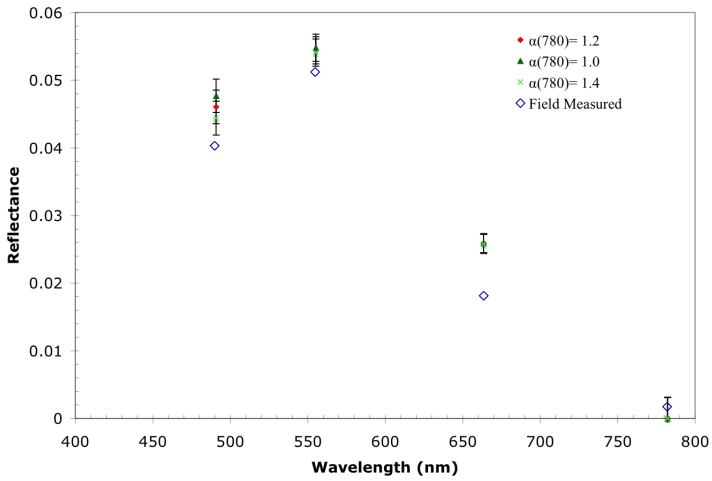

FIGURE 4.18: Pt IKB1 from image IKB, with derived reflectance with different value of $\alpha(780)$ and field measured reflectance

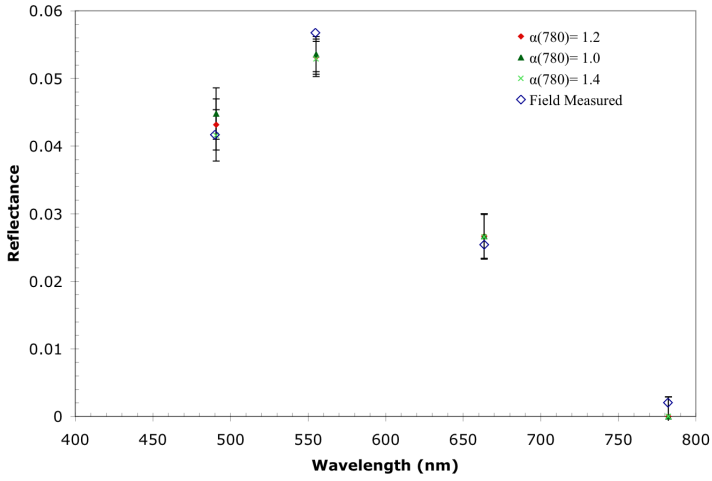

FIGURE 4.19: Pt IKB2 from image IKB, with derived reflectance with different value of $\alpha(780)$ and field measured reflectance

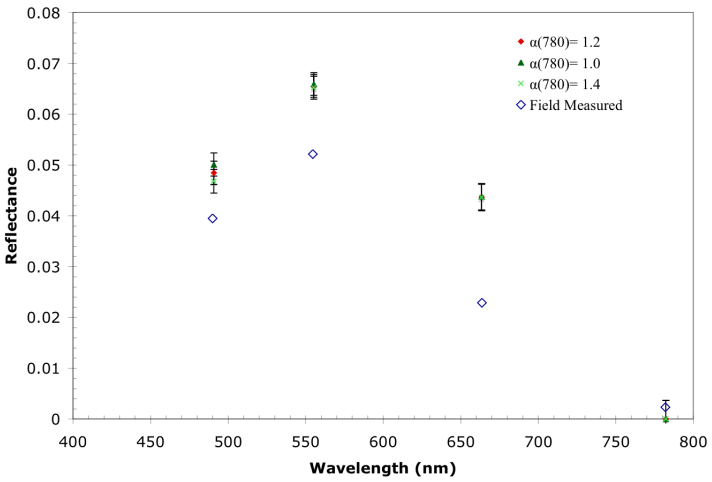

FIGURE 4.20: Pt IKB3 from image IKB, with derived reflectance with different value of $\alpha(780)$ and field measured reflectance

Figure 4.16 to Figure 4.20 show the field measured reflectance $\rho_w(\lambda)$ of the five sampling points aggregated to the Ikonos bands and the corresponding water reflectance derived using three different values of $\alpha(780)$. The error bars show the variation of the actual raw counts where a 3 by 3 pixel window was averaged over the sampling points. As seen from the figures, the derived reflectance agreed quite well with the field measured ones. A percentage error was computed between the derived and the field measured reflectance for all the three wavelengths and the five spectra. The percentage error for $\alpha(780)$ is 1.2 is 20.0 $\%$. For values of $\alpha(780)$ are 1.0 and 1.4 , the errors are 19.3 $\%$ and 20.0 $\%$, respectively.

4.4.2 Hyperion Image

The results of implementing the cloud and shadow method for deriving water reflectances from hyperspectral image data acquired by the Hyperion sensor are presented in this section. The Hyperion image was acquired on 2 June 2001 at 03:41 UTC, a RGB composite image of the study site is shown in Figure 4.21.

For illustration, results obtained from 8 locations in Figure 4.21) are discussed here. Different locations were selected for comparison. The locations were selected based on points of interests such as over coral reefs, open water, channels between coral reefs and the locations where field measurements were routinely measured. The points were selected due to the fact that they cover shallow and deep waters.

Atmospheric correction for the same image was also performed with TAFKAA. The correction was done by selecting the option which allowed the aerosol optical thickness aerosol optical

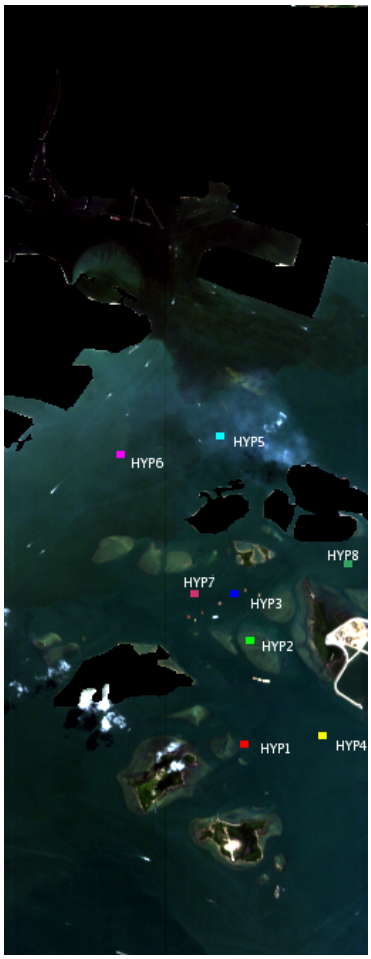

FIGURE 4.21: Hyperion image showing various ROIs

thickness and model to be derived for each pixel. These optical properties were derived based on choosing two spectral where the radiance signals are assumed to be solely from the atmosphere. The two wavelengths are 750 nm and 865 nm respectively. Correction for atmospheric water vapour absorption was, however not performed, because the program requires longer wavelength channels near 1030 nm were not available for this particular image. Though the omission of water vapour correction is not critical for correct aerosol estimation as 750 nm and 865 nm are transparent atmospheric windows, the corrected reflectance would be filled with dips arising from the absorption effects.

These results are shown in Figure 4.22 and Figure 4.23 . For each location the derived water reflectance is averaged over a 4 by 4 pixel square and the mean reflectance is plotted in the figures.

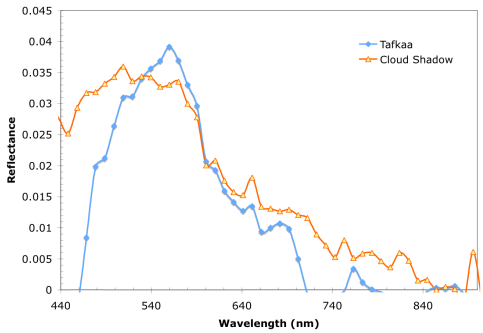

(a) HYP1

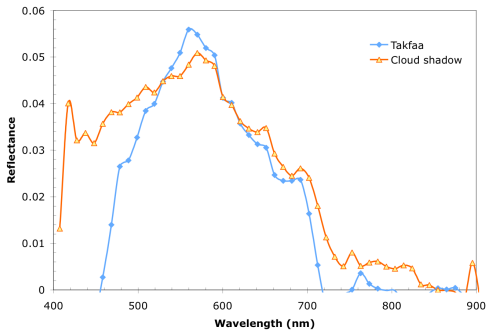

(b) HYP2

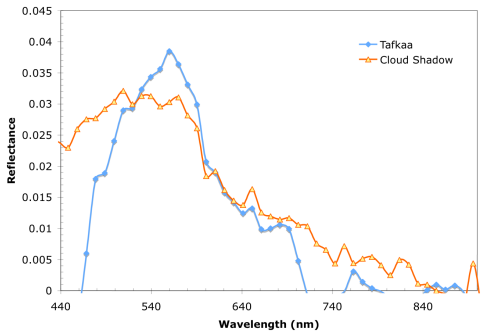

(c) HYP3

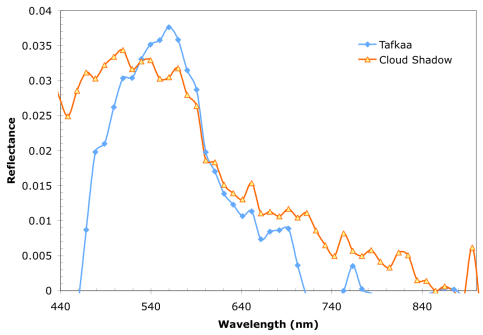

(d) HYP4

FIGURE 4.22: Atmospheric Correction Results I from Hyperion

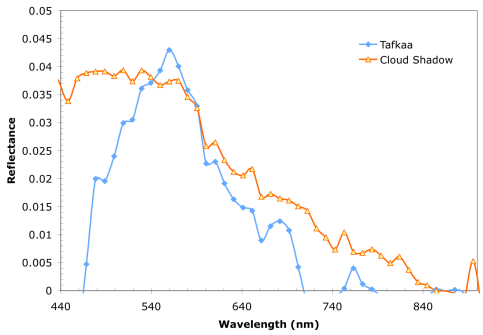

(a) HYP5

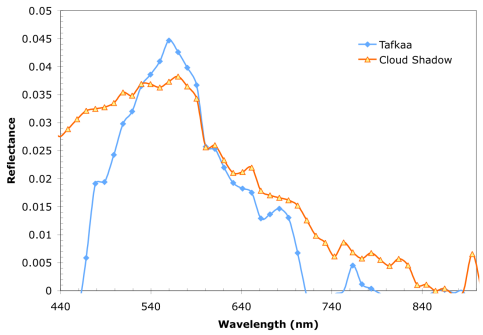

(b) HYP6

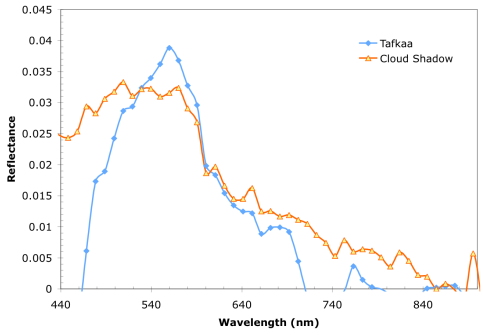

(c) HYP7

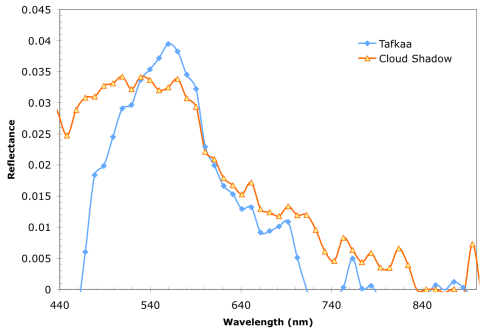

(d) HYP8

FIGURE 4.23: Atmospheric Correction Results II from Hyperion

For wavelengths less than 460 nm, the reflectance obtained using TAFKAA was overcorrected resulting in negative water reflectance values. For spectra obtained via the cloud and shadow method, the values are above zero. The cloud and shadow method is able to remove the absorption features of water vapour and oxygen as shown in the retrieved water reflectance spectra. TAFKAA is capable of correcting the gaseous absorption . However, the option to perform gaseous absorption was not turned on due to the lack of the spectral bands beyond 950 nm in our Hyperion data, which are needed to correct for the absorption features. Hence, the reflectance retrieved by TAFKAA shows negative values in the region beyond 700 nm where absorption by atmospheric gases are prevalent. It is interesting to note that there is a smoke plume for points sampled at HYP5 and HYP6. After retrieving the water reflectance using the cloud and shadow method, the reflectance value at 854 nm was assumed to be due to surface glint and this was subtracted away from the reflectance values at all other wavelengths. This procedure is able to remove part of the effect due to the smoke plume. Some values of the plume still remains especially at the shorter wavelengths since the path reflectance of the smoke is not spectrally flat. The TAFKAA method was able to tackle the extra path reflectance due to aerosols in the plume.

The reflectance derived by the two methods was compared at four wavelengths, which are 500 nm, 550 nm, 600 nm and 650 nm. A total of about 100000 points were used for comparison. The reflectance retrieved using the cloud and shadow method was regressed against that from TAFKAA. Two different regressions were done. The first was to take reflectance derived by TAFKAA to be the true values and the R^2 was computed between these two values. The next was to fit a linear line through the scatter plot of cloud and shadow derived reflectance versus

the TAFKAA retrieved. Another R^2 term was computed for this. The corrected reflectance maps from both methods and the scatter plots can be seen in Figure 4.24 to Figure 4.27 .

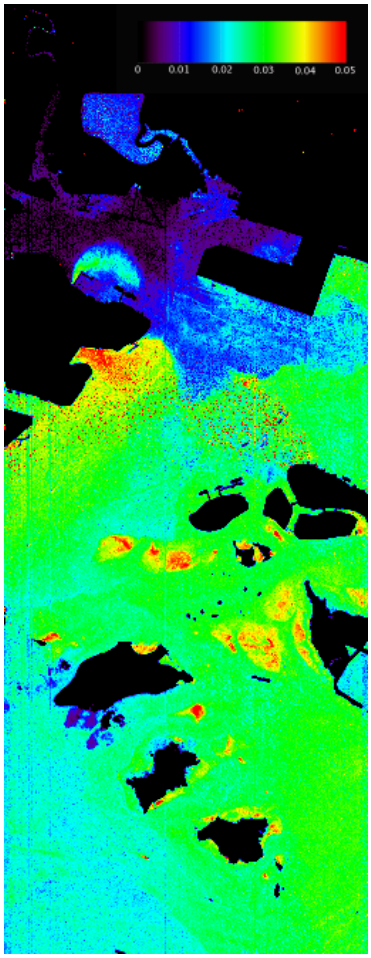

(a) Derived Reflectance map from TAFKAA

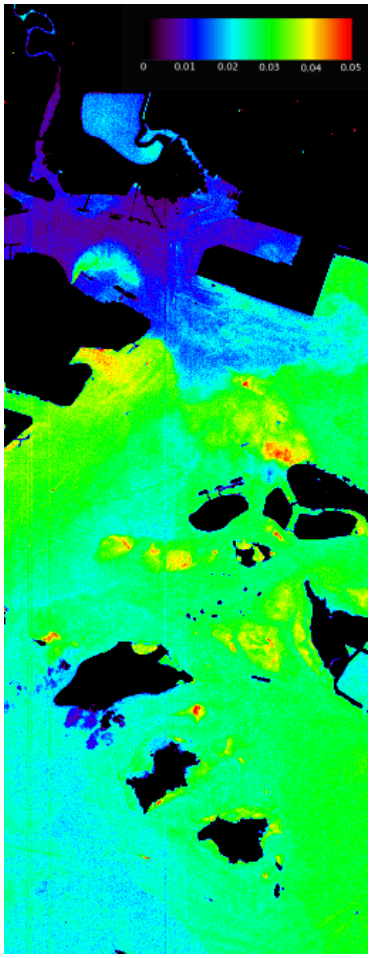

(b) Derived Reflectance map from Cloud and shadow method

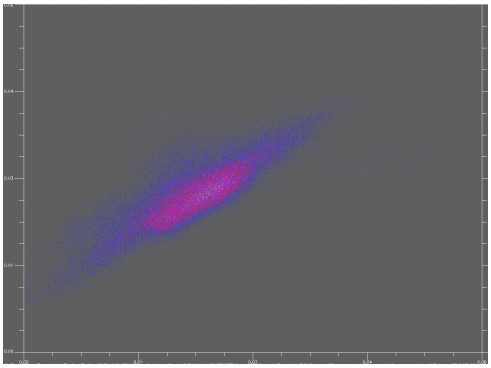

(c) Scatterplot Cloud and shadow vs TAFKAA reflectance (Density)

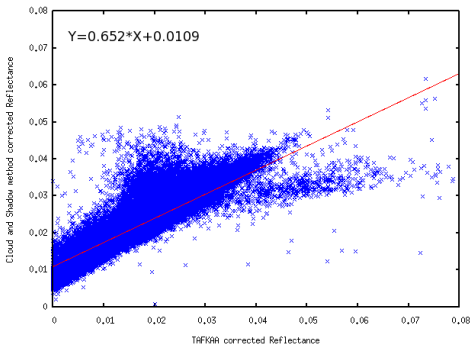

(d) Scatter plot Cloud and shadow vs TAFKAA reflectance

FIGURE 4.24: Comparing TAFKAA and Cloud and shadow derived reflectance, reflectance map and scatter plot at 500 nm

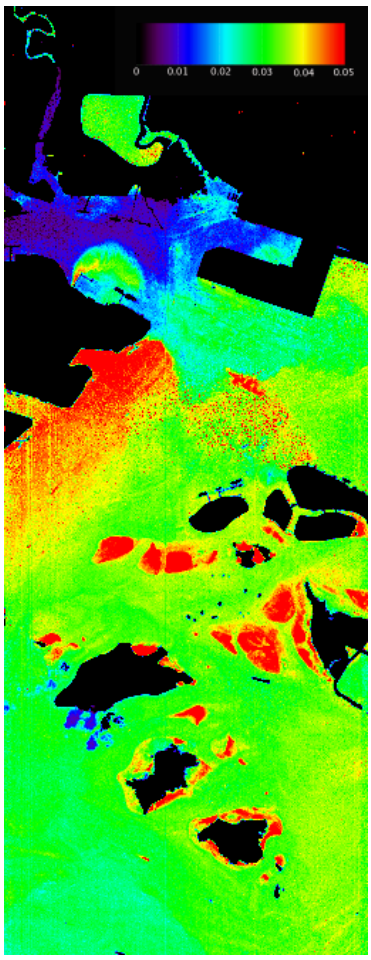

(a) Derived Reflectance map from TAFKAA (550 nm)

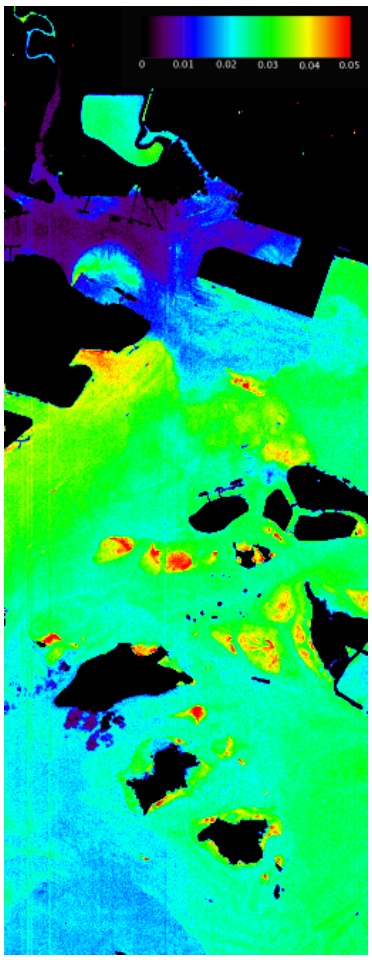

(b) Derived Reflectance map from Cloud and shadow method (550 nm)

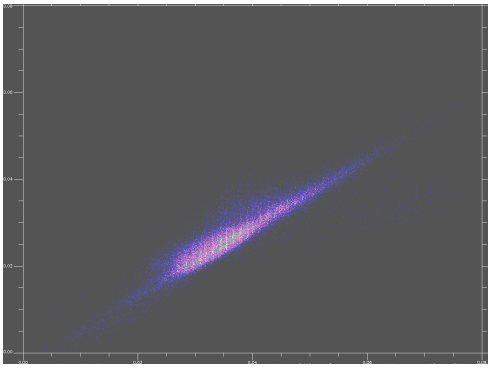

(c) Scatterplot Cloud and shadow vs TAFKAA reflectance (Density)

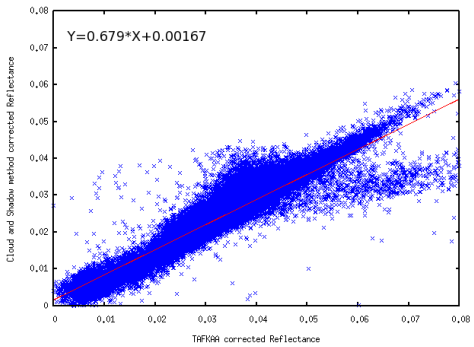

(d) Scatterplot Cloud and shadow vs TAFKAA reflectance

FIGURE 4.25: Comparing TAFKAA and Cloud and shadow derived reflectance, reflectance map and scatterplot at 550 nm

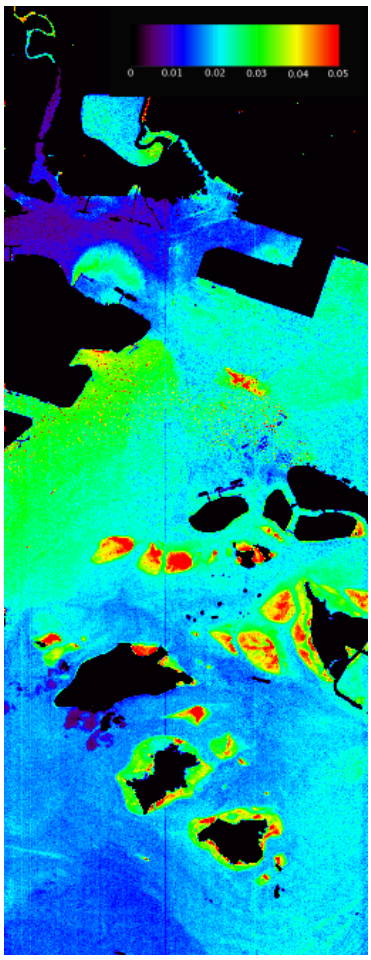

(a) Derived Reflectance map from TAFKAA

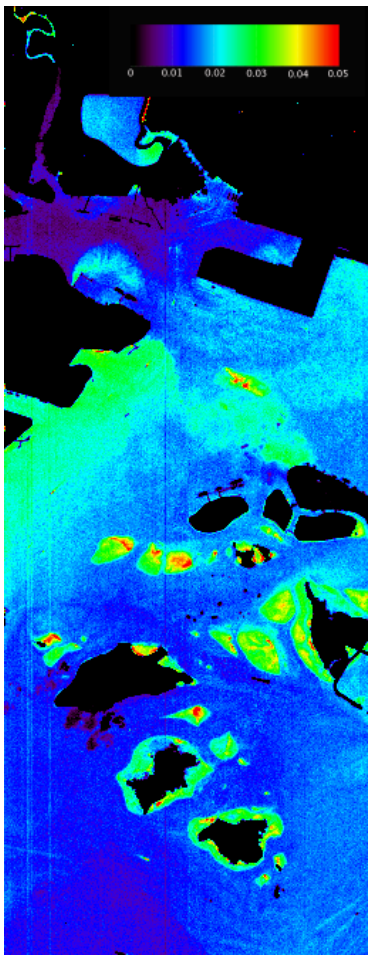

(b) Derived Reflectance map from Cloud and shadow method

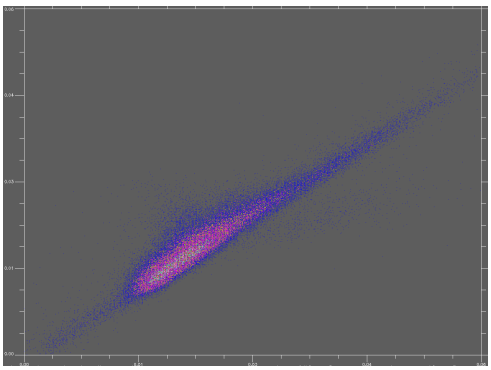

(c) Scatterplot Cloud and shadow vs TAFKAA reflectance (Density)

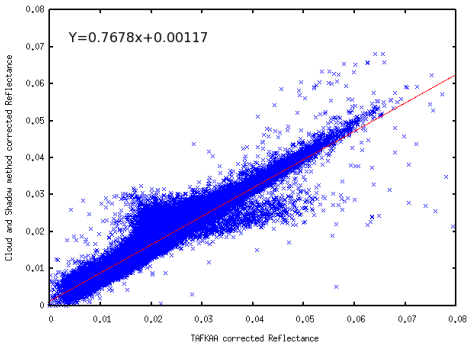

(d) Scatterplot Cloud and shadow vs TAFKAA reflectance

FIGURE 4.26: Comparing TAFKAA and Cloud and shadow derived reflectance, reflectance map and scatterplot (600 nm)

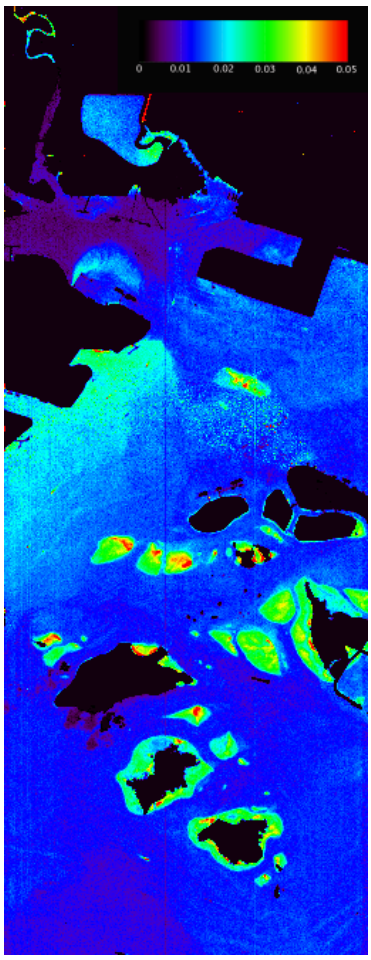

(a) Derived Reflectance map from TAFKAA

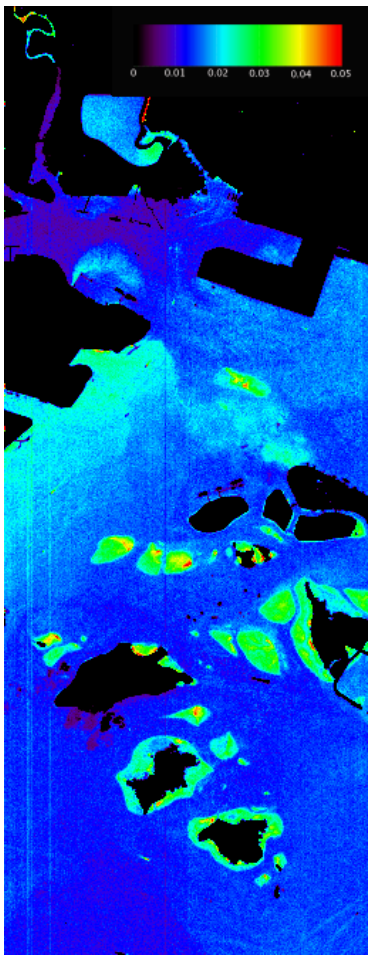

(b) Derived Reflectance map from Cloud and shadow method

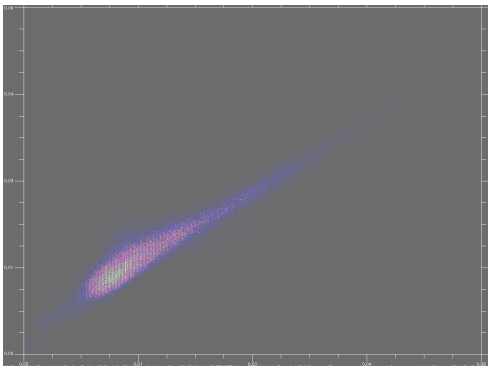

(c) Scatterplot Cloud and shadow vs TAFKAA reflectance (Density)

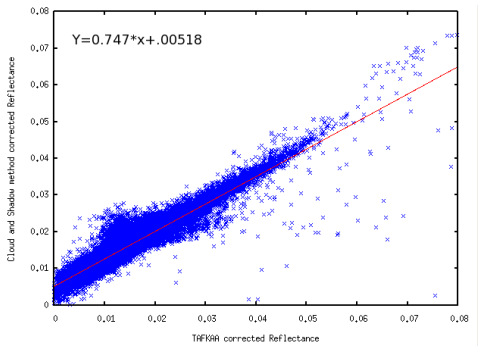

(d) Scatterplot Cloud and shadow vs TAFKAA reflectance

FIGURE 4.27: Comparing TAFKAA and Cloud and shadow derived reflectance, reflectance map and scatterplot (650 nm)

TABLE 4.1: R^2 values for the different regressions. The first regression was done between the cloud and shadow corrected reflectance and the TAFKAA corrected reflectance. The second is for the linear line fitted in the scatterplots shown in earlier figures.

Wavelength (nm)	Regression 1 R^2	Regression 2 R^2
500	0.940	0.982
550	0.845	0.987
600	0.935	0.987
650	0.968	0.988

The regression errors shown in Table 4.1 indicate that the values retrieved by the cloud and shadow method are very close to that from TAFKAA. Though the fitted linear lines do not indicate a one to one fit, the low R^2 values for the first regression done between these two retrieved reflectance suggests the values are similar.

4.4.3 Deriving Atmospheric properties (Aerosol Type and Optical Thickness)

The aerosol type and optical thickness can be retrieved from the derived $\rho_{path}(\lambda)/T_s^{\uparrow\downarrow}(\lambda)$ by using a pre-computed look-up table as described in Section 4.1.5. TAFKAA was used to generate look-up-table consisting of $\rho_{path}(\lambda)/T_s^{\uparrow\downarrow}(\lambda)$ for different aerosol type and optical thickness. The aerosol models selected were those reported in Shettle & Fenn (1979). The various types of aerosols employed in generating the LUT were coastal, Coastal-A, Maritime and Urban each with relative humidity of 80 $\%$, 90 $\%$ and 98 $\%$. The aerosol loading parameterized by τ at 550 nm was varied from 0 to 0.3 at a interval of 0.002. In order to find the best fit aerosol type, least square error fitting was performed between the modeled and derived path reflectance using the

following cost function,

$$\chi = \sum_{\lambda=450}^{\lambda=700} \{\log \left[\frac{\rho_{path}(\lambda)}{T_s^{\uparrow\downarrow}(\lambda)}\right]_{derived} - \log \left[\frac{\rho_{path}(\lambda)}{T_s^{\uparrow\downarrow}(\lambda)}\right]_{modeled}\}^2 \tag{4.40}$$

The set of parameters (aerosol type, humidity and optical thickness) that gives the least value for the cost function χ is taken as the "correct" aerosol properties corresponding to the derived path reflectance. Note that wavelengths less than 440 nm were not used in the fitting as they were noisy. Wavelengths greater than 700 nm were also not employed as these bands are known to be plagued by water and oxygen absorption. These wavelengths were not used though Figure 4.28 showed no visible traces of the atmospheric artifact. In addition, the path reflectance for 700 nm and beyond are considered to be spectrally constant. The flatness in spectral details implies that it may not contribute important information for the retrieval of atmospheric properties such as aerosol type. Moreover at longer wavelength, data may be noisy due to the small signal measured by the sensor, hence unable to aid in the retrieval process. A total of 12 different aerosol models were used in the least square fitting. The aerosol type fitted for the three was found to be Maritime with a relative humidity of 98 $\%$ and optical thickness of 0.012. Figure 4.28 shows the derived path reflectance. The derived $\rho_{path}(\lambda)/T^{\uparrow\downarrow(\lambda)}$ for $\alpha(854)$ with value of 1.2 was shown together with the fitted values.

Figure 4.28 shows that the best fit spectrum coincides well with the reflectance spectrum derived using the cloud and shadow method. There were slight discrepancies at wavelengths near 600 nm where there is ozone absorption and beyond 700 nm where water vapour and oxygen absorption is present. The small dips showed that there is still small amount of gaseous atmospheric absorption that was not removed, however the larger dips as seen in previous figures have been removed. The severity of atmospheric gaseous absorption can be illustrated with

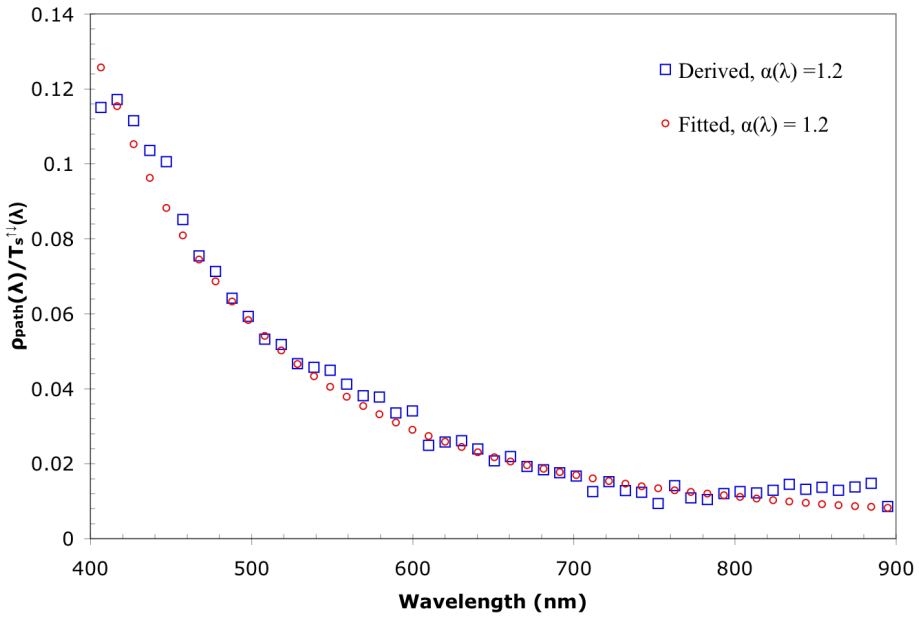

FIGURE 4.28: Fitted and Derived $\rho_{path}(\lambda)/T^{\uparrow\downarrow}(\lambda)$

some simple forward modeling. For Tropical Climate with 4.12 g/cm^2 precipitable water, the transmittance is about 26.6 and centered at 760 nm, the absorption by oxygen is about 37 $\%$. Both values are calculated from 6S (radiative transfer code) (Vermote et al., 1997). Clearly the derived path reflectance showed that such severe dips haveone been removed.

4.4.4 Deriving Atmospheric Transmittance

The atmospheric transmittance is derived using the method described in Section 4.1.6. As seen from the Figure 4.29, the 6S computed gaseous transmittance values shows that for 400 nm to 580 nm it is equivalent to one. Therefore, scattering transmittance dominates. In this spectral range it can be seen that the derived scattering transmittance from the fitting method coincide

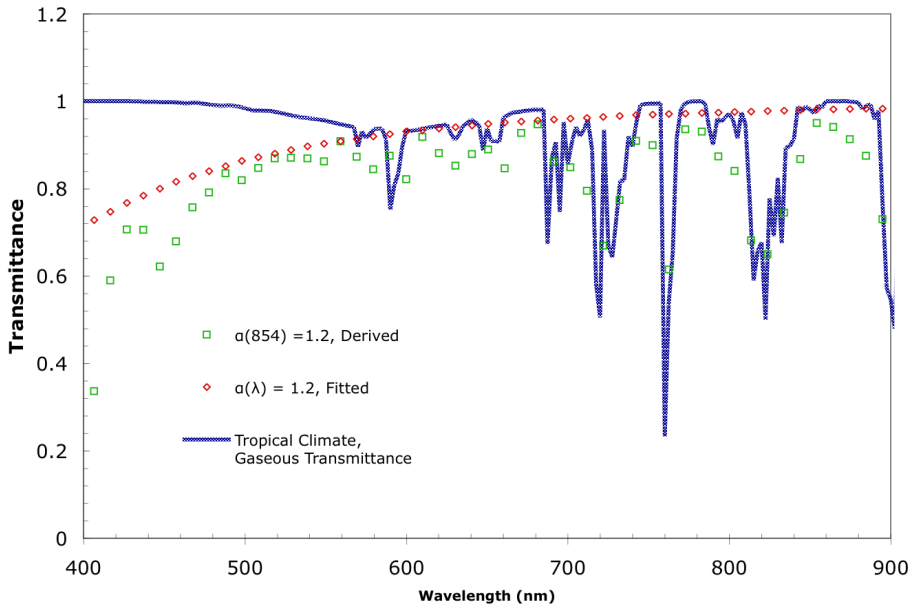

FIGURE 4.29: Scattering transmittance obtained by fitting $\rho_{path}(\lambda)/T^{\uparrow\downarrow(\lambda)}$, derived total transmittance and computed gaseous transmittance are shown.

well with the derived total transmittance. For the blue end of the spectrum, there are large variations due to noises in the spectral bands.

At wavelengths longer than 700 nm, the total atmospheric transmittance is dominated by gaseous transmittance. It can be seen that the total scattering transmittance derived is in excellent agreement with that computed using the 6S code. This suggests that the derived atmospheric transmittance is corrected for the longer wavelengths.

4.5 Conclusions

The cloud and shadow method described in this chapter is a method to derive the path radiance with minimal inputs from the visible spectral range such as solar irradiance, aerosol model and optical thickness. These atmospheric properties are usually needed to perform atmospheric correction. Subsequently, atmospheric properties, such as aerosol model, optical thickness and atmospheric transmittance are derived using two independent approaches. The results agree with each other. The accuracy of these retrieved parameters is directly related to the accuracy of the atmospheric correction method.

The comparison of Ikonos corrected reflectance with the water reflectance from field measurements showed that the cloud and shadow scheme was able to perform atmospheric correction with an error of about 20 $\%$. For the Ikonos image, atmospheric properties were not derived due to the fact that there were not enough spectral bands and the signal was averaged into four spectral bands.

For the hyperspectral satellite imagery, the corrected spectrums were benchmarked against standard methods such as TAFKAA. The corrected water reflectance in this chapter were close to that from TAFKAA for wavelength 450 - 650 nm and there were dips due to gaseous absorption seen in the NIR. Several points in Figure 4.22 and Figure 4.23 show that the cloud and shadow corrected reflectance is close to the TAFKAA corrected reflectance. A further analysis gave high R^2 values for the regression of cloud and shadow reflectance with the TAFKAA reflectance. A linear line that was regressed between these two sets of values also have high R^2 values.

The derivation of atmospheric properties, such as atmospheric transmittances by the two different methods, from Hyperion data were compared. The lookup table method gave the aerosol model, optical thickness and scattering transmittance. The derived transmittances overlap each other for the visible bands, suggesting that the scattering transmittances are similar. In the NIR range, the derived gaseous transmittances lie on the points with the Tropical model, suggesting that the derived transmittance are valid.

The effects of different values of $\alpha(NIR)$ used for the initial step of the atmospheric correction scheme was also investigated. The derived $L'_p(\lambda)$ for different values of $\alpha(NIR)$ for both Ikonos and Hyperion images are very close to each other suggesting that the algorithm is not sensitive to $\alpha(NIR)$. It was also demonstrated that by using the $\alpha(\lambda)$ values computed with different aerosol models and optical thickness for $\alpha(NIR)$ in the 1.0 and 1.4 range, the derived $L'_p(\lambda)$ is significantly different from that derived from the cloud and shadow method. This would results in significant errors in the derived water reflectance since the water leaving radiance is sensitive to errors in $L'_p(\lambda)$.

In summary, the cloud and shadow method has been successfully applied to two different sensors. It is expected that more sensors can be adapted for atmospheric corrections using the developed method.

Chapter 5

Retrieval of IOPs from remote sensing reflectance

5.1 Introduction

A method to retrieve the absorption and backscattering coefficients of water from remote-sensing reflectance is presented in this section. This method is called Split-window inversion method, in short SWIM. The method is similar to the well known matrix inversion techniques (Hoge et al., 1999a,b; Wang et al., 2005). Instead of using the whole visible spectral region for inversion, the method selected narrow windows for retrieval. The spectral windows were selected in this algorithm to enable the retrieval of optical properties from turbid and possibly shallow coastal water, avoiding the spectral region where contribution from the sea bottom reflection is the highest.

The spectral windows were selected based on in-situ measurements made during field trips.

Although the measurements may not be exhaustive and representative of all the possible types of water in Singapore, the spectral windows were chosen to possibly minimize the contribution from the sea bottom. The waters sampled has high CDOM absorption and low phytoplankton absorption, and the total absorption is lowest around the green spectral region (550 nm). The spectral region to be omitted is largely based on this observation. The spectral region used for matrix inversion is 460 nm -530 nm and the blue end at 400-460 nm was avoided due to possible contamination from inaccurate removal of surface glint.

There are many algorithms developed for the retrieval of IOPs (Lee et al., 1994, 1998a,b; Hoge & Lyon, 1996; Hoge et al., 1999a,b; Lee et al., 2002; Wang et al., 2005). In related works, matrix inversion methods were used to perform IOPs retrieval (Hoge et al., 1999a,b). Recently different spectral shapes for absorption and backscattering coefficients were used for IOPs retrievals taking into considerations of defined statistical uncertainties (Wang et al., 2005).

In this approach, simple matrix inversion was applied to the spectral window of 460 nm - 530 nm and equations relating underwater remote sensing reflectance and IOPs of water. The input water reflectance, $R_{rs}(\lambda)$, was converted to under water remote sensing reflectance using a semi-analytical equation described in chapter 2. From the underwater remote sensing reflectance, $R_{rs}(\lambda)$ was expressed as a function of absorption and backscattering coefficients which can be linearized for matrix inversion. However certain assumptions had to be made in order to set up equations for inversion. The spectral shape of CDOM absorption and backscattering were parameterized by S and Y respectively. These need to be known before the system of linear equations can be set up. With each combination of S and Y a set of IOPs were derived.

This was then used to compute the water leaving reflectance. The set that gave the least error between the computed and measured reflectance was taken to be the derived parameters. This process was done for the spectral windows of 460 nm - 530 nm and 600 nm - 650 nm. This method was tested on three datasets of water reflectance: a synthetic dataset prepared by the International Ocean Colour Coordinating Group (IOCCG) (Lee, 2005), field measured data set collected by a handheld spectrometer during our field trips, and a hyperspectral satellite data set acquired by the Hyperion sensor on-board the EO-1 satellite.

There are two main concerns pertaining to the new algorithm implemented. The first was its ability to derive IOPs over the whole visible spectral range in spite of the omission of the green spectral window. This would be examined and evaluated using the errors of retrieved absorption and backscattering coefficients. The second concern is the accuracy in which the IOPs of the shallow waters could be retrieved. This was evaluated using the experimental data with water depth that was sounded by sonar. The evaluation was also done by using HYRDOLIGHT to generate water reflectance for retrieval with different depth and albedo. The errors in retrieval were examined to see how the algorithm is able to minimize the contribution from the shallow sea bottom.

5.2 Mathematical Formulation

Either the measured or simulated $R_{rs}(\lambda)$, the above water reflectance, can be converted into the underwater reflectance,

$$r_{rs}(\lambda) = \frac{R_{rs}(\lambda)}{(\zeta + \Gamma R_{rs}(\lambda))} \tag{5.1}$$

The values ζ and Γ were taken to be 0.5 and 1.5, respectively. These values were computed for remote sensing observation angles (Morel & Gentili, 1993)

A quadratic model was developed for $r_{rs}(\lambda)$ based on monte carlo simulations (Gordon et al., 1988),

$$r_{rs}(\lambda) = g_0 u(\lambda) + g_1 u(\lambda)^2 \tag{5.2}$$

where

$$u(\lambda) = \frac{b_b(\lambda)}{b_b(\lambda) + a_{tot}(\lambda)} \tag{5.3}$$

$b_b(\lambda)$ and $a_{tot}(\lambda)$ are defined as,

$$a_{tot}(\lambda) = a_w(\lambda) + a_g(\lambda) + a_\phi(\lambda) \tag{5.4}$$

where $a_g(\lambda)$ is the absorption of both CDOM and detritus, $a_\phi(\lambda)$ is the absorption of phytoplankton. The backscattering coefficients are,

$$b_b(\lambda) = b_w(\lambda) + b_{bp}(\lambda) \tag{5.5}$$

From Eq.(5.3), $u(\lambda)$ can be rexpressed as a function of $r_{rs}(\lambda)$,

$$u(\lambda) = \frac{-g_0 + [(g_0)^2 + 4g_1 r_{rs}(\lambda)]}{2g_1} \tag{5.6}$$

and also can be written as,

$$u(\lambda)a(\lambda) + (u(\lambda) - 1)b(\lambda) = 0 \tag{5.7}$$

Hence, a system of linear equations can be set up to perform matrix operation to derive IOPs. $a_{tot}(\lambda)$ and $b_{bp}(\lambda)$ can be further partitioned into linear equations with optical models for CDOM, detritus, phytoplankton and suspended particles in water. The various optical models were briefly described in Section 2.4.

From Eq.(5.7) can written as

$$\begin{aligned} &u(a_{ag}(440)A_g + a_\phi(440)A_0 + a_w) \\ &+(u-1)(b_{bw} + (b_{bp}(550)B_p) = 0 \end{aligned} \tag{5.8}$$

The lambda dependency was taken out for brevity. The various basis functions are given below,

$$A_g = e^{s(440-\lambda)} \tag{5.9}$$

$$B_p = (\frac{550}{\lambda})^Y \tag{5.10}$$

and A_0 is the basis function for phytoplankton absorption.

The basis functions A_g and B_p are parametrized by S and Y values. Each spectral shape of CDOM and backscattering of suspended particles were determined by the values S and Y. In most cases unless extensive field work has been done in the area of interests the values are usually unknown. However, the two values are known to be typically in the ranges of 0.008 m^{-1} - 0.023 m^{-1} and -0.20 - 2, respectively. By selecting a value for S and Y from these ranges, the spectral shapes could be determined and a linear system of equations can be set up for retrieval.

The absorption coefficient function for phytoplankton is linearlized in the following manner. Absorption coefficients for phytoplankton are computed by using the following formula (Lee, 1994),

$$a_\phi(\lambda) = a_\phi(440)a_0(\lambda) + a_\phi(440)\ln(a_\phi(440))a_1(\lambda) \tag{5.11}$$

$a_\phi(440)$ was varied from 0.001 m^{-1} to 0.20 m^{-1}. Each of the absorption spectrum generated was then divided by $a_\phi(440)$ to obtain a basis function. This basis function was then averaged for all the different normalized spectrums to give,

$$a_\phi(\lambda) = a_\phi(440)A_0(\lambda) \tag{5.12}$$

This new function generates absorption coefficient of about 3 $\%$ from the original model in the wavelength region between 400 to 520 nm but rise to about 20 $\%$ for the wavelength ranges of 550 to 600 nm when $a_\phi(440)$ is above 0.1 m^{-1}.

The linear equation from Eq.(5.7) can be express in a matrix as ,

$$\begin{pmatrix} u_1 A_0^{'} & u_1 A_g & u_1 B_p \\ \vdots & \vdots & \vdots \\ u_n A_0^{'} & u_n A_g & u_n B_p \end{pmatrix} \begin{pmatrix} a_\phi(440) \\ a_g(440) \\ b_{bp}(550) \end{pmatrix} = \begin{pmatrix} u_1 a_w - (u_1 - 1) b_w \\ \vdots \\ u_n a_w - (u_n - 1) b_w \end{pmatrix} \tag{5.13}$$

From Eq.(5.13), parameters such as $a_\phi(440)$, $a_g(440)$ and $b_{bp}(550)$ can be derived from $R_{rs}(\lambda)$. The matrix inversion method has been used widely (Hoge & Lyon, 1996; Hoge et al., 1999a,b; Wang et al., 2005) though the final linear form may differ from our formulation. The linear equation was also obtained by solving the quadratic equation in Eq.(5.6). In the first linear matrix inversion method (Hoge & Lyon, 1996), spectral shapes of CDOM was assumed, i.e a value for S is assumed and Y is estimated from band ratios of reflectance (Hoge & Lyon, 1996) and the matrix inversion was applied to three spectral bands at 412, 490 and 555 nm.

In recent years, a method (Wang et al., 2005) which allows the parameters S and Y to vary was implemented, and certain statistical criteria was imposed on the $a_\phi(440)$, $a_g(440)$ and $b_{bp}(550)$ retrieved for different permutations of S and Y. The criteria was set such that the parameters such as $a_\phi(440)$, $a_g(440)$ and $b_{bp}(550)$ used to compute the $r_{rs}(\lambda)$ must give values of up to 10

or 20 $\%$ variation of the measured $r_{rs}(\lambda)$.

In the approach developed in this thesis, the values of S and Y was allowed to vary and the matrix inversion was applied to the spectral window of 460 -530 nm. This was to avoid contribution from the sea bottom and to avoid any errors that might be induced in the retrieval from overestimation of surface glint correction in the range of 460 to 530 nm. Moreover this was developed in consideration for Hyperion data which is usually noisy in the first few bands of the visible range.

5.3 Selecting the Spectral Window

For shallow coastal waters, the total reflectance has contribution from the sea bottom. The penetration of light in water is dependent on the diffuse attenuation, which in turn is largely determined by the absorption and backscattering coefficients of water. Since the inherent optical properties of water depend on optical components, such as phytoplankton, CDOM and suspended particles, light penetration is also dependent on the abundance of these components. The field surveyed points around the waters of Singapore has high CDOM content and are highly backscattering in nature which has been discussed in Chapter 3. A plot of the total absorption of the waters measured with pure water component is made in Figure 5.1 .

From Figure 5.1 , we can see that that the waters sampled has the least absorption centered at 550 nm. There are some sites with high absorption even at wavelength of 530 nm , for example site S2A and site S2b. However there are some sites which has lower absorption at this same

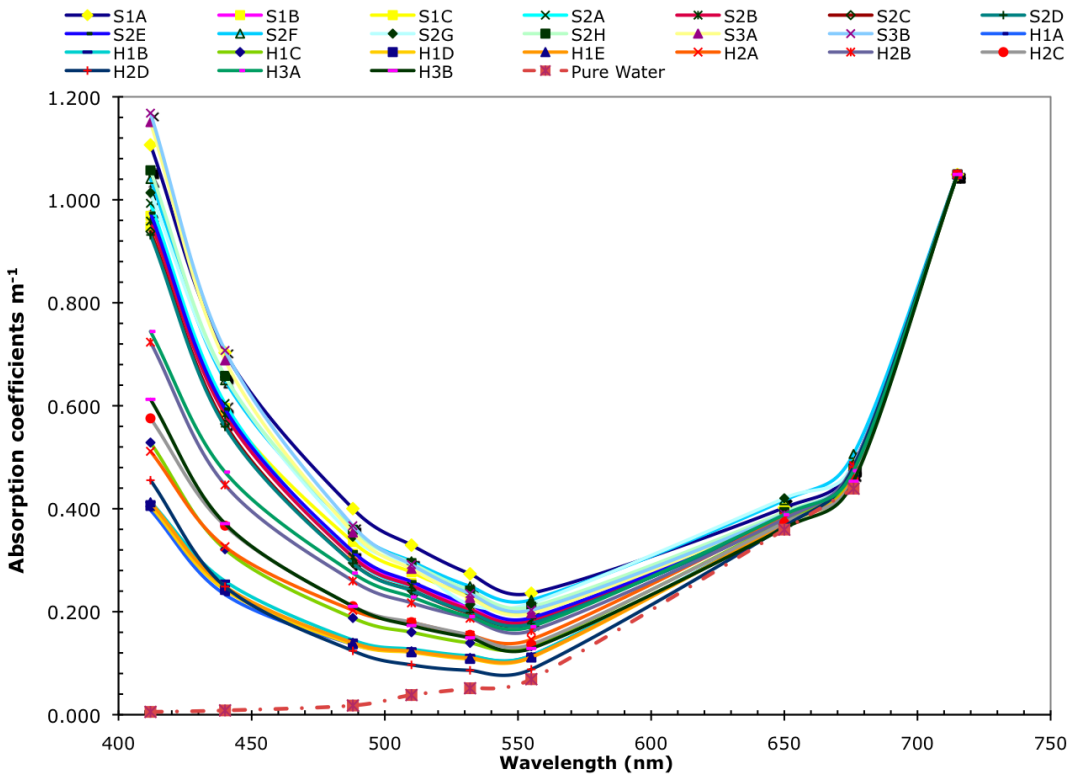

FIGURE 5.1: Absorption coefficients of water sampled in Singapore

wavelength. We have to decide on an encompassing spectral window to avoid and also to consider the practicality of implementation, which in this case is the sufficient number of spectral bands. We took the lower range of 530 nm for one end of the spectral window and 600 nm for the other due to high water absorption. In summary, the spectral range of 540 to 600 nm is to be avoided for the retrieval of IOPs. The effectiveness of this assumption would be examined at a later section where the SWIM algorithm will be compared to one that uses this avoided spectral window.

The contribution from bottom reflectance depends not only on the diffuse attenuation coefficient but also on the bottom reflectance relative to the water reflectance. The reflectance of shallow

water can be expressed as (Maritorena et al., 1994),

$$R_{rs}(\lambda, H) = R_{rs}^{\infty}(\lambda) + (R_b(\lambda) - R_{rs}^{\infty}(\lambda)) \exp^{-2KH} \tag{5.14}$$

where K is the diffuse attenuation, H is the water depth, $R_b(\lambda)$ is the reflectance of the sea bottom and $R_{rs}^{\infty}(\lambda)$ is the reflectance of the deep waters having the same optical properties as the shallow water. The ratio of the reflectance of the shallow water of depth H to that of deep water is,

$$\psi(\lambda, H) = \frac{R_{rs}(\lambda, H)}{R_{rs}^{\infty}(\lambda)} \tag{5.15}$$

This ratio is an indicator of the percentage contribution of shallow waters with respect to the total reflectance, and would be useful in later sections to examine how this ratio would affect the accuracy of IOPs retrieved.

5.4 Implementation of algorithm

After the matrix inversion framework is set up, the inversion algorithm can be applied to $R_{rs}(\lambda)$ in the wavelength range of 460 nm to 530 nm. The wavelength range of 400 nm to 450 nm was avoided as this is the region where the error in correcting surface may potentially be the largest due to huge component of reflected skylight in the radiance measured off the water surface. For each set of S and Y, the matrix inversion will derive values for $a_g(440)$, $a_\phi(440)$ and $b_{bp}(440)$. The matrix inversion was performed using the SVD (Single Value Decomposition) technique. The retrieved IOPs together with S and Y are used to model the $R_{rs}(\lambda)$.

The solution space of S and Y was partitioned into small segments of 0.0001 and 0.02 respectively. The retrieved parameters together with S and Y can be used to model $R_{rs}(\lambda)$ in the region

of 460 nm - 530 nm and 600 nm - 660 nm. The range of 670 nm -750 nm was avoided due to chlorophyll fluorescence. The modeled $R_{rs}(\lambda)$ was matched up with the input or measured spectrum by computing the error according to the equation

$$\chi = \sum_{i=0}^{N} |(R_{rs}^{model}(\lambda)) - (R_{rs}^{measured}(\lambda))| \tag{5.16}$$

and the retrieved IOPs are compared to measured ones by,

$$\Omega = \left(\frac{\sum_{i=0}^{N} [log_{10}(IOP^{model}(\lambda)) - log_{10}(IOP^{measured}(\lambda))]^2}{N-2} \right)^{0.5} \tag{5.17}$$

Ω is known as RMSE, which is the root mean squared error in the log space. This method for computing error will be used to quantify the accuracy of IOPs retrieval as the RMSE have been widely used in the ocean colour community.

5.5 Results

5.5.1 Synthetic dataset

The algorithm was tested on the synthetic data set developed by the International Ocean Color Coordination Group (IOCCG). The data set includes spectral IOPs and remote-sensing reflectance generated at 10 nm intervals. The algorithm was applied to the 500 sets of simulated $R_{rs}(\lambda)$. The RMSE was computed for the retrieved IOPs defined by Eq.(5.17) where $R_{rs}(\lambda)$ is replaced by IOPs in the equation. The input IOPs represent a huge spread of water types from clear ocean waters to turbid, CDOM laden and phytoplankton rich waters. The absorption coefficient, $a_{tot}(\lambda)$-$a_w(\lambda)$, ranged from 0.000992 m^{-1} to 0.9837 m^{-1} and the backscattering

coefficient ranged from 0.000521 m^{-1} to 0.1316 m^{-1} at 550 nm.

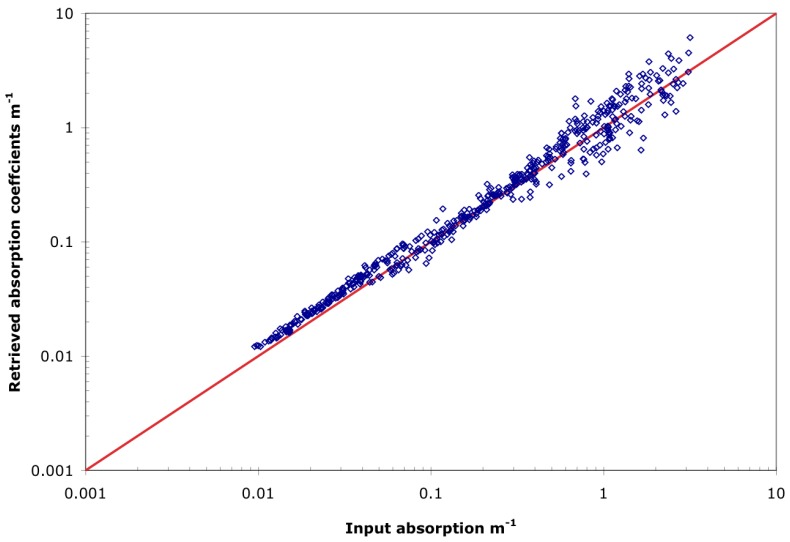

FIGURE 5.2: Scatterplot of retrieved absorption vs input absorption at 440 nm

Scatterplots between the retrieved and the input absorption and backscattering are shown in Figure 5.2 and Figure 5.3.

Both figures showed that the retrieved IOPs lie along the 1:1 line and the RMSE is low. Moreover, retrieval was done without the use of spectral window centered around 550 nm, suggesting that the IOPs retrieved at this wavelength is reasonably constrained with low errors at 0.111 and 0.059 respectively. The errors at various wavelengths were tabulated in Table 5.1.

The errors shown in Table 5.1 indicate that the IOPs retrieved over the visible spectral regime

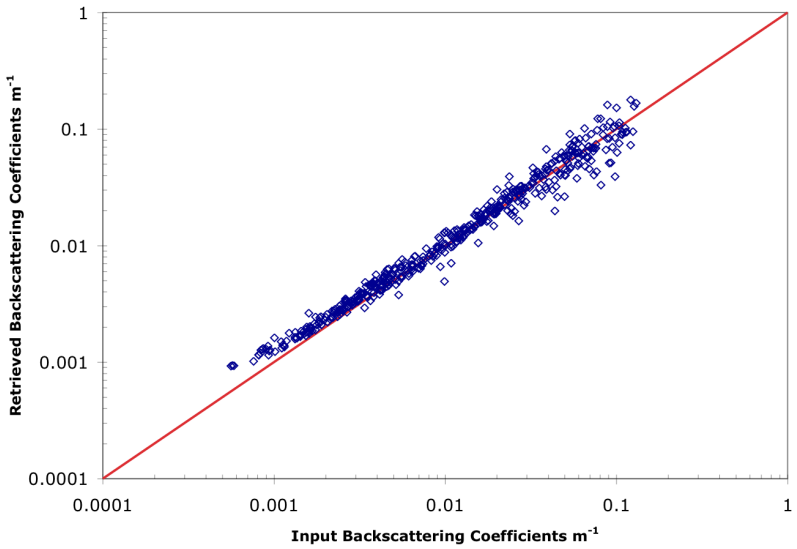

FIGURE 5.3: ScatterPlot of input backscattering vs retrieved backscattering at 550 nm

are low and suggests that the spectral shapes of various IOPs are well modeled. However there are large errors in retrieving $a_\phi(\lambda)$ and it could be due to large amount of $a_g(\lambda)$ present. A comparison was made with several algorithms that were implemented on the same dataset to see how the algorithm fared.

Table 5.2 shows that the SWIM algorithm implemented performed well compared to other algorithms. Compared to the similar methods that used linear matrix inversion (Hoge & Lyon, 1996; Wang et al., 2005) the SWIM method performed more or less the same. In spite of the selection of preferred spectral windows to minimize the contribution of the sea bottom reflectance to the total signal measured, the algorithm was able to retrieve IOPS in the omitted

TABLE 5.1: RMSE errors of IOPs retrieval

Wave (nm)	RMSE $a_{tot}(\lambda)$-$a_w(\lambda)$	RMSE $b_{bp}(\lambda)$
440	0.111	0.170
490	0.090	0.136
550	0.132	0.090
650	0.288	0.060

windows. The method is robust as shown and justified by the errors in Table 5.2.

TABLE 5.2: RMSE comparison between algorithms reported in the IOCCG report, current algorithm for synthetic data set.

Method	$a_{total}(440)$	$a_g(440)$	$b_{bp}(440)$	$b_{bp}(555)$
Simple algorithm(Morel & Maritorena, 2001)	0.224	–	–	–
K_d method(Loisel & Stramski, 2000)	0.119	–	0.123	0.138
Neural network(Doerffer et al., 2002)	0.052	0.230	0.082	–
Linear matrix(Hoge & Lyon, 1996)	0.140	0.161	0.150	–
Linear matrix (statistical Selection)(Wang et al., 2005)	0.106	0.141	0.125	
MODIS S.A(Carder et al., 1999)	0.059	0.135	0.042	–
QAA(Lee et al., 2002)	0.056	0.088	0.064	0.063
GSM(Maritorena et al., 2002)	0.115	0.145	0.152	–
S.A(Sathyendranath & Platt, 1997)	0.166	0.348	0.160	–
(Work in this Chapter)	0.111	0.197	0.0712	0.0540

5.5.2 Field measured data

Field measured IOPs were used to validate the algorithm. The field measured reflectance data provides an opportunity to test the algorithm as the data was collected in an environment with fast varying magnitude of downwelling light and strong tidal current that might affect the Ac-9 measurements of IOPs. This would be a good test for the robustness of the algorithm, especially with consideration that error may incur in radiometric measurements. This adds on to the confidence of the validity of the field measurements if the retrieved IOPs corresponds well to the measured data. Additional field data was also added to the pool of data from P. Hantu and P. Semakau. The field data added is from cyreene reefs. They are sites M1A, M1B and M1C and are shown together with the rest of the remote sensing reflectance at P. Hantu and P. Semkau in Figure 5.4.

The remote sensing reflectance at sites M1A, M1B and M1C is much higher that than from P. Hantu and P. Semakau . The absorption and backscattering coefficients from these three sites are much higher than the rest of the sites sampled. The absorption coefficients can be seen in Figure 5.5 and the backscattering coefficients are shown in Figure 5.6 together with the rest of the IOPs used for validating the algorithm.

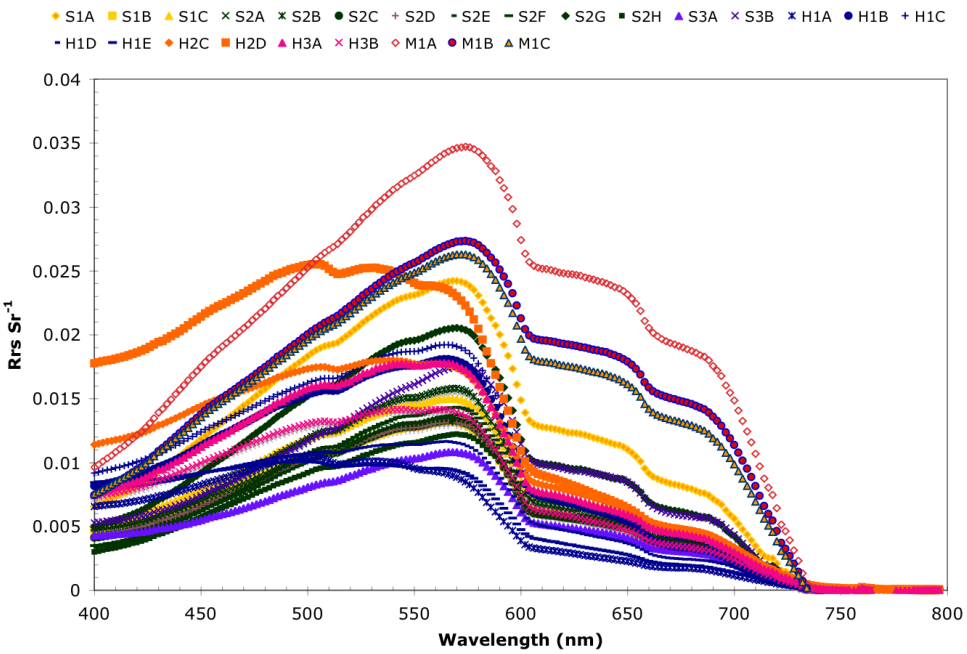

FIGURE 5.4: $R_{rs}(\lambda)$ used for IOPs retrieval

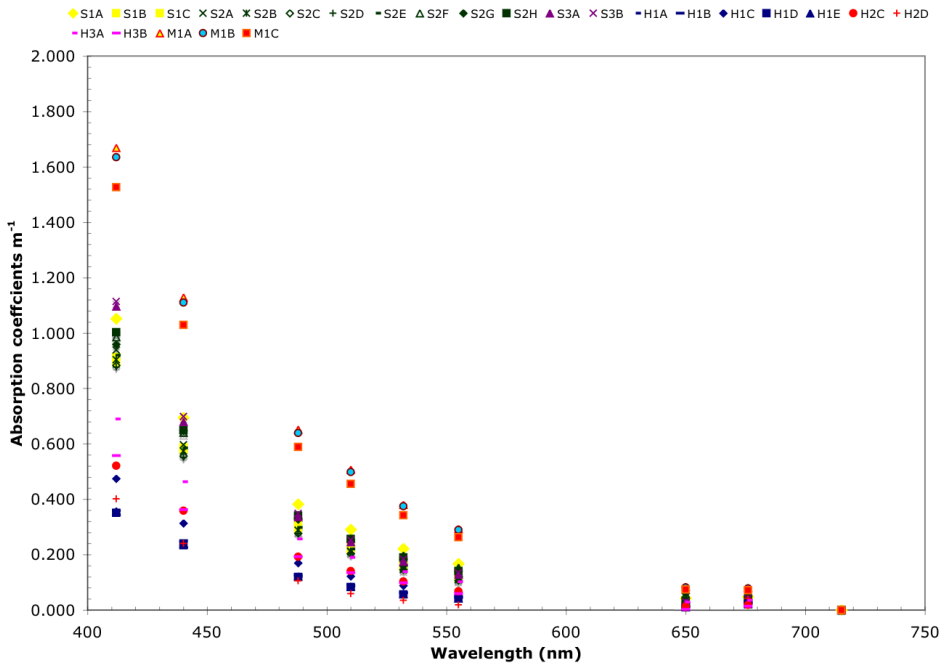

FIGURE 5.5: Absorption coefficients used to validate IOPs retrieval

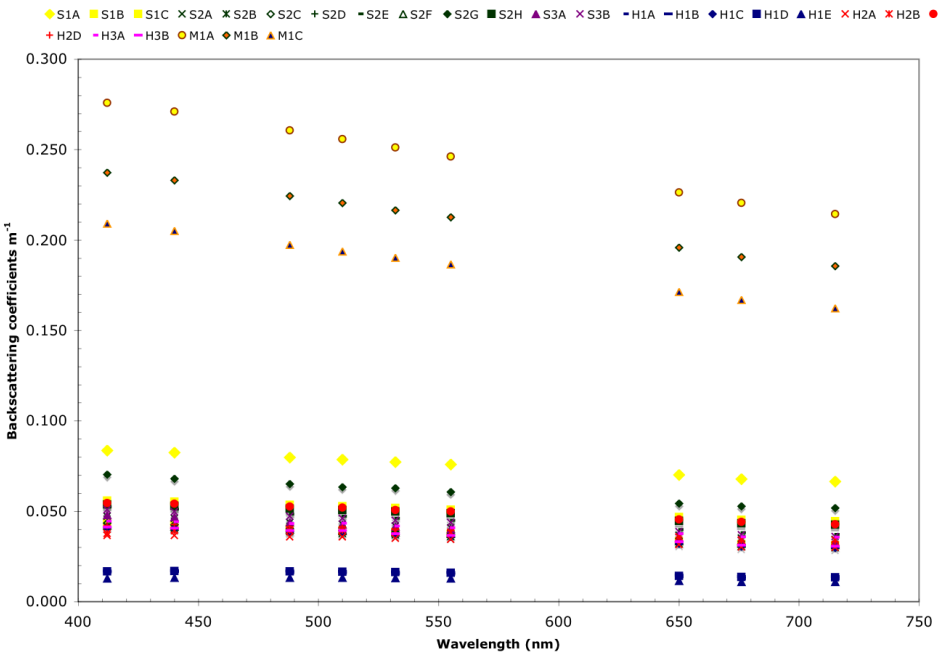

FIGURE 5.6: Backscattering coefficients used to validate IOPs retrieval

The reflectance spectrum consists of both shallow and deep waters. This allows the SWIM to be validated on the accuracy of retrieval of IOPs from shallow waters. The MIM (Matrix inversion method) was also implemented for the spectral windows from 460 to 590 nm. This was carried out so as to include the omitted green spectral window. In this way, the SWIM algorithm can be tested for its effectiveness in retrieving IOPs over shallow waters. The scatterplot of the absorption coefficients retrieved by the two methods are shown in Figure 5.7 and Figure 5.8.

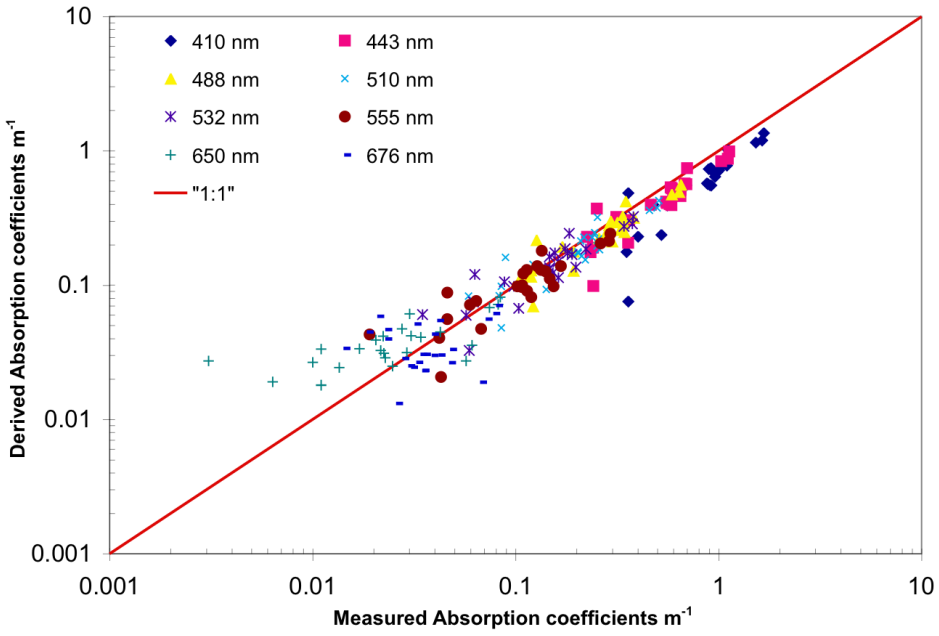

FIGURE 5.7: Retrieved Absorption versus Measured Absorption, using SWIM

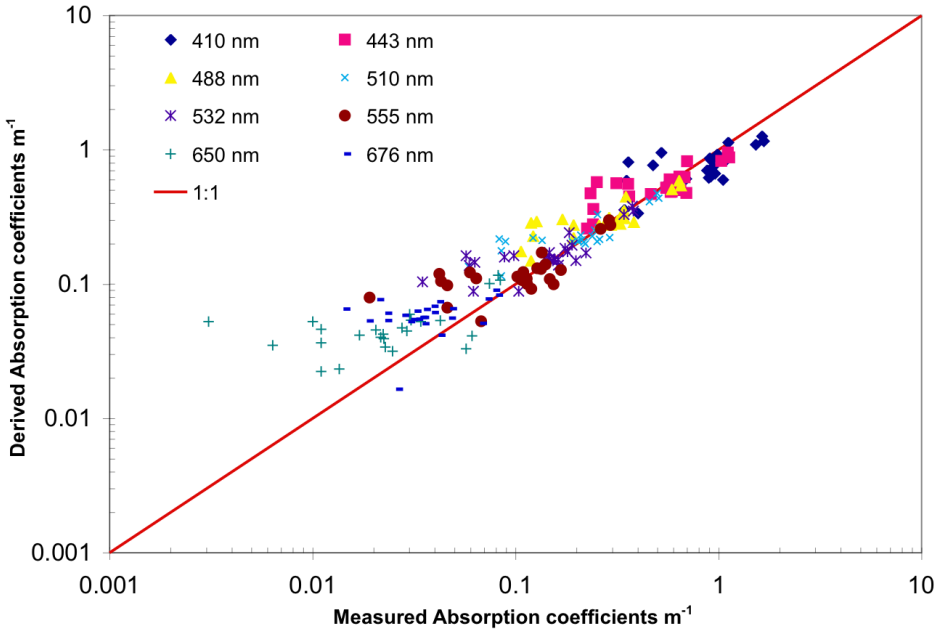

FIGURE 5.8: Retrieved Absorption versus Measured Absorption, using MIM

On comparison, both the approaches retrieved IOPs that lie around the 1:1 line. This indicates that the retrieval algorithm is well implemented. There is a spread of points for the wavelengths between 650 and 676 nm, where water absorption is high and the absorption coefficients measured are low. Most of the absorption coefficients measured at these two wavelengths are about 0.06 m^{-1} and the accuracy of the Ac-9 is 0.01 m^{-1}. These two factors would imply high errors at these wavelengths. The RMSE are shown in Table 5.3

TABLE 5.3: RMSE of absorption coefficients from SWIM and MIM

Wavelength (nm)	RMSE (SWIM)	RMSE (MIM)
412	0.178	0.151
440	0.121	0.138
488	0.108	0.152
510	0.125	0.173
532	0.142	0.194
555	0.174	0.218
650	0.374	0.426
676	0.256	0.293

The RMSE of the retrieved absorption coefficients suggest that the SWIM algorithm did modestly better than MIM for wavelengths greater than 550 nm. The scatterplots for retrieved backscattering coefficients from both methods are shown in Figure 5.9 and Figure 5.10.

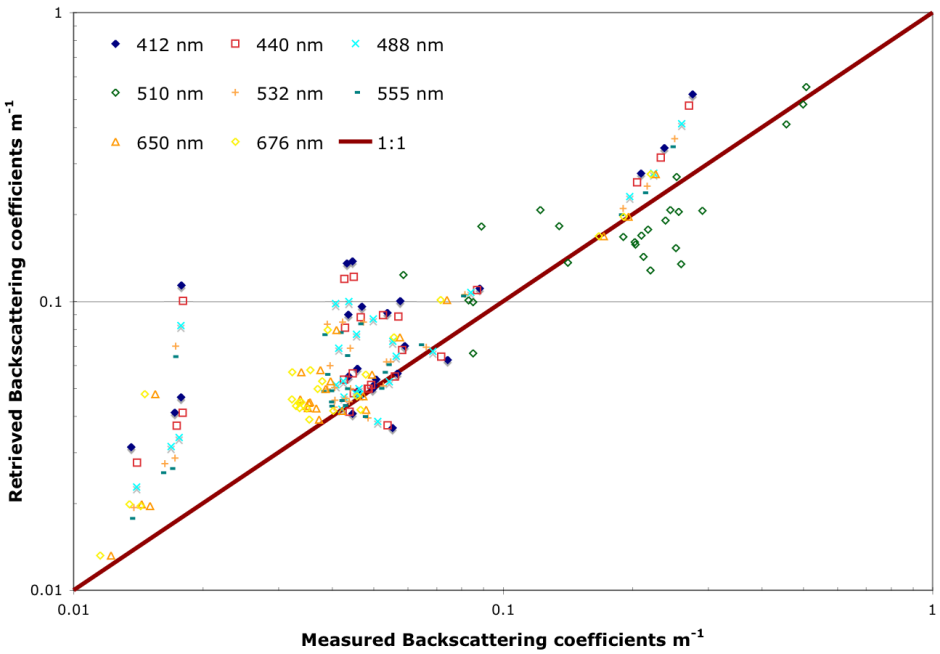

FIGURE 5.9: Retrieved backscattering versus measured backscattering coefficients, using SWIM

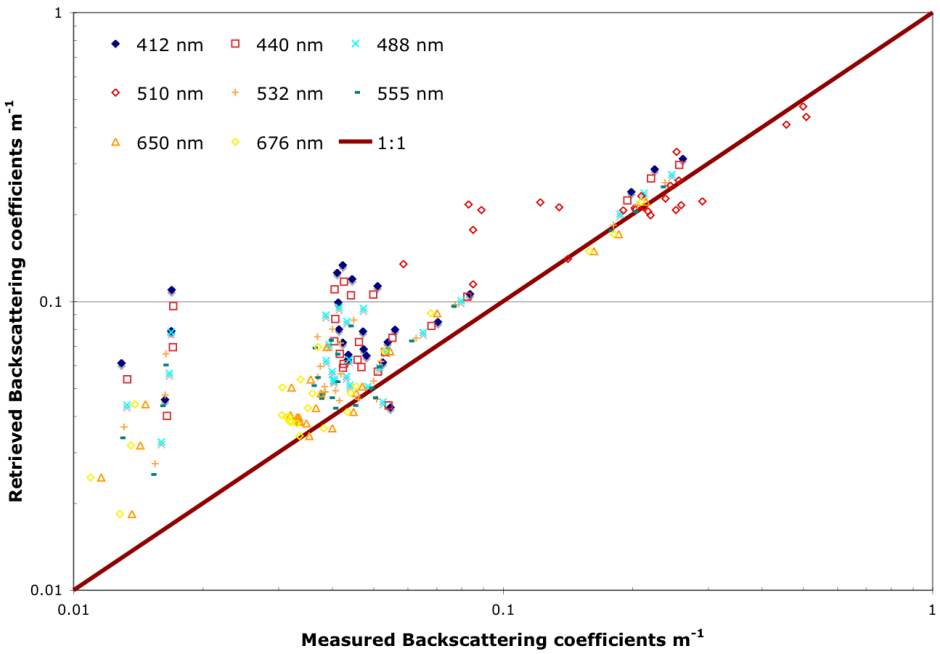

FIGURE 5.10: Retrieved backscattering versus measured backscattering coefficients, using MIM

From Figures **??** and Figure 5.10, it is seen that there are points located near the 1:1 line. However, there are points that are far from the 1:1 line. The RMSE as shown in Table 5.4 at the shorter wavelengths suggest that the backscattering coefficients were not well modeled at these wavelengths. Moreover it was found that the retrieved backscattering coefficients are higher than the measured coefficients estimated from total scattering coefficients. Taking this into account, the errors in the estimated backscattering coefficients would be high to begin with. Nevertheless the low errors from the absorption coefficients gave confidence in the retrieval method. Moreover the test on simulated dataset suggests that the algorithm is able to retrieve accurate backscattering coefficients from remote sensing reflectance.

TABLE 5.4: RMSE of backscattering coefficients from SWIM and MIM

Wavelength (nm)	RMSE (SWIM)	RMSE (MIM)
412	0.359	0.294
440	0.321	0.260
488	0.271	0.216
510	0.250	0.198
532	0.234	0.186
555	0.216	0.171
650	0.169	0.138
676	0.165	0.138

The various retrieved values of $a_g(\lambda)$, $a_{phi}(\lambda)$, S and Y are also tabulated in Table 5.5 to Table 5.8

TABLE 5.5: Retrieved $a_g(\lambda)$, $a_{phi}(\lambda)$, S, $b_{bp}(555)$ and Y from P.Semakau and Cyreene Reefs, using SWIM

S/N	Measured $a_g(440)$ m^{-1}	Derived $a_g(440)$ m^{-1}	Measured $a_\phi(440)$ m^{-1}	Derived $a_\phi(440)$ m^{-1}	Measured S nm^{-1}	Derived S nm^{-1}	Measured $b_{bp}(555)$ m^{-1}	Derived $b_{bp}(555)$ m^{-1}	Measured Y	Derived Y
M1A	1.148	1.048	0.039	0.250	0.0126	0.0120	0.246	0.250	0.450	2.00
M1B	1.128	0.967	0.036	0.180	0.0126	0.0119	0.213	0.180	0.435	2.00
M1C	1.046	0.911	0.036	0.168	0.0128	0.0118	0.187	0.168	0.450	2.00
S1A	0.708	0.567	0.023	0.105	0.0134	0.0117	0.080	0.105	0.408	1.040
S1B	0.575	0.548	0.037	0.052	0.0154	0.0126	0.039	0.052	0.590	1.630
S1C	0.594	0.515	0.023	0.061	0.0138	0.0116	0.054	0.061	0.410	1.250
S2A	0.583	0.495	0.037	0.050	0.0160	0.0124	0.038	0.050	0.580	1.310
S2B	0.574	0.481	0.029	0.051	0.0153	0.0138	0.043	0.051	0.570	1.130
S2C	0.554	0.451	0.032	0.044	0.0156	0.0129	0.040	0.044	0.603	0.975
S2D	0.550	0.463	0.033	0.045	0.0155	0.0128	0.042	0.045	0.682	1.135
S2E	0.585	0.442	0.032	0.041	0.0151	0.0141	0.047	0.041	0.610	0.770
S2F	0.616	0.410	0.070	0.042	0.0144	0.0136	0.040	0.042	0.523	0.535
S2G	0.609	0.439	0.059	0.071	0.0145	0.0122	0.064	0.071	0.560	0.415
S2H	0.655	0.458	0.028	0.046	0.0143	0.0113	0.052	0.046	0.420	0.575
S3A	0.678	0.327	0.042	0.037	0.0160	0.0104	0.043	0.037	0.685	0.375
S3B	0.691	0.991	0.047	0.093	0.0158	0.0137	0.046	0.093	0.615	1.86

TABLE 5.6: Retrieved $a_g(\lambda)$, $a_{phi}(\lambda)$, S, $b_{bp}(555)$ and Y from P.Semakau and Cyreene Reefs, using MIM

S/N	Measured $a_g(440)$ m^{-1}	Derived $a_g(440)$ m^{-1}	Measured $a_\phi(440)$ m^{-1}	Derived $a_\phi(440)$ m^{-1}	Measured S nm^{-1}	Derived S nm^{-1}	Measured $b_{bp}(555)$ m^{-1}	Derived $b_{bp}(555)$ m^{-1}	Measured Y	Derived Y
M1A	1.148	1.048	0.039	0.250	0.0126	0.0120	0.246	0.250	0.450	2.00
M1B	1.128	0.967	0.036	0.180	0.0126	0.0119	0.213	0.180	0.440	2.00
M1C	1.046	0.911	0.036	0.168	0.0128	0.0118	0.187	0.168	0.450	2.00
S1A	0.708	0.567	0.023	0.105	0.0134	0.0117	0.080	0.105	0.410	1.04
S1B	0.575	0.548	0.037	0.052	0.0154	0.0126	0.039	0.052	0.589	1.63
S1C	0.594	0.515	0.023	0.061	0.0138	0.0116	0.054	0.061	0.410	1.25
S2A	0.583	0.495	0.037	0.050	0.0160	0.0124	0.038	0.050	0.580	1.31
S2B	0.574	0.481	0.029	0.051	0.0153	0.0138	0.043	0.051	0.570	1.13
S2C	0.554	0.451	0.032	0.044	0.0156	0.0129	0.040	0.044	0.603	0.980
S2D	0.550	0.463	0.033	0.045	0.0155	0.0128	0.042	0.045	0.682	1.14
S2E	0.585	0.442	0.032	0.041	0.0151	0.0141	0.047	0.041	0.610	0.770
S2F	0.616	0.410	0.070	0.042	0.0144	0.0136	0.040	0.042	0.530	0.540
S2G	0.609	0.439	0.059	0.071	0.0145	0.0122	0.064	0.071	0.555	0.420
S2H	0.655	0.458	0.028	0.046	0.0143	0.0113	0.052	0.046	0.420	0.575
S3A	0.678	0.327	0.042	0.037	0.0160	0.0104	0.043	0.037	0.690	0.375
S3B	0.691	0.991	0.047	0.093	0.0158	0.0137	0.046	0.093	0.620	1.86

TABLE 5.7: Retrieved $a_g(\lambda)$, $a_{phi}(\lambda)$, S, $b_{bp}(555)$ and Y from P.Hantu, using SWIM

S/N	Measured $a_g(440)$ m^{-1}	Derived $a_g(440)$ m^{-1}	Measured $a_\phi(440)$ m^{-1}	Derived $a_\phi(440)$ m^{-1}	Measured S nm^{-1}	Derived S nm^{-1}	Measured $b_{bp}(555)$ m^{-1}	Derived $b_{bp}(555)$ m^{-1}	Measured Y	Derived Y
H1A	0.185	0.229	0.058	0.024	0.0167	0.0116	0.016	0.024	0.4437	1.820
H1B	0.207	0.355	0.049	0.059	0.0158	0.0116	0.017	0.059	0.3572	1.815
H1C	0.272	0.300	0.063	0.066	0.0157	0.0100	0.038	0.066	0.5597	1.435
H1D	0.198	0.112	0.047	0.026	0.0166	0.0100	0.017	0.026	0.4013	2.000
H1E	0.200	0.047	0.051	0.017	0.0167	0.0100	0.014	0.017	0.3112	2.000
H2C	0.344	0.218	0.023	0.053	0.0140	0.0100	0.053	0.053	0.4240	2.000
H2D	0.156	0.207	0.090	0.070	0.0272	0.0100	0.042	0.070	0.4297	1.870
H3A	0.438	0.390	0.051	0.061	0.0140	0.0118	0.043	0.061	0.4153	1.500
H3B	0.359	0.408	0.018	0.053	0.0151	0.0110	0.039	0.053	0.5629	1.950

TABLE 5.8: Retrieved $a_g(\lambda)$, $a_{phi}(\lambda)$, S, $b_{bp}(555)$ and Y from P.Hantu, using MIM

S/N	Measured $a_g(440)$ m^{-1}	Derived $a_g(440)$ m^{-1}	Measured $a_\phi(440)$ m^{-1}	Derived $a_\phi(440)$ m^{-1}	Measured S nm^{-1}	Derived S nm^{-1}	Measured $b_{bp}(555)$ m^{-1}	Derived $b_{bp}(555)$ m^{-1}	Measured Y	Derived Y
H1A	0.185	0.232	0.058	0.025	0.0167	0.0112	0.016	0.025	0.4437	1.915
H1B	0.207	0.378	0.049	0.061	0.0158	0.0122	0.017	0.061	0.3572	1.995
H1C	0.272	0.388	0.063	0.070	0.0157	0.0114	0.038	0.070	0.5597	1.970
H1D	0.198	0.224	0.047	0.035	0.0166	0.0100	0.017	0.035	0.4013	2.000
H1E	0.200	0.121	0.051	0.022	0.0167	0.0100	0.014	0.022	0.3112	2.000
H2C	0.344	0.250	0.023	0.056	0.0140	0.0100	0.053	0.056	0.4240	2.000
H2D	0.156	0.165	0.090	0.064	0.0272	0.0100	0.042	0.064	0.4297	2.000
H3A	0.438	0.393	0.051	0.061	0.0140	0.0117	0.043	0.061	0.4153	1.540
H3B	0.359	0.409	0.018	0.054	0.0151	0.0108	0.039	0.054	0.5629	2.000

From the tables that show the values of S and Y retrieved along with the parameters of $a_g(\lambda)$, $a_{phi}(\lambda)$, S and $b_{bp}(555)$, it can be seen that the value of Y is not well retrieved at times. This could explain for the spread of backscattering coefficients as seen in the previous scatterplots.

Next, we look at the retrieved IOPs and modeled $R_{rs}(\lambda)$ for deep and shallow waters. The retrieved IOPs are shown in Figure 5.11 and Figure 5.13 .

As seen from the retrieved IOPs over the deep waters, both the SWIM and MIM are able to derive the absorption and backscattering coefficients from the measured reflectance. At the shorter wavelength of 412 nm, a deviation can be observed and this could be attributed to the spectral slope S not accurately modeled. The backscattering coefficients, from both methods are higher than the estimated coefficients from total scattering. For the shallow waters, it can be seen that the absorption coefficients retrieved by the SWIM approach agree well with the measured while that from the MIM did not do as well. The backscattering coefficients retrieved over the shallow waters, suggests that the SWIM approach did modestly better than the other one. The measured and modeled reflectance can be seen in Figure 5.13.

The error in log space was also investigated to evaluate how well the algorithm retrieved IOPs over shallow waters. The error in log space is,

$$|log_{10}(IOP^{retrieved}(\lambda)) - log_{10}(IOP^{measured}(\lambda))| \tag{5.18}$$

As it can be seen from Figure 5.14 to Figure 5.16, the errors for the three wavelengths examined, which are namely 440, 480 and 550 nm indicates that the SWIM has done better at depths less than 3 meters. From the plots, it can also be seen that the errors in backscattering coefficients are more sensitive to shallow waters. This could be due to extra contribution from the bottom

reflectance of the sea bed. It can be seen that for depths greater than 5 meters, the MIM outperforms the SWIM approach by a small margin. The extra bands provided extra information in the matrix inversion process which could explain the lower errors for the MIM. From the results it seems that only waters with depths of 3 meter or less are considered optically shallow.

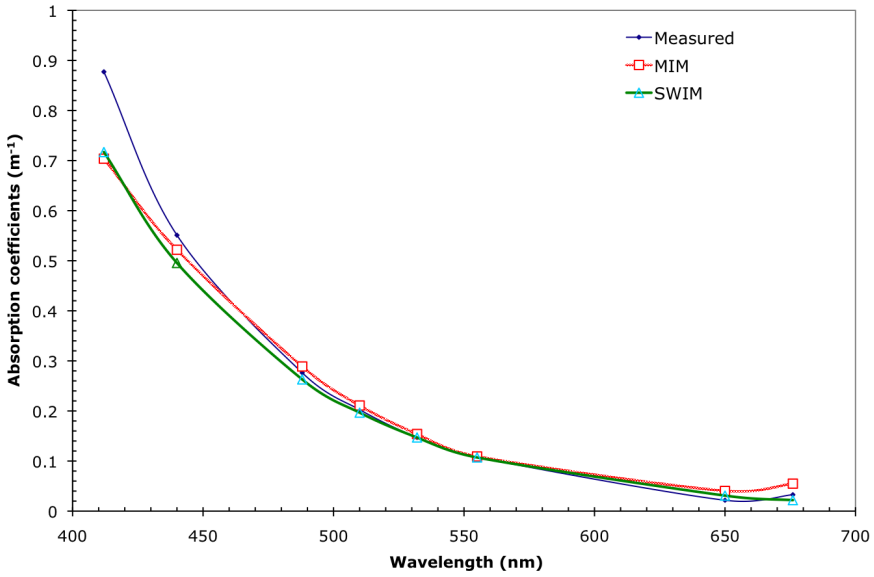

(a) Retrieved absorption coefficients

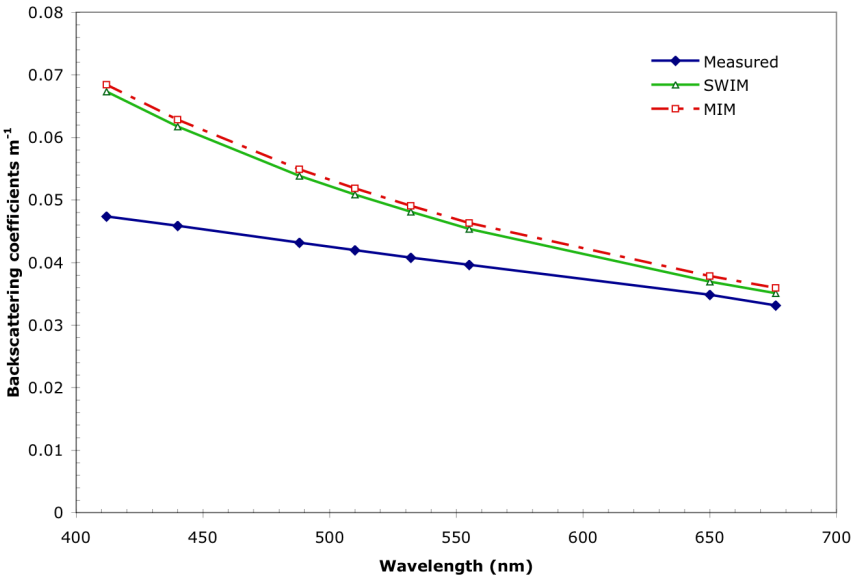

(b) Retrieved backscattering coefficients

FIGURE 5.11: Retrieved IOPs for deep water, depth of 10 meters

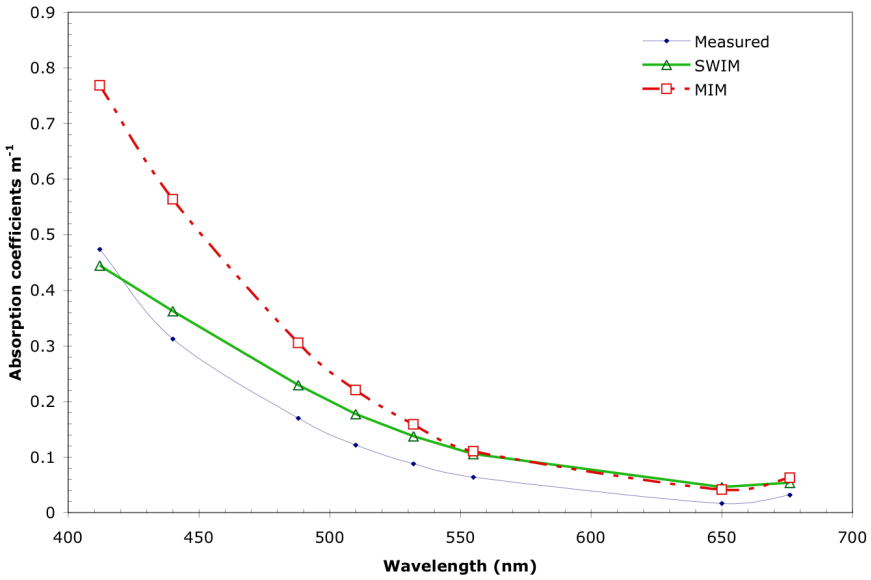

(a) Retrieved absorption coefficients

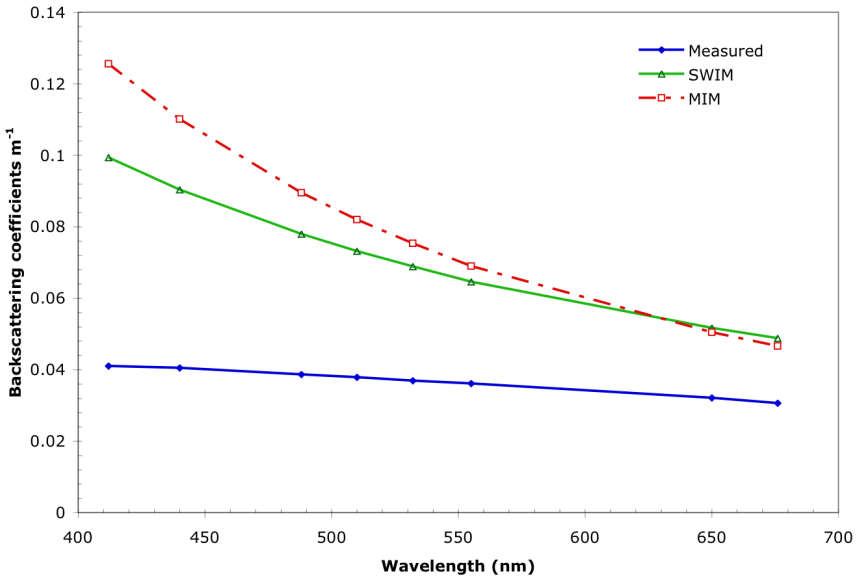

(b) Retrieved backscattering coefficients

FIGURE 5.12: Retrieved IOPs for shallow water, depth of 1 meters

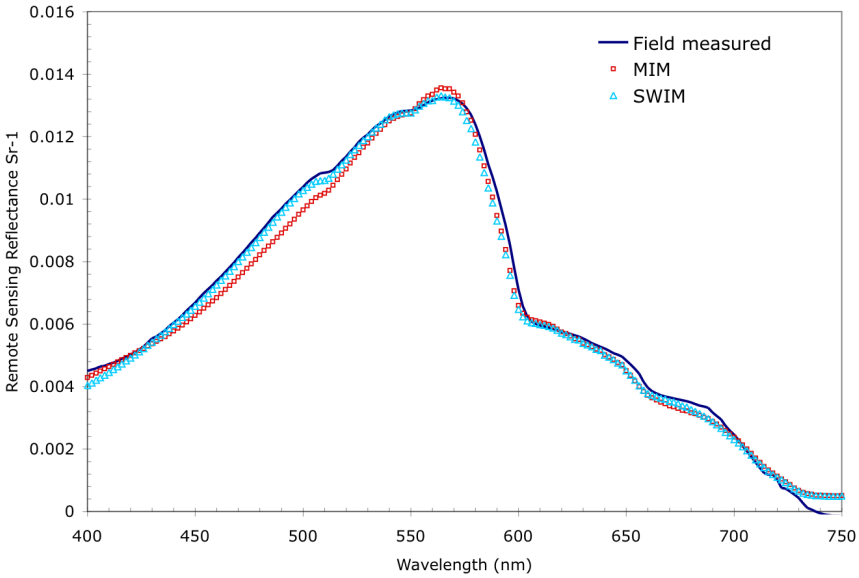

(a) Measured and modeled $R_{rs}(\lambda)$ over deep waters

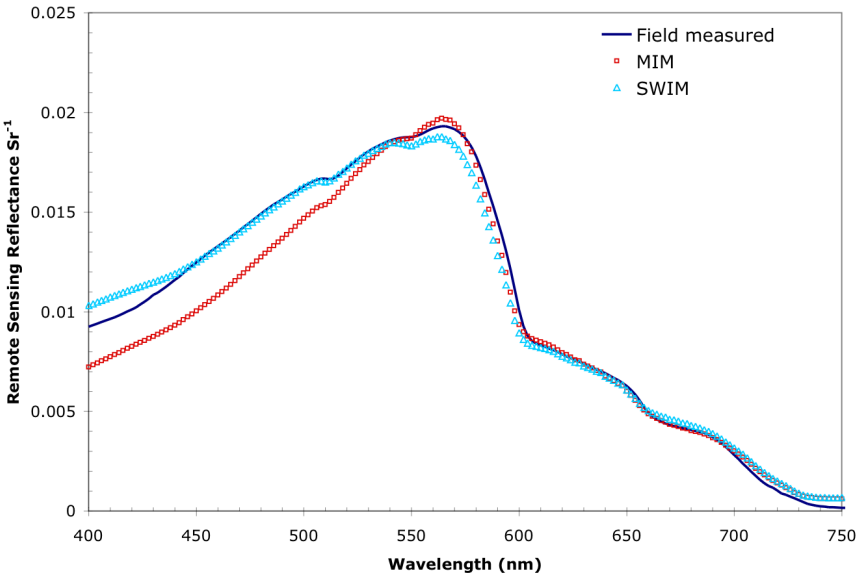

(b) Measured and modeled $R_{rs}(\lambda)$ over shallow waters

FIGURE 5.13: [Measured and modeled $R_{rs}(\lambda)$

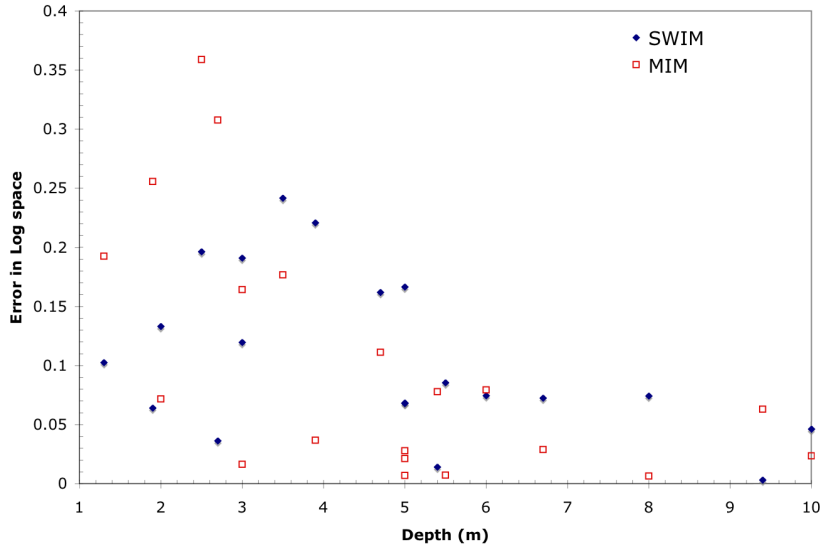

(a) Absorption coefficients errors vs depth

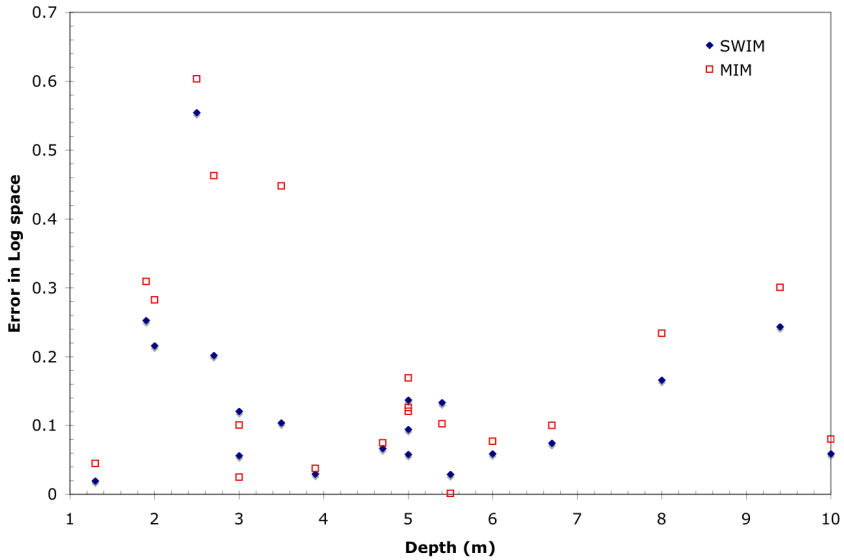

(b) Backscattering coefficients vs depth

FIGURE 5.14: IOPs errors vs depth (440 nm)

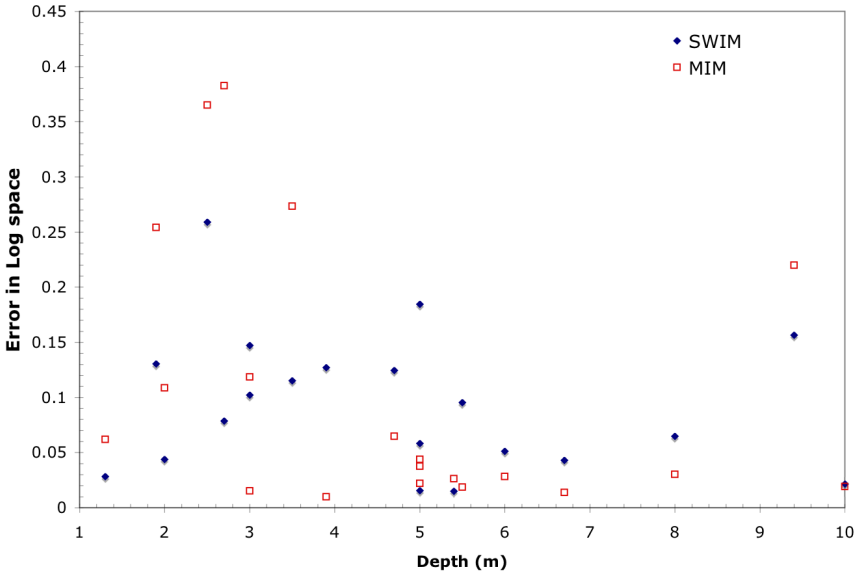

(a) Absorption coefficients errors vs depth

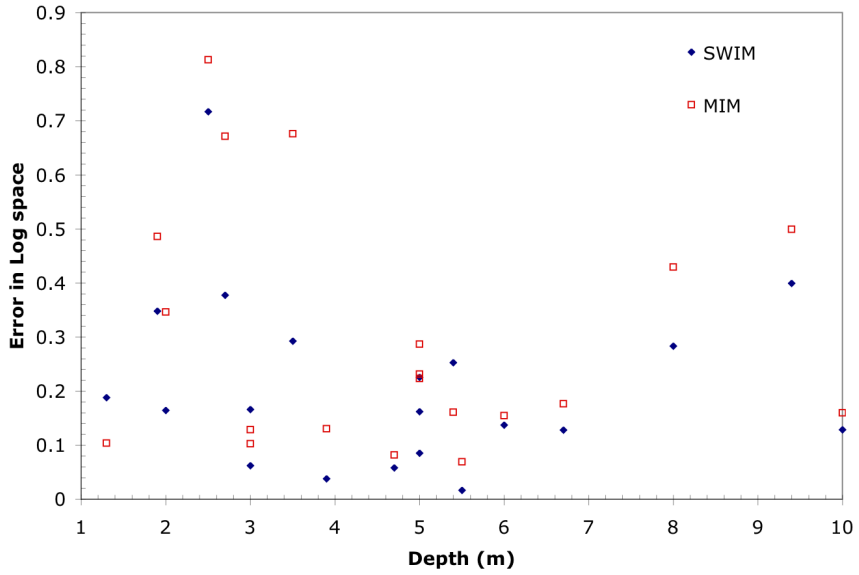

(b) Backscattering coefficients vs depth

FIGURE 5.15: Plot of IOPs errors vs depth (488 nm)

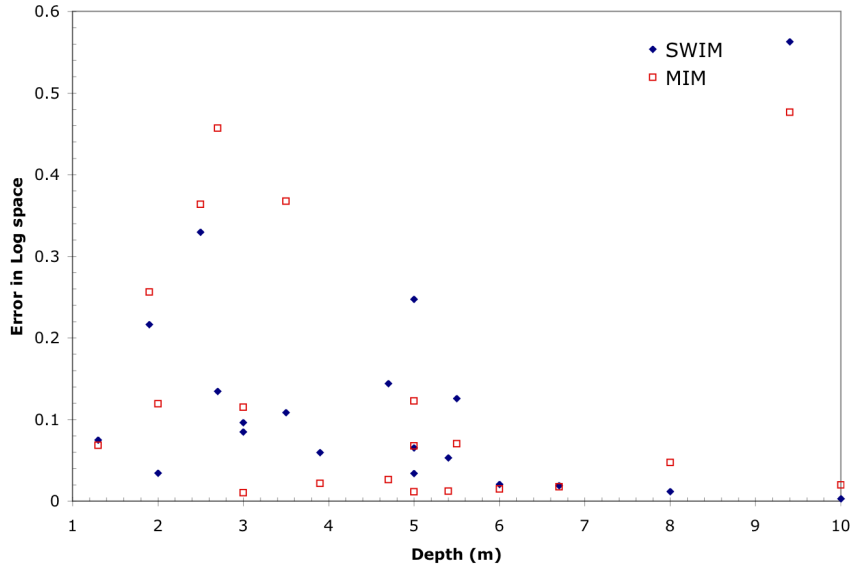

(a) Absorption coefficients errors vs depth

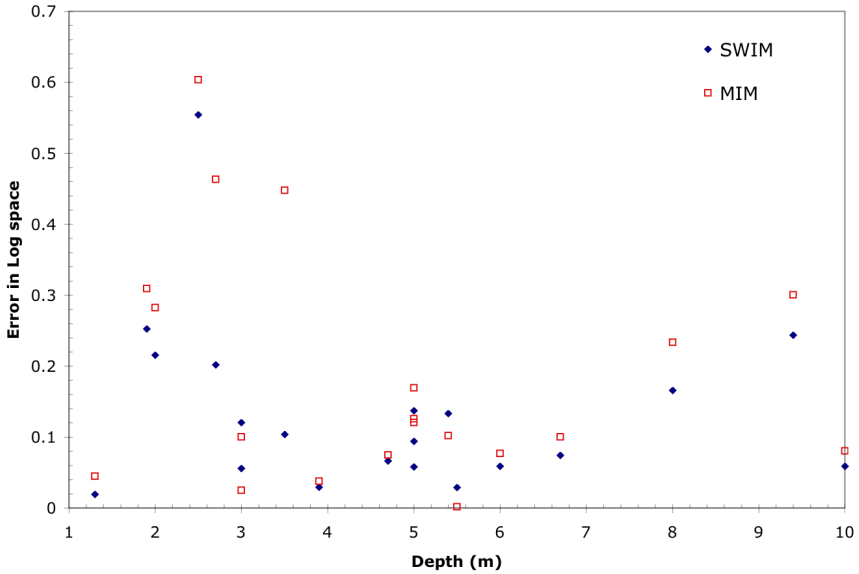

(b) Backscattering coefficients vs depth

FIGURE 5.16: IOPs errors vs depth (550 nm)

5.5.3 Algorithm Performance over shallow waters

The algorithm utilizes spectral windows with the least light penetration. In order to examine how valid and useful this approach is, two different types of data, field data and simulated data were used. For the simulated data, IOPs of lowest absorption that were measured around the area of interest were used as inputs. The depth with values of sand reflectance were varied. The depth ranged from 1 to 8 meters, while the values of 0.10 and 0.30 were used for the bottom reflectance. The absorption at 440 nm is about 0.35 m^{-1} and total scattering 1 m^{-1}, these IOPs was from the measurements made at point H1A. The spectrums generated for the test can be seen in Figure 5.17 .

The SWIM algorithm was implemented on the HYDROLIGHT simulated data. The MIM used in this section refers to using the spectral windows from 460 mn to 590 nm for the matrix inversion. In short, the MIM includes the green region of spectrum where light penetration is the greatest. The errors in log space shown in Eq.(5.18) were plotted against $\psi(\lambda, H)$ from Eq.(5.15) for the various IOPs retrieved by the two different algorithms. The plots are shown in Figure 5.18 to Figure 5.20 .

From the figures showing the errors in IOPs for spectrums with bottom reflectance of 0.3, the errors of retrieved IOPs from the SWIM method is much lower for absorption and backscattering coefficients. However the errors for the absorption coefficients by the MIM is much lower than the SWIM approach at 440 nm. This is due to the inaccurate modeling of the absorption coefficients and can be seen in Figure 5.21. This can also be deduced from the fact that the errors at other wavelengths are much smaller for the split window approach.

Likewise, it can be seen that the errors incurred by the SWIM method is lower than the MIM approach. The errors at lower values of $\psi(\lambda, H)$ for both methods converges as expected for the spectrums generated with bottom reflectance of 0.1. The test on the simulated dataset suggests that the SWIM approach was able to retrieve IOPs with lower errors as compared to the MIM approach for shallow waters.

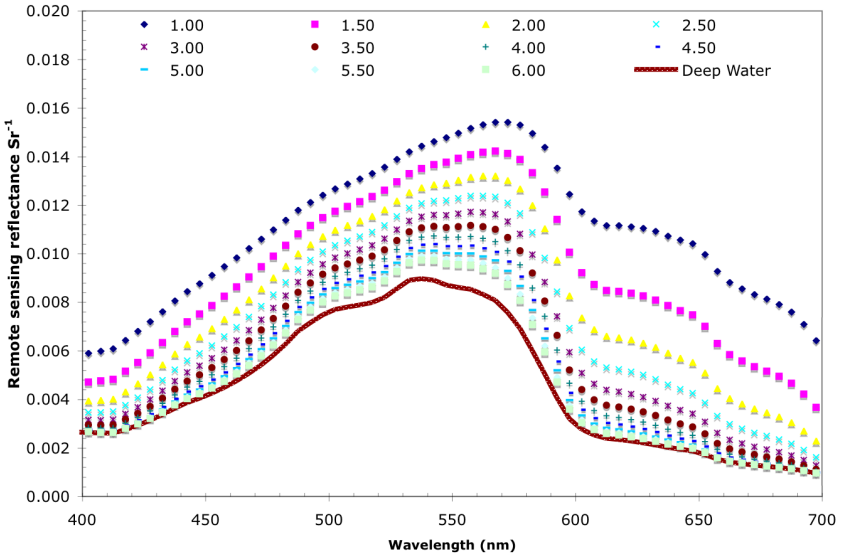

(a) $R_{rs}(\lambda)$ generated with bottom reflectance 0.1

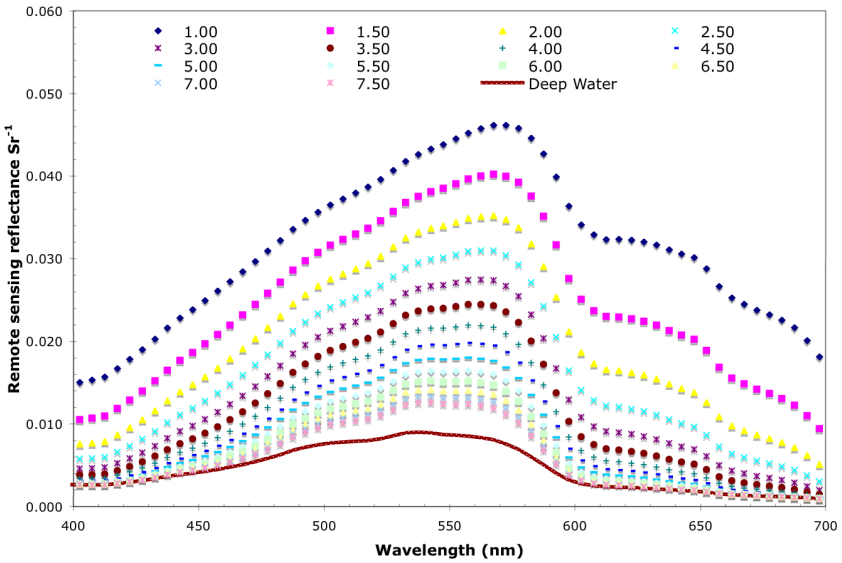

(b) $R_{rs}(\lambda)$ generated with bottom reflectance 0.3

FIGURE 5.17: Reflectance spectra were generated with different bottom reflectance, depths are shown in figure, ranging from 1 to 7.5 m, in steps of 0.5 m

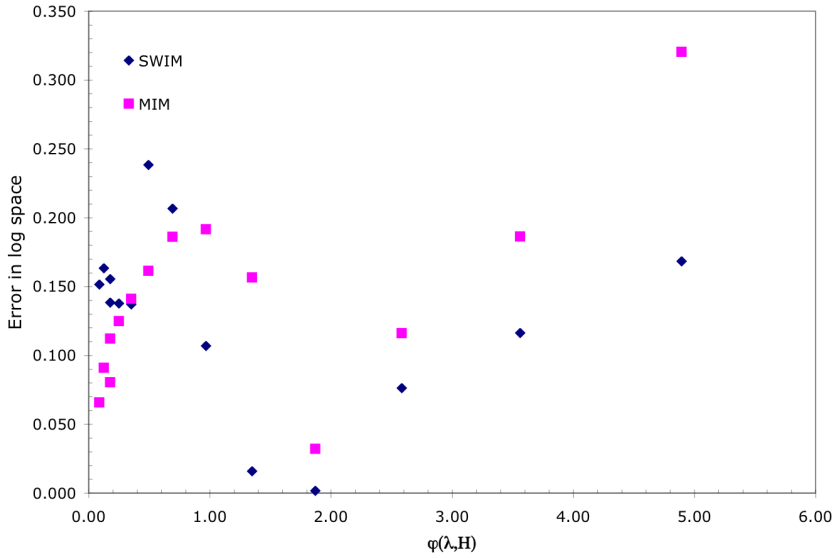

(a) Plot of absorption coefficients errors vs $\psi(\lambda, H)$

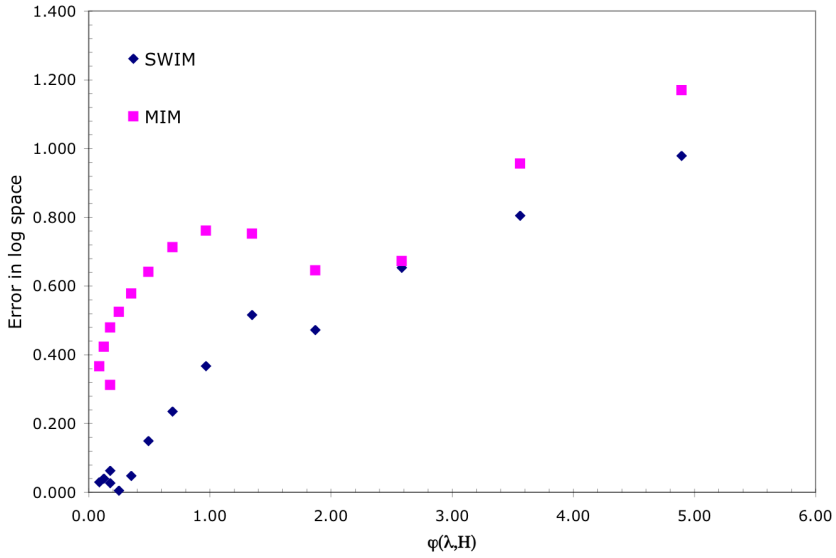

(b) Plot of backscattering coefficients vs $\psi(\lambda, H)$

FIGURE 5.18: Plot of errors vs $\psi(\lambda, H)$ (440 nm) with bottom reflectance of 0.3

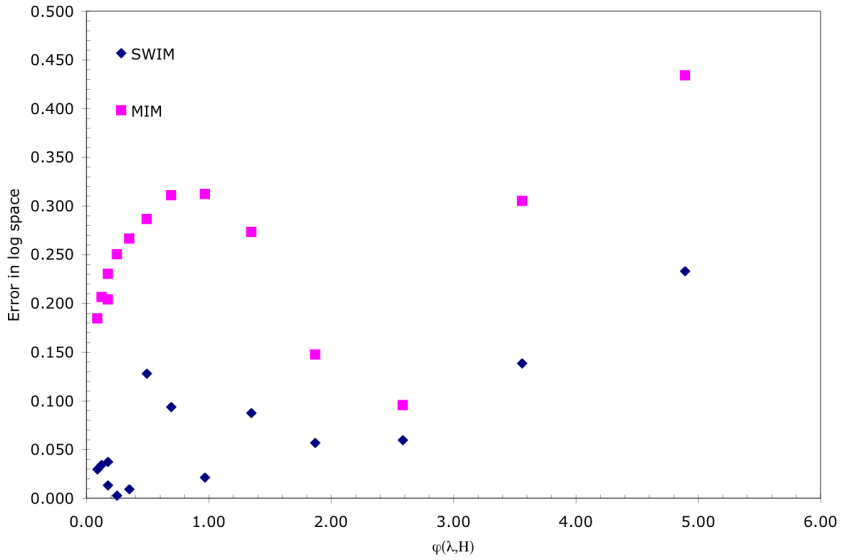

(a) Plot of absorption coefficients errors vs $\psi(\lambda, H)$

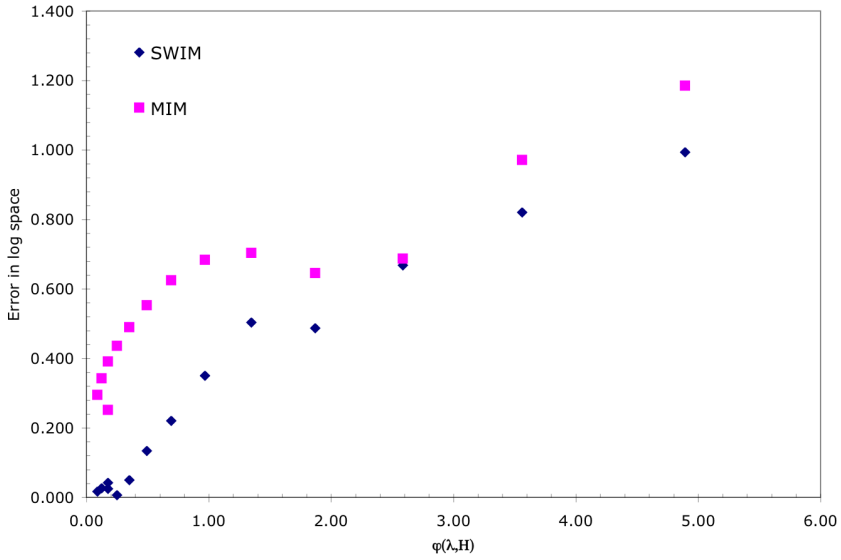

(b) Plot of backscattering coefficients vs depth

FIGURE 5.19: Plot of errors vs $\psi(\lambda, H)$ (480 nm) with bottom reflectance of 0.3

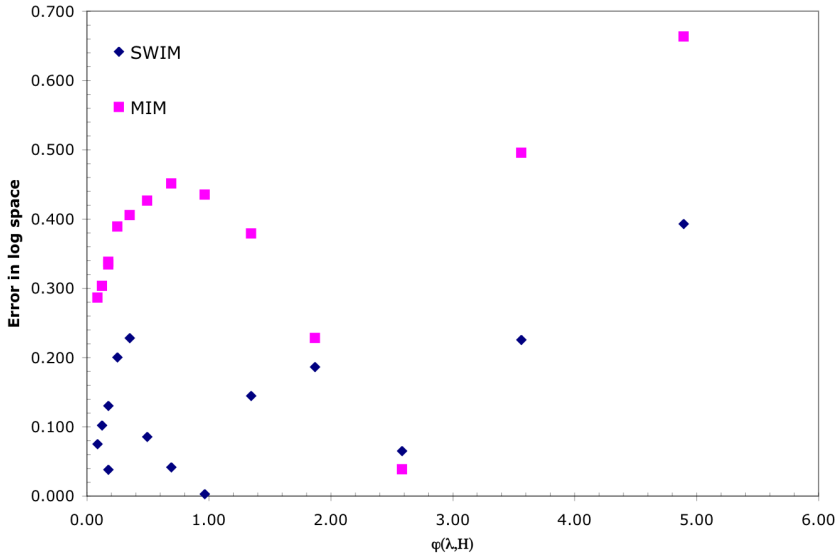

(a) Plot of absorption coefficients errors vs $\psi(\lambda, H)$

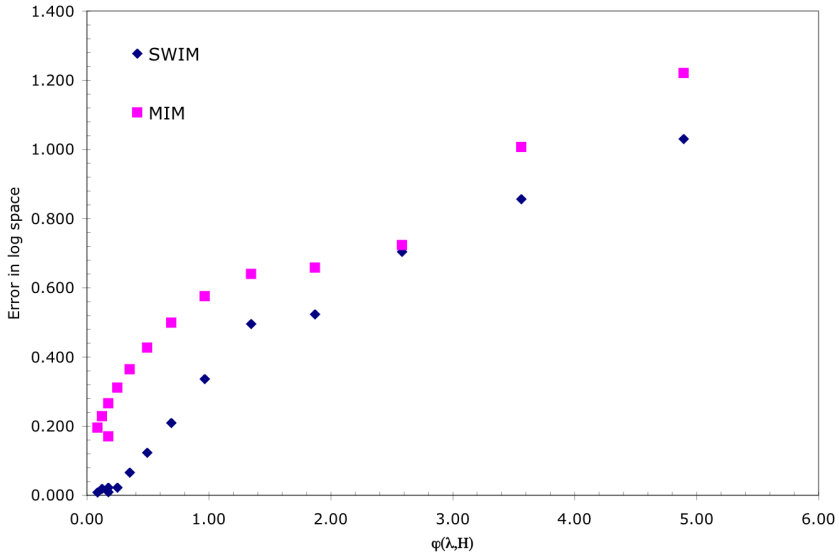

(b) Plot of backscattering coefficients vs depth

FIGURE 5.20: Plot of errors vs $\psi(\lambda, H)$ (550 nm) with bottom reflectance of 0.3

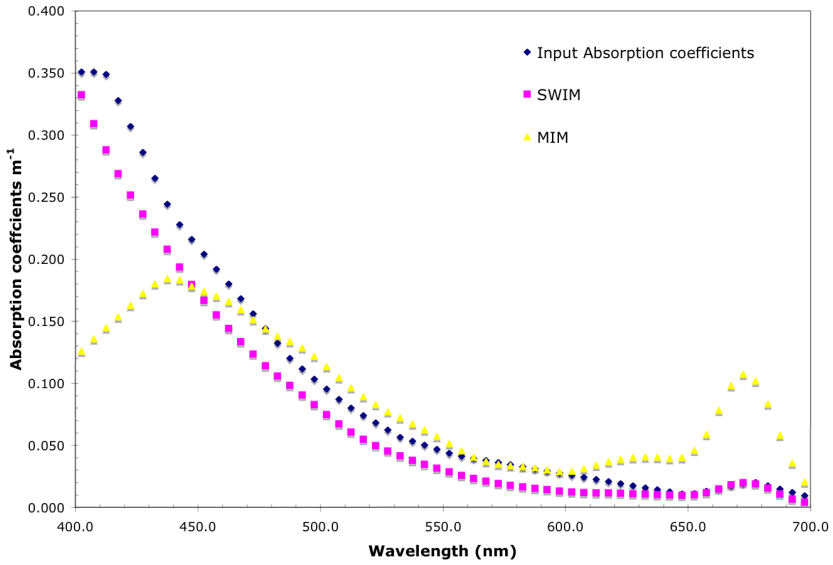

(a) Retrieved absorption coefficients from shallow water reflectance

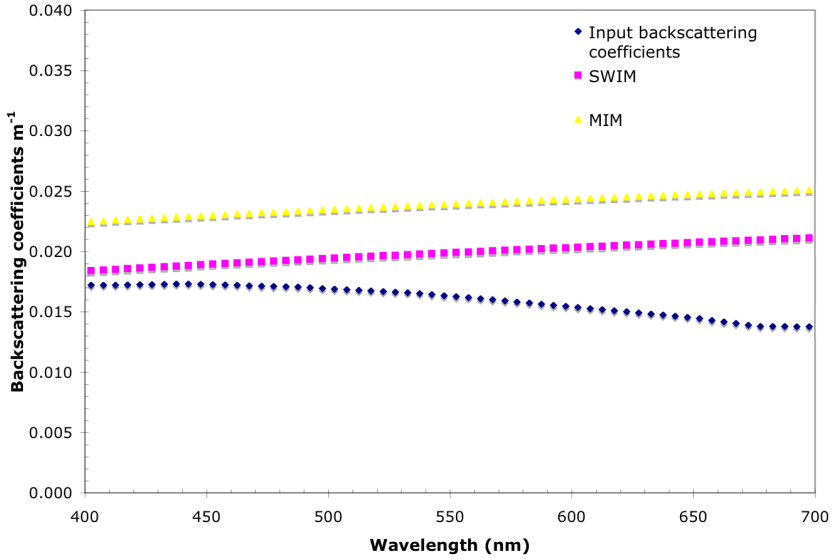

(b) Retrieved backscattering coefficients from shallow water reflectance

FIGURE 5.21: Retrieved IOPs for shallow water, depth = 3 m, bottom reflectance = 0.1, $\psi(440, H)$ =0.3

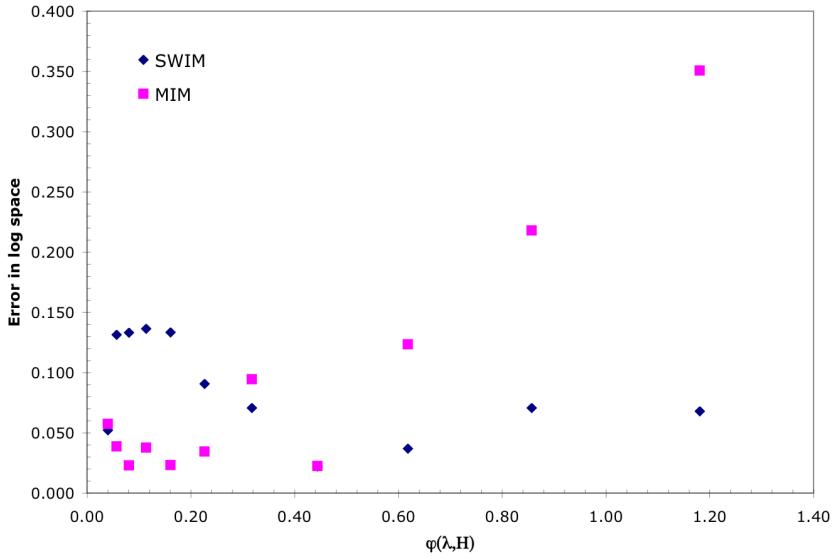

(a) Absorption coefficients errors vs $\psi(\lambda, H)$

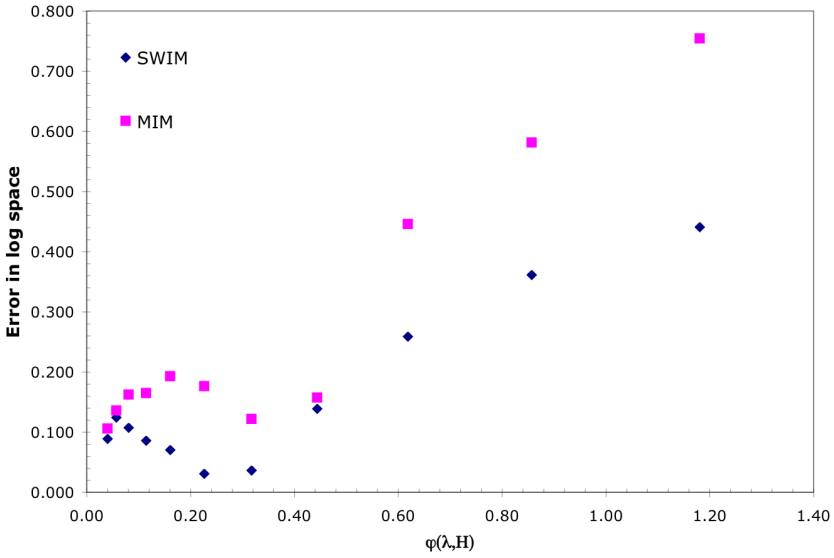

(b) Backscattering coefficients vs $\psi(\lambda, H)$

FIGURE 5.22: IOPs errors vs $\psi(\lambda, H)$ (440 nm) with bottom reflectance of 0.1

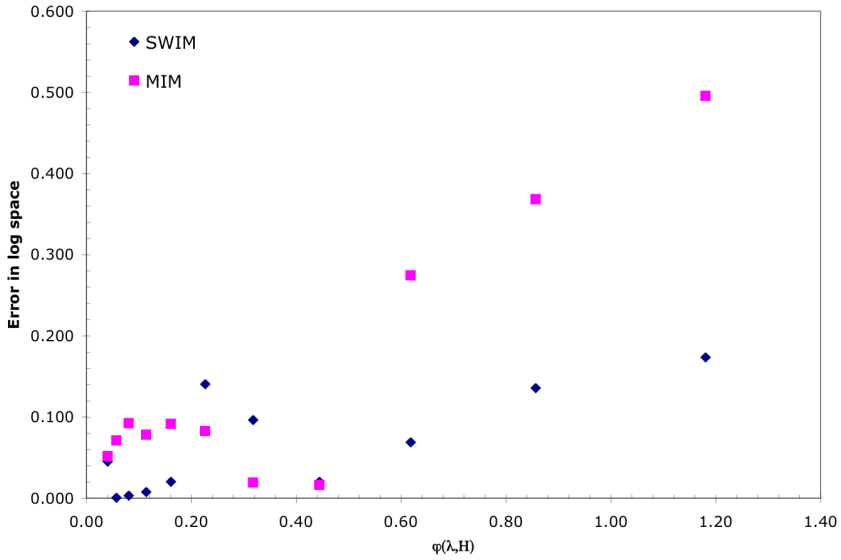

(a) Absorption coefficients errors vs $\psi(\lambda, H)$

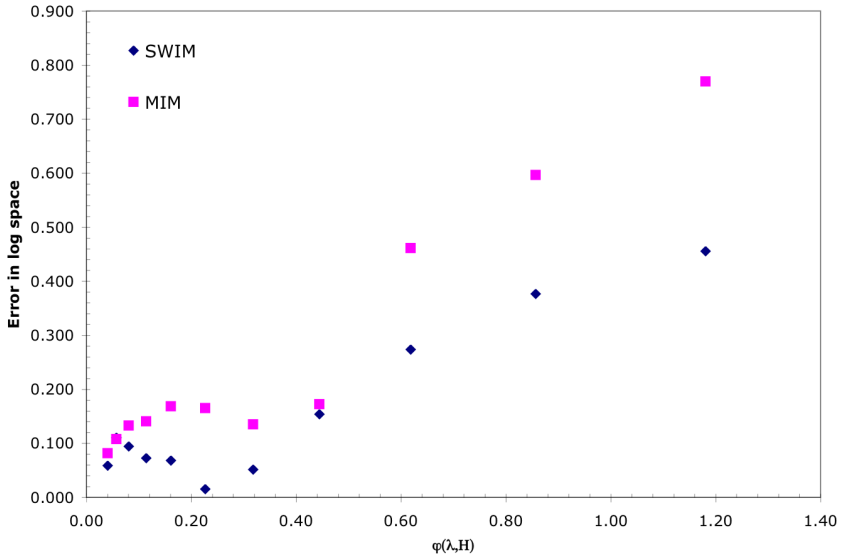

(b) Backscattering coefficients vs $\psi(\lambda, H)$

FIGURE 5.23: IOPs errors vs $\psi(\lambda, H)$ (480 nm) with bottom reflectance of 0.1

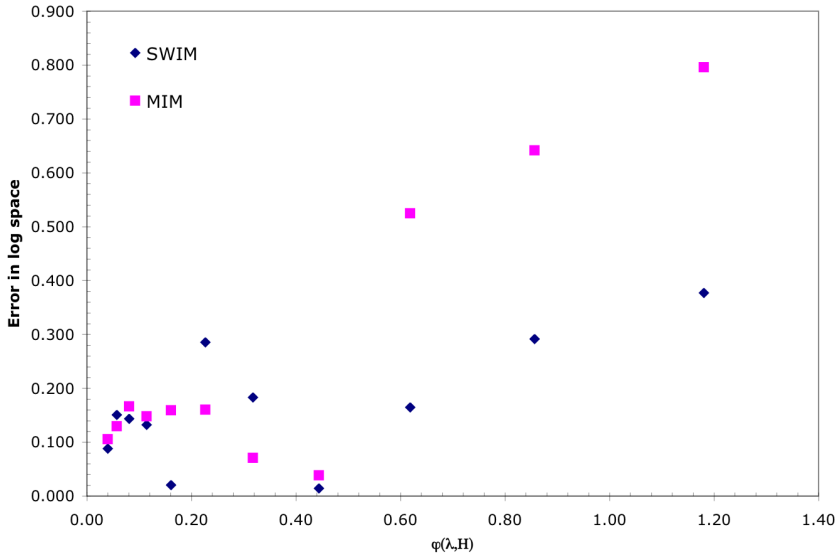

(a) Absorption coefficients errors vs $\psi(\lambda, H)$

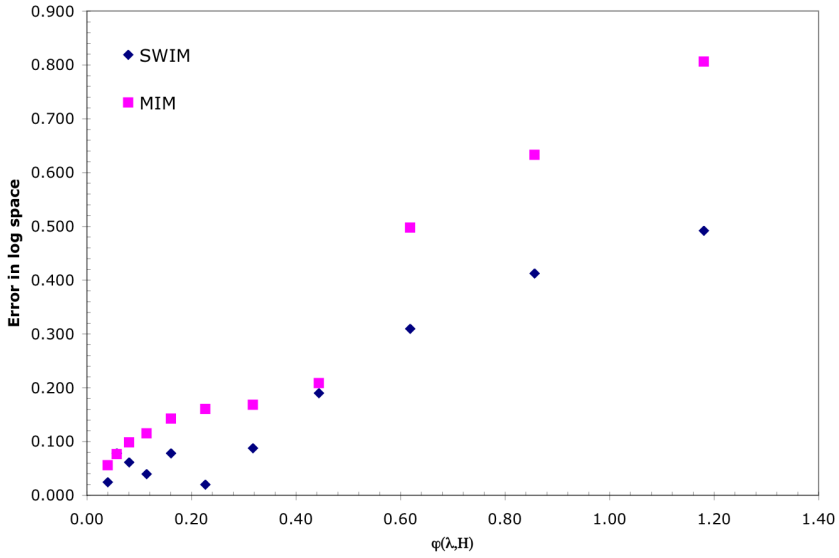

(b) Plot of backscattering coefficients vs $\psi(\lambda, H)$

FIGURE 5.24: IOPs errors vs $\psi(\lambda, H)$ (550 nm) with bottom reflectance of 0.1

5.5.4 Hyperspectral data

The algorithm was implemented on atmospherically corrected data from the Hyperion sensor, which has a total of 224 bands. However for our purporse of remote sensing of ocean colour, only the first 50 bands in the range of 400 - 900 nm were used. The width of each Hyperion band is approximately 10 nm. The hyperspectral data was corrected with the cloud and shadow atmospheric correction scheme which was explained in the previous chapter. Region of Interests (ROIs) were chosen for testing the SWIM algorithm. The original image has a spatial resolution of 30 m per pixel, the pixels were aggregated from two into one. This was to improve the SNR and to lower the noise in the corrected water reflectance.

The imagery was collected on 2 June 2001 at 03:41 UTC. There were no concurrent measurements of optical properties such as absorption and backscattering coefficients. Hence there is a need to provide validation for the retrieved IOPs. In this study, the well known HYDROLIGHT for radiative transfer in water was used to generate water reflectance for validation. The retrieved IOPs were used as inputs to HYDROLIGHT to compute water reflectance.

After applying the SWIM algorithm to HYPERION data, absorption and backscattering coefficients maps were produced at 440 nm and 550 nm, respectively. They are shown in Figure 5.25 . The maps suggest that the algorithm reproduced IOPs map that are able to delineate the different water bodies. This could be seen from the water plume (ROI C) region in the backscattering map which is corresponding found in the RGB image. The dark water body at (ROI B) could also be seen delineated by both absorption and backscattering maps.

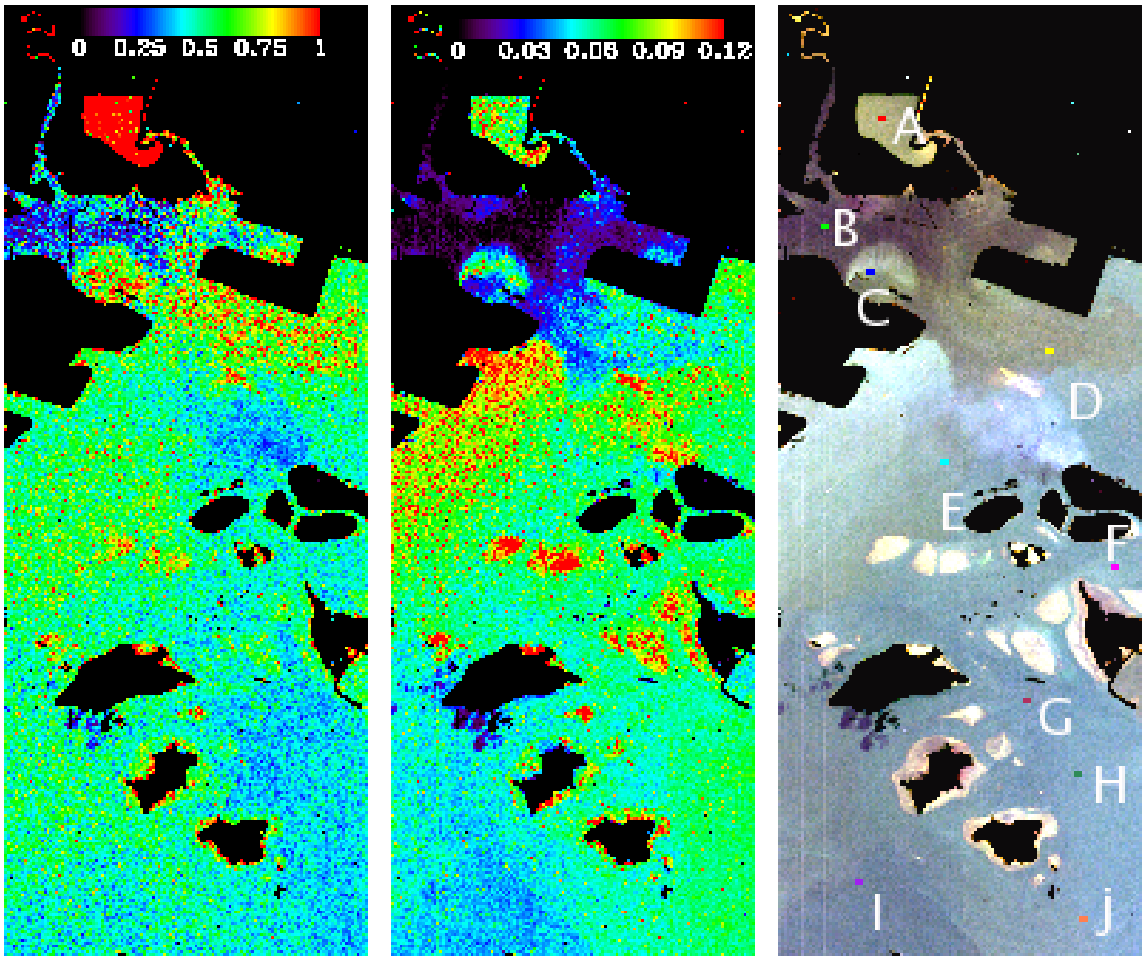

(a) Absorption coefficients Map (b) Backscattering coefficients Map (c) HYPERION Image

FIGURE 5.25: IOPs retrieved from HYPERION

The smoke plume seen in the RGB image Figure 5.25(c) was not removed totally by atmospheric correction and retrieved as higher backscattering in the map. The corals were also seen in the backscattering map. However, this does not suggests that the algorithm has failed to retrieve the IOPs accurately but higher errors could have been incurred due to contribution from the sea bottom. The features in ROI (G,H,J) which looked like suspended sediments in the Hyperion RGB image were also reflected in the backscattering coefficients map. This was sur-

prising as the algorithm was able to retrieve backscattering coefficients that are well resolved to show such features.

The absorption map was also able to delineate certain water bodies such as the reservoir at ROI A and the darker brownish water body at ROI D. The effects of the smoke plume was seen in the backscattering map but not in the absorption map. This suggest that the algorithm is more susceptible to errors in retrieving backscattering coefficients due to increased reflectance.

The retrieved IOPs were used as inputs for the HYDROLIGHT code to make forward simulation of $R_{rs}(\lambda)$. values. Deep waters were assumed and the simulated spectral range was from 400 to 700 nm for Hyperion bands. The forward simulated reflectance was compared to hyperspectral reflectance spectrum corrected by the atmospheric correction scheme implemented in this study. Several region of interests (ROIs) were selected for comparisons as shown in Figure 5.25(c) .

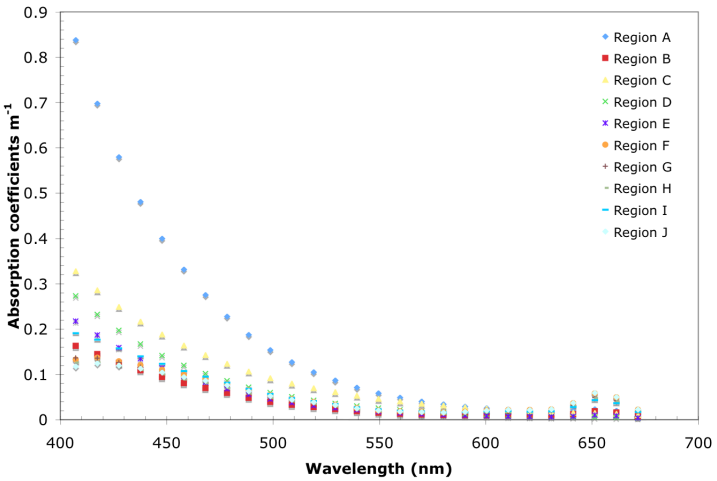

(a) Retrieved Absorption from HYPERION

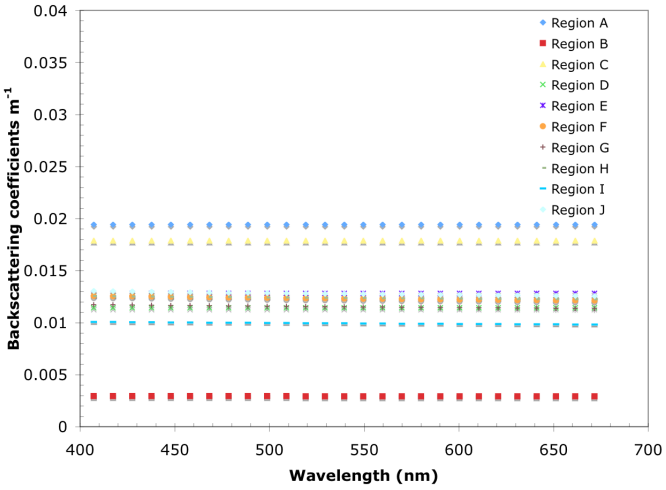

(b) Retrieved Backscattering from HYPERION

FIGURE 5.26: IOPs retrieved from HYPERION

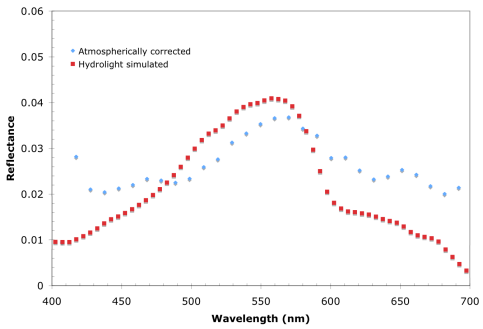

(a) ROI A

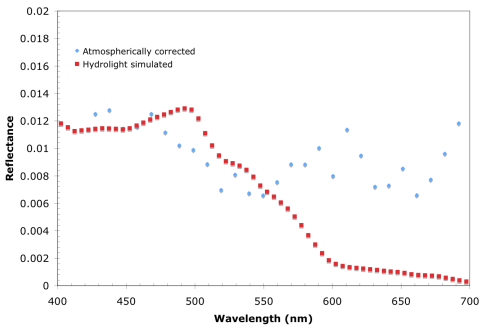

(b) ROI B

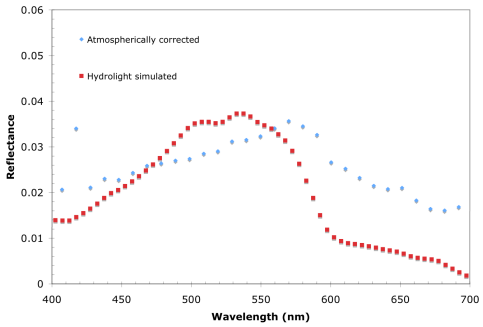

(c) ROI C

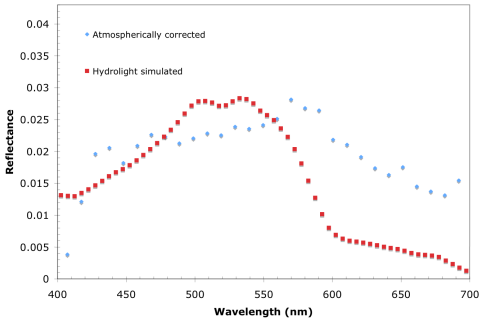

(d) ROI D

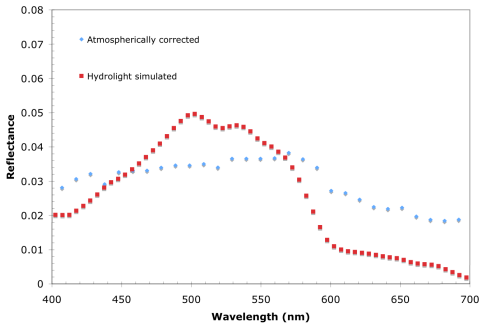

(e) ROI E

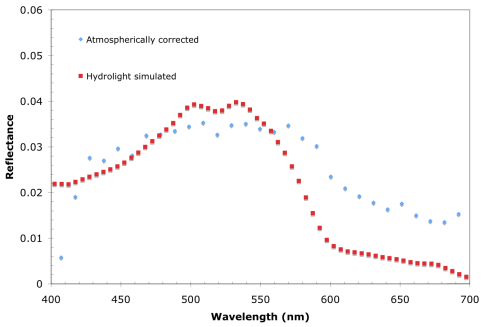

(f) ROI F

FIGURE 5.27: ROI A-F Fitted $R_{rs}(\lambda)$ compared with HYDROLIGHT

From Figure 5.27 , the HYDROLIGHT simulated reflectance coincides well with the corrected reflectance. However it can be seen that the spectrum agrees well between 400 nm to 600 nm. At longer wavelengths, the corrected reflectance is much higher than the simulated. This could be due to under correction by the atmospheric correction scheme. For the ROI C, the reflectance is very low and noisy which can be attributed to the high absorption as seen from the original RGB image in Fig 5.25(c) . The spectrum also has a low reflectance as compared to the spectrum from other ROIs. The reflectance is about 2 times smaller as compared to the least bright spectrum (ROI D). This evidently shows that the corrected reflectance maybe unreliable as it is highly susceptible to noise in the original data and errors in the atmospheric correction scheme.

For ROIs (G-J), they belong to open waters, and the spectral shapes are similar. There is strong agreement with the HYDROLIGHT, atmospherically corrected and computed reflectance in the wavelength range from 400 nm - 580 nm. The RMSE between the atmospherically corrected and HYDROLIGHT reflectance is shown in Figure 5.29.

The RMSE has a low value of 0.15 and a high value of 0.60 for wavelengths longer than 600 nm. This was in line with the observations made for the plots shown in Figure 5.27 and Figure 5.28 where the HYDROLIGHT simulated does not overlap with the atmospherically corrected reflectance. The low errors suggest that the retrieved IOPs were correct and gave further robustness of SWIM.

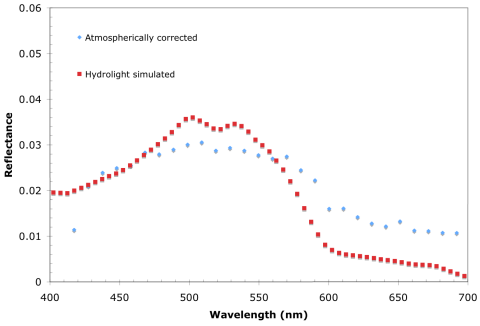

(a) ROI G

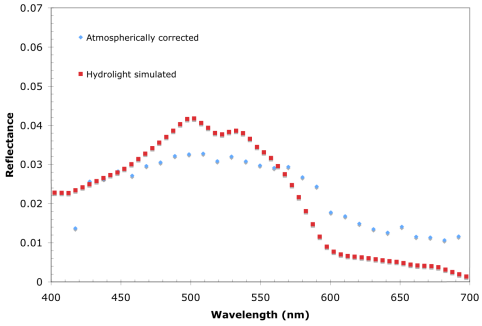

(b) ROI H

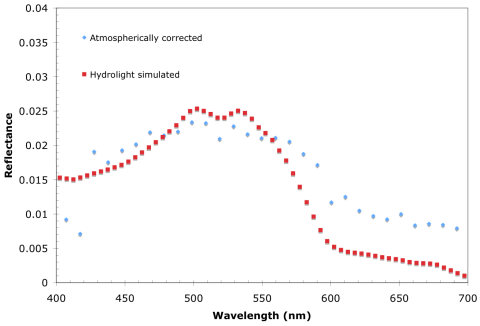

(c) ROI I

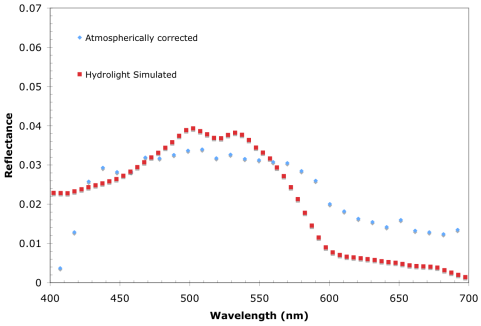

(d) ROI J

FIGURE 5.28: ROI G-J Fitted $R_{rs}(\lambda)$ compared with HYDROLIGHT

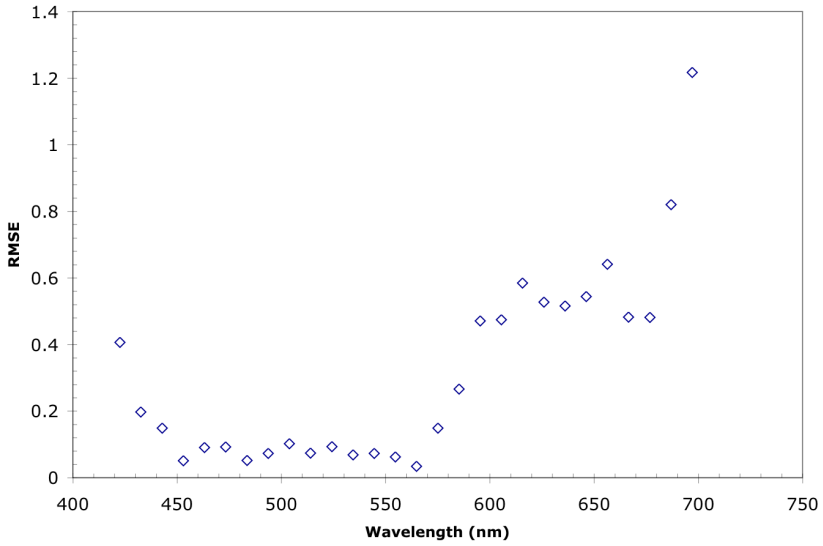

FIGURE 5.29: RMSE computed as a comparision for HYDROLIGHT simluated data and atmospherically corrected reflectance

5.6 Conclusions

An algorithm was developed to retrieve the IOPs for both shallow and deep waters from its reflectance. The test on forward simulated data (IOCCG) showed that it is able to match up to most of the present algorithms used in the ocean colour community although a spectral window was omitted in the retrieval process, the IOPs were retrieved with low errors in the visible spectral range. However the error went up in the red region. This was due to the dominant signature of water absorption. The wide range of absorption and backscattering coefficients used in the generation of the remote sensing reflectance provided a good test of the algorithm. The algorithm has proved to be able to derive the IOPs in the wide range of reflectance tested and implying that the algorithm is able to work well for most types of optically deep water.

The algorithm was also tested on field measured data. The errors are acceptable in view of the low confidence in the measurements. The acceptable errors in the retrieval of IOPs suggest that both the radiometric and in-situ measurements are correct. The selection of spectral windows where light has the least penetration was able to minimize the errors in the retrieval of IOPs as shown from the test on field measured data. This was concluded from the lower errors for absorption and backscattering retrieved for the SWIM method. The SWIM method was also compared to MIM where the green spectral region was included in the matrix inversion implementation. The SWIM approach was able to match up to the MIM and outperformed it in shallow waters region especially for waters with depths of 3.5 m or less.

The two methods were also compared using HYDROLIGHT simulated reflectance where the

depth and sea bottom reflectance was varied to investigate how the contribution from shallow water reflectance would affect the IOPs retrieved. As seen from the results, the backscattering coefficients are sensitive to extra contribution from shallow water reflectance and the SWIM method was able to handle it better. It could be seen in Figure 5.21 that the extra contribution from the bottom reflectance also resulted in deriving high phytoplankton absorption instead of the high CDOM absorption present.

SWIM was also tested on atmospherically corrected hyperspectral data. From the corrected data, the noise in the spectrum could be seen visibly, however the algorithm was still able to retrieve the IOPs. The retrieved IOPs were used as inputs to HYDROLIGHT to generate reflectance spectrums. This was done in place of actual field measurements as the image was acquired back in 2001. The reflectance spectrum from HYDROLIGHT has strong agreement with the corrected spectrums especially in the blue and green regions.

SWIM has been successfully implemented on three different type of datasets. It has been shown to be able to minimize the contribution from the sea bottom for shallow waters. SWIM can be also adapted for othe satellite sensors provided that there are enough spectral bands to perform the implementation.

Chapter 6

Conclusions

The cloud and shadow algorithm was able to perform atmospheric correction on satellite imagery using cloud and shadow image features without assumption on atmospheric optical properties as visible bands. In fact atmospheric optical properties were derived from hyperspectral satellite imagery. An inversion algorithm termed as Split-window inversion method, SWIM was designed for both shallow and deep turbid waters. The algorithm uses spectral windows where light was assumed to be least peneratable. It was tested on simulated, experimental and satellite datasets.

The atmospheric correction scheme was implemented on the satellite Imagery from the Ikonos and Hyperion satellite. The main aim was to derive the atmospheric properties of the aerosol, which also means to perform accurate atmospheric correction. The algorithm was designed to require little ancillary inputs such as aerosol model, optical thickness and calibration constants for the raw counts to radiance. The calibration constant at NIR is needed for this method and also a value of $\alpha(NIR)$ is needed. It was shown and found that the values of $\alpha(NIR)$ had little

influence on the path radiance and the derived water reflectance. The corrected water reflectance from the Ikonos image was compared to near concurrent field measurements. It was found that the error in the visible spectral band is about 20.0 %. This indicates the correct implementation of the algorithm.

The scheme was then applied to Hyperion imagery. The corrected water reflectance was compared to that corrected from TAFKAA. Regression of the two reflectance data sets with a total of 100,000 points suggest that the TAFKAA corrected reflectance is similar to that corrected with the cloud and shadow method. It was observed, for longer wavelengths of 700 nm and beyond, the sharp absorption features centered at 720, 760 and 830 nm were corrected. This does not imply that TAFKAA is unable to handle the correction but the lack of spectral bands beyond 900 nm was the reason why TAFKAA was not used to correct gaseous absorption.

The results from Ikonos and Hyperion suggest that the atmospheric correction scheme was able to yield water reflectance with small errors. This in turn means that the path reflectance due to aerosol and molecular scattering has been derived correctly.

From the Hyperion imagery other optical properties such as scattering transmittance and aerosol model was derived by using look-up tables constructed with TAFKAA. This was cross validated with the transmittance obtained from the corrected cloud radiance. The scattering transmittance obtained by fitting method and the total transmittance from using cloud radiance has strong agreement for the spectral range 490-600 nm. There is also agreement between the total transmittance derived from cloud radiance and computed gaseous transmittance for wavelengths

greater than 700 nm. This suggest the validity of these two approaches to retrieve optical properties of the atmosphere.

SWIM was implemented on the three different datasets. The experimental dataset was sampled around the region of interest where waters of high absorption and backscattering coefficients are present. The absorption coefficients measured by the in-situ suggests that it is dominated by CDOM, evident from the exponential spectral behavior. Further analysis by decomposing the measured absorption into the various absorption constituents of CDOM and phytoplankton concurred this point. The fitted spectral slope S suggests that the CDOM was from a common source. The value of S for P.Semkau is 0.0153 $\pm$ 0.0003 and P.Hantu 0.0150 $\pm$ 0.0003. The backscattering coefficients estimated from the total scattering coefficients were also fitted to the power law function that is used to describe the coefficients over the spectral wavelengths. The parameter Y was found to be 0.407 $\pm$ 0.100 and 0.557 $\pm$ 0.09 for P. Hantu and P. Semakau.

SWIM was able to retrieve IOPS from the field measured reflectance with small errors. MIM was also used on the same dataset and the errors between the methods are comparable. However the errors for retrieved backscattering coefficients are larger. This could be attributed to the fact that the coefficients were estimated from the total scattering coefficients derived from the attenuation and absorption coefficients from field measurements. The error incurred by SWIM for absorption at 676 nm is 0.256, which is much higher than other wavelengths. This was probably due to the high water absorption and low field measured absorption at this band. The range of absorption in this band is from 0.01 to 0.10 m^{-1} while the precision of the Ac-9 is 0.01 m^{-1}. This could partly explain the larger errors incurred at this band.

The results from the simulated dataset further demonstrate that the algorithm was able to retrieve the IOPs over the visible spectral range with small RMSE errors incurred in spite of omitting the spectral window around the green wavelength. The RMSE for $a_{total}(\lambda)$ at 440 nm is 0.111 compared to 0.140 (Wang et al., 2005) and 0.106 (Hoge & Lyon, 1996) for the other two matrix inversion method.

The algorithm was also applied to atmospherically corrected Hyperion data. The cloud and shadow method was used to correct the Hyperion data. As there were no in-situ data dated back to 2001, the retrieved IOPs were used as input for HYDROLIGHT to perform forward simulations of the reflectance. The reflectance was used to compare with the corrected reflectance. The RMSE between the HYDROLIGHT reflectance and atmospherically corrected Hyperion data is less than 0.2 for wavelengths between 410-560 nm.

Based on all the results it is concluded that that SWIM is able to retrieve IOPs from remote sensing reflectance. The next question is how does it fare over shallow waters. SWIM was compared to MIM where the green band was not omitted. Firstly, the errors of IOPs retrieved over the different depths which was measured by a sonar was compared. The results show that SWIM outperformed MIM for depths less than 3.5 m. SWIM and MIM was also applied to simulated data with field measured IOPs as input, in this case the set of IOPs which represent the clearest water sampled was chosen. The depth was varied together with different bottom reflectance. The results showed that SWIM outperformed MIM for most cases especially when $\psi(\lambda, H)$ is large, which is an indicator of the influence of the sea bottom.

The cloud and shadow atmospheric correction was implemented on two different sensors and possibly on other satellite sensors for future work. The implementation of the correction scheme was made as generic as possible such that it can be used for other sensors. Moreover this scheme was designed in mind for the implementation on satellite sensors that do not have excellent radiometric calibration. This opened up another avenue for more satellite imageries to be used for ocean colour remote sensing. SWIM can also be implemented on hyperspectral imagery as shown and can also be adapted for use in other sensors. However this is limited by the fact that a minimum number of spectral bands are needed for SWIM to work.

Bibliography

Ahmad Z., Fraser R., 1982, An Iterative Radiative Transfer Code For Ocean-Atmosphere Systems, Journal of the Atmospheric Sciences, **39**, Nr. 3, 656–665

Albert A., Mobley C.D., 2003, An analytical model for subsurface irradiance and remote sensing reflectance in deep and shallow case-2 waters, Optics. Express., **37**, 2873 – 2890

Austin R.W., "Inherent spectral radiance signatures of the ocean surface, Ocean Color Analysis " , (Final technical Report, S.Q. Duntley,ed., SIO Ref.74-10, Scripps Instituion of Oceanography, La Jolla, Calif., 1974)

Baker K., Smith R., 1982, Bio-Optical Classification and Model of Natural Waters. 2, Limnology and Oceanography, **27**, Nr. 3, 500–509

Berk A., Bernstein L., Robertson D., et al., Modtran: A Moderate Resolution Model for LOWTRAN 7 (Air Force Geophysics Laboratory, Air Force Systems Command, US Air Force, 1987)

Bricaud A., Morel A., Prieur L., 1981, Absorption by dissolved organic matter of the sea (yellow substance) in the UV and visble domains, Limnol. Oceanogr., **26**, 43–53

Carder K., Chen F., Lee Z., Hawes S., Kamykowski D., 1999, Semianalytic Moderate-Resolution Imaging Spectrometer algorithms for chlorophyll a and absorption with bio-optical domains based on nitrate-depletion temperatures, Journal of Geophysical Research, **104**, Nr. C3, 5403–5422

Carder K., Hawes S., Baker K., Smith R., Steward R., Mitchell B., 1991, Reflectance model for quantifying chlorophyll a in the presence of productivity degradation products, Journal of Geophysical Research, **96**, Nr. C11, 20599–20611

Carder K., Steward R., 1985, A Remote-Sensing Reflectance Model of a Red-Tide Dinoflagellate Off West Florida, Limnology and Oceanography, **30**, 286–298

Carder K., Steward R., Harvey G., Ortner P., 1989, Marine Humic and Fulvic Acids: Their Effects on Remote Sensing of Ocean Chlorophyll, Limnology and Oceanography, **34**, Nr. 1, 68–81

Clarke G., Ewing G., Lorenzen C., 1970, Spectra of Backscattered Light from the Sea Obtained from Aircraft as a Measure of Chlorophyll Concentration, Science, **167**, Nr. 3921, 1119

Davis C., Bowles J., Leathers R., Korwan D., Downes T., Snyder W., Rhea W., Chen W., Fisher J., Bissett P., et al., 2002, Ocean PHILLS hyperspectral imager: design, characterization, and calibration, Optics Express, **10**, Nr. 4, 210–221

Deschamps P., Herman M., Tanre D., 1983, Modeling of the atmospheric effects and its application to the remote sensing of ocean color, Appl. Opt, **22**, Nr. 23, 3751–3758

Doerffer R., Heymann K., Schiller H., 2002, Case 2 Water Algorithm for the medium resolution imaging spectrometer Meris on Envisat, ESA report ENVISAT validation workshop

Fougnie B., Frouin R., Lecomte P., Deschamps P., 1999, Reduction of skylight reflection effects in the above-water measurement of diffuse marine reflectance, Appl. Opt, **38**, 3844–3856

Fry E., Kattawar G., Pope R., 1992, Integrating cavity absorption meter, Appl. Opt, **31**, 2055–2065

Gao B., Davis C., 1997, Development of a line-by-line-based atmosphere removal algorithm for airborne and spaceborne imaging spectrometers, Proc. SPIE, **3118**, 132–141

Gao B., Heidebrecht K., Goetz A., 1993, Derivation of scaled surface reflectances from AVIRIS data., Remote Sensing of Environment, **44**, Nr. 2, 165–178

—, 1997, Atmosphere Removal Program (ATREM) Version 3.0 User's Guide, Center for the Study of Earth from Space, University of Colorado at Boulder, S. 1–27

Gao B., Montes M., Ahmad Z., Davis C., 2000, Atmospheric correction algorithm for hyperspectral remote sensing of ocean color from space, Appl. Opt, **39**, Nr. 6, 887–896

Gordon H., 1978, Removal of atmospheric effects from satellite imagery of the oceans, Applied Optics, **17**, Nr. 10, 1631–1636

—, 1987, Calibration requirements and methodology for remote sensors viewing the ocean in the visible, Remote Sensing of Environment, **22**, 103–126

Gordon H., Brown J., Evans R., 1988, Exact Rayleigh scattering calculations for use with the Nimbus-7 Coastal Zone Color Scanner, Applied Optics, **27**, Nr. 5, 862–871

Gordon H., Clark D., 1981, Clear water radiances for atmospheric correction of coastal zone color scanner imagery, Applied Optics, **20**, Nr. 24, 4175–4179

Gordon H., Morel A., 1983, Remote Assessment of Ocean Color for Interpretation of Satellite Visible Imagery: A Review Springer-Verlag, New York

Gordon H., Wang M., 1992, Surface roughness considerations for atmospheric correction of ocean color sensors. 1: The Rayleigh scattering component, Appl. Opt, **31**, Nr. 21, 4247–4260

—, 1994a, Influence of oceanic whitecaps on atmospheric correction of ocean-color sensor, Appl. Opt, **33**, Nr. 33, 7754–7763

—, 1994b, Retrieval of water-leaving radiance and aerosol optical thickness over the oceans with SeaWiFS: a preliminary algorithm, Applied Optics, **33**, Nr. 3, 443–452

Gordon H.R., 1997, Atmospheric correction of ocean color imagery in the Earth Observing System era, J. Geophys. Res., **102**, Nr. 11, 17081–17106

Gordon H.R., Brown O.B., Evans R.H., Smith R.C., Baker K. S.and Clark D.K., 1988, A semi-analytic radiance model of ocean color, J. Geophys. Res., **93**, 10,909–10,924

Hoge F.E., Lyon P.E., 1996, Satellite retrieval of inherent optical properties by linear matrix inversion of oceanic radiance models: an analysis of model and radiance measurement errors, J. Geophys. Res., **101**, 16,631 – 16,648

Hoge F.E., Wright C.W., Lyon P.E., Swift R.N., Yungel J.K., 1999a, Satellite retrieval of inherent optical properties by inversion of an oceanic radiance model: a preliminary algorithm, Appl. Opt., **38**, 495–504

—, 1999b, Satellite retrieval of the absorption coefficient of phytoplankton phycoerythrin pigment: theory and feasibility status, Appl. Opt., **38**, 7431–7441

Højerslev N., Aas E., 2001, Spectral light absorption by yellow substance in the Kattegat-Skagerrak area, Oceanologia, **43**, Nr. 1, 39–60

Hooker S., Zibordi G., Lazin G., McLean S., The SeaBOARR-98 Field Campaign, NASA Tech. Memo.1999- 206892, Vol.3, S.B. Hooker and E.R.Firestone, Eds. (NASA, GSFC, 1999)

Hu C., Carder K., Muller-Karger F., 2000, Atmospheric Correction of SeaWiFS Imagery over Turbid Coastal Waters: A Practical Method, Remote Sensing of Environment, **74**, Nr. 2, 195–206

Jin Z., Charlock T., Rutledge K., Stamnes K., Wang Y., 2006, Analytical solution of radiative transfer in the coupled atmosphere-ocean system with a rough surface, Applied Optics, **45**, Nr. 28, 7443–7455

Kaufman Y., Gao B., 1992, Remote sensing of water vapor in the near IR from EOS/MODIS, Geoscience and Remote Sensing, IEEE Transactions on, **30**, Nr. 5, 871–884

Kirk J., 1992, Monte Carlo modeling of the performance of a reflective tube absorption meter, Appl. Opt, **31**, Nr. 30, 6463–6468

Koepke P., 1984, Effective reflectance of oceanic whitecaps, Applied Optics, **23**, 1816–1823

Lee Z., Remote Sensing of Inherent Optical Properties: Fundamental, Tests of Algorithms and Applications, reports of the International Ocean-Colour Coordinating Group (Dartmouth, Nova Scotia, Canada, 2005)

Lee Z., Carder K., 2001, Particle phase function and remote-sensing reflectance model: a revisit, Ocean Color Research Team Meeting, San Diego, Calif., May, S. 21–24

Lee Z., Carder K., Steward R., Peacock T., Davis C., Mueller J., 1997, Remote sensing reflectance and inherent optical properties of oceanic waters derived from above-water measurements, Proceedings of SPIE, **2963**, 160

Lee Z., Hu C., 2006, Global distribution of Case-1 waters: An analysis from SeaWiFS measurements, Remote Sensing of Environment, **101**, 270–276

Lee Z.P., "Visible-infrared remote-sensing model and application for ocean waters " , Ph.D dissertation (Department of Marine Science, Univertsity of South Florida, St. Petersburg, Fla., 1994)

Lee Z.P., Carder K.L., Arnone R.A., 2002, Deriving Inherent Optical Properties from Water Color: a Multiband Quasi-Analytical Algorithm for Optically Deep Waters, Appl. Opt., **41**, 5755–5772

Lee Z.P., Carder K.L., mobley C.D., steward R.G., Patch J.S., 1998a, Hyperspectral Remote Sensing for Shallow Waters. 1. A Semianalytical Model, Appl. Opt., **37**, 6329–6338

—, 1998b, Hyperspectral Remote Sensing for Shallow Waters. 2. A Semianalytical Model, Appl. Opt., **37**, 6329–6338

Lee Z.P., Carder K.L., Steve K., Steward R.G., Peacock T.G., Curtiss O.D., 1994, Model for interpretation of hyperspectral remote-sensing reflectance, Appl. Opt., **33**, 5721–5732

Loisel H., Stramski D., 2000, Estimation of the inherent optical properties of natural waters from

the irradiance attenuation coefficient and reflectance in the presence of Raman scattering, Appl. Opt, **39**, 3001–3011

Maritorena S., Andre M., Gentili B., 1994, Diffuse Reflectance of Oceanic Shallow Waters:Influence of Water Depth, Limnol. Oceanogr., **39**, 1689–1703

Maritorena S., Siegel D., Peterson A., 2002, Optimization of a semianalytical ocean color model for global-scale applications, Applied Optics, **41**, Nr. 15, 2705–2714

McClatchey R., et al., Optical Properties of the Atmosphere (Air Force Systems Command, United States Air Force; Distributed by National Technical Information Service, 1972)

Mobley C.D., Light and Water:Radiative Tranfer in Natural Waters (Academic, New York, 1994)

—, Hydrolight 3.0 User's Guide, Final Report (SRI International, Menlo Park, Calif, 1995)

—, 1999, Estimation of the remote-sensing reflectance from above-surface measurements, Appl. Opt., **38**, 7442–7455

Mobley C.D., Sundman L.K., Davis C.O., Bowles J.H., Downes T.V., Leathers R.A., Montes M.J., Bissett W.P., David D., Kohler R., Reid R.P., Louchard E.M., Gleason A., 2005, Interpretation of hyperspectral remote-sensing imagery by spectrum matching and look-up tables, Appl. Opt., **44**, 3576–3592

Montes M., Gao B., Davis C., 2003, Tafkaa atmospheric correction of hyperspectral data, Proceedings of SPIE, **5159**, 188–197

Morel A., Bricaud A., 1981, Theoretical results concerning light absorption in a discrete

medium, and application to specific absorption of phytoplankton, Deep-Sea Res, **28**, 1375–1393

Morel A., Gentili B., 1993, Diffuse reflectance of oceanic waters. II. Bidirectional aspects, Appl. Opt, **32**, Nr. 33, 6864–6879

Morel A., Maritorena S., 2001, Bio-optical properties of oceanic waters- A reappraisal, Journal of Geophysical Research, **106**, Nr. 7, 163–7

Morel A., Prieur, 1977, Analysis of variations in ocean color, Limnol. Oceanogr., **22**, 709–722

Morel A., Prieur L., 1997, Analysis of variations in ocean color, Laser Optoelektron., **36**, 8710–8723

Mueller J., Fargion G., McClain C., Ocean Optics Protocols for Satellite Ocean Color Sensor Validation, Revision 4, Volume IV: Inherent Optical Properties: Instruments, Characterizations, Field Measurements and Data Analysis Protocols (NASA Goddard Space Flight Center, Greenbelt, Md., 2002)

Mueller J.L., Austin R.W., Ocean optics protocols for SeaWiFS validation, revision 1, SeaWiFS Technical Report Series, Vol. 25 (Vol. 25, NASA Tech. Memo. 104566, S. B. Hooker, E. R. Firestone, and J. G. Acker, eds. National Technical Information Service, Springfield, Va., 1995)

Mueller J.L., Morel A., Frouin R., Davis C., Arnone R., Carder K.L., Lee Z.P., Hooker H.S., Mobley C.D., McLean S., Holben B., Miller M., Pietras C., Knobelpiesse K.D., Fargion G.S., Porter J., Voss K., "Ocean Optics Protocols for Satellite Ocean Color Sensor Validation, Rev.

4, SeaWiFS Tech. Rep. Ser., NASA Tech. Memo. 2003-21621, Vol. 3," (NASA Goddard Space Flight Center, Greenbelt, Md., 2003)

Mustard J., Staid M., Fripp W., 2001, A Semianalytical Approach to the Calibration of AVIRIS Data to Reflectance over Water-Application in a Temperate Estuary, Remote Sensing of Environment, **75**, Nr. 3, 335–349

O'Reilly J., Maritorena S., Mitchell B., Kahru M., Siegel D., Carder K., Garver S., McClain C., 1998, Ocean color chlorophyll algorithms for SeaWiFS, Journal of Geophysical Research, **103**, Nr. 24, 937–24

Pegau W., Gray D., Zaneveld J., 1997, Absorption and attenuation of visible and near-infrared light in water: dependence on temperature and salinity, Appl. Opt, **36**, Nr. 24, 6035–6046

Pegau W., Zaneveld J., 1993, Temperature-Dependent Absorption of Water in the Red and Near-Infrared Portions of the Spectrum, Limnology and Oceanography, **38**, Nr. 1, 188–192

Peterson B., 2001, IKONOS relative spectral response and radiometric calibration coefficients, Document number SE-REF-016, Revision A. Space Imaging, Thornton, CO

Petzold T., 1972, Volume scattering functions for selected ocean waters, SIO Ref, S. 72–78

Pope R.M., Fry E.S., 1997, Absorption spectrum (380-700 nm) of pure water. II. Integrating cavity measurements, Appl. Opt., **36**, 8710–8723

Preisendorfer R., Hydrologic Optics (US Dept. of Commerce, National Oceanic and Atmospheric Administration, Environmental Research Laboratories, Pacific Marine Environmental Laboratory, 1976)

Prieur L., Sathyendranath S., 1981, An Optical Classification of Coastal and Oceanic Waters Based on the Specific Spectral Absorption Curves of Phytoplankton Pigments, Dissolved Organic Matter, and Other Particulate Materials, Limnology and Oceanography, **26**, Nr. 4, 671–689

Reinersman P., Carder K., Chen F., 1998, Satellite-Sensor Calibration Verification With the Cloud-Shadow Method, Applied Optics, **37**, Nr. 24, 5541–5549

Roesler C., Perry M., Carder K., 1989, Modeling in Situ Phytoplankton Absorption from Total Absorption Spectra in Productive Inland Marine Waters, Limnology and Oceanography, **34**, Nr. 8, 1510–1523

Rothman L., Jacquemart D., Barbe A., Chris Benner D., Birk M., Brown L., Carleer M., Chackerian C., Chance K., Coudert L., et al., 2005, The HITRAN 2004 molecular spectroscopic database, Journal of Quantitative Spectroscopy and Radiative Transfer, **96**, Nr. 2, 139–204

Sathyendranath S., Arnone R., Remote Sensing of Ocean Colour in Coastal, and Other Optically-complex Waters: Report of an IOCCG Workshop Held in Ispra, Italy (14-18 June, 1999)...[et Al.] (IOCCG, 2000)

Sathyendranath S., Platt T., 1997, Analytic model of ocean color, Appl. Opt, **36**, 2620–2629

Shettle E., Fenn R., 1979, Models of aerosols of lower troposphere and the effect of humidity variations on their optical properties, US Air Force Cambridge Res. Lab. Tech. Rep., AFCRL-TR 79, **214**, 100

Shettle E.P., Fenn R.W., 1979, Models for the aerosols of the lower atmosphere and the effects

of humidity variations on their optical properties., AFGL-TR-79-0214 (Air Force Geophysics Laboratory, Hanscomb Airforce base, Mass.)

Siegel D., Wang M., Maritorena S., Robinson W., 2000, Atmospheric correction of satellite ocean color imagery: the black pixel assumption, Appl. Opt, **39**, Nr. 21, 3582–3591

Sogandares F., Fry E., 1997, Absorption spectrum 340–640 nm of pure water. I. Photothermal measurements, Appl. Opt, **36**, Nr. 33, 8699–8709

Sydor M., Arnone R., 1997, Effect of suspended particulate and dissolved organic matter on remote sensing of coastal and riverine waters, Appl. Opt, **36**, 6905–6912

Sydor M., Arnone R., Gould Jr R., Terrie G., Ladner S., Wood C., 1998, Remote-sensing technique for determination of the volume absorption coefficient of turbid water, Appl. Opt, **37**, 4944–4950

Van Zee H., Hankins D., 2002, C. deLespinasse, 2002: ac-9 Protocol Document (Revision F)

Vermote E., Tanre D., 1992, Analytical expressions for radiative properties of planar Rayleigh scattering media, including polarization contributions, Journal of Quantitative Spectroscopy & Radiative Transfer, **47**, Nr. 4, 305–314

Vermote E., Tanre D., Deuze J., Herman M., Morcette J., 1997, Second Simulation of the Satellite Signal in the Solar Spectrum, 6S: an overview, Geoscience and Remote Sensing, IEEE Transactions on, **35**, Nr. 3, 675–686

Wang P., Boss E., Roesler C., 2005, Uncertainties of inherent optical properties obtained from semianalytical inversions of ocean color, Appl. Opt., **44**, Nr. 19, 4074–4085

Werdell P., Bailey S., 2005, An improved in-situ bio-optical data set for ocean color algorithm development and satellite data product validation, Remote Sensing of Environment, **98**, Nr. 1, 122–140

Zaneveld J., Kitchen J., Bricaud A., Moore C., 1992, Analysis of in-situ spectral absorption meter data, Proceedings of SPIE, **1750**, 187

Zaneveld J., Kitchen J., Moore C., 2003, Scattering error correction of reflection-tube absorption meters, Proceedings of SPIE, **2258**, 44

Zepp R., Schlotzhauer P., 1981, Comparison of photochemical behavior of various humic substances in water: III. Spectroscopic properties of humic substances, Chemosphere, **10**, Nr. 5, 479–486

Appendix A

Processing AC-9 data

At each measured depth, the live data of absorption and attenuation can be observed on screen using the interface program,WETVIEW. As seen in Figure A.1(a) and Figure A.1(b) , on the Y-axis is time, and the X-axis shows the attenuation and absorption. The real time data serves as a good guide to see if there is any problem during acquirsition. Figure A.1(b) shows the case where the data from the AC-9 is noisy and a re-acquisition had to be performed again. From the experience gained from the numerous field trips, when there were passing crafts,strong tidal current, noise shown in Figure A.1(b) was experienced. Similar situation was also experienced when the bottom depth was less then 2 m, indicating that there might be influx of sand particles stirred up by the engine. Usually the sediment was allowed to settle after the ship was anchored for measurements.

The data that is streamed into the laptop via the WETVIEW program is processed and exported to ASCII format. The absorption and attenuation data has to be first corrected for both temperature and salinity effects (Van Zee & Hankins, 2002). In particular the absorption channel

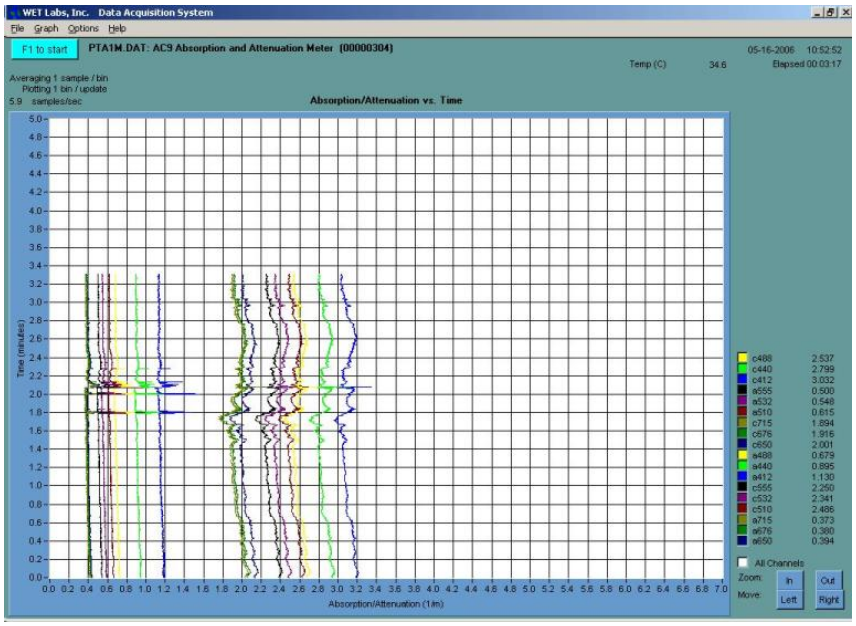

(a) Shows relatively good and noise free data

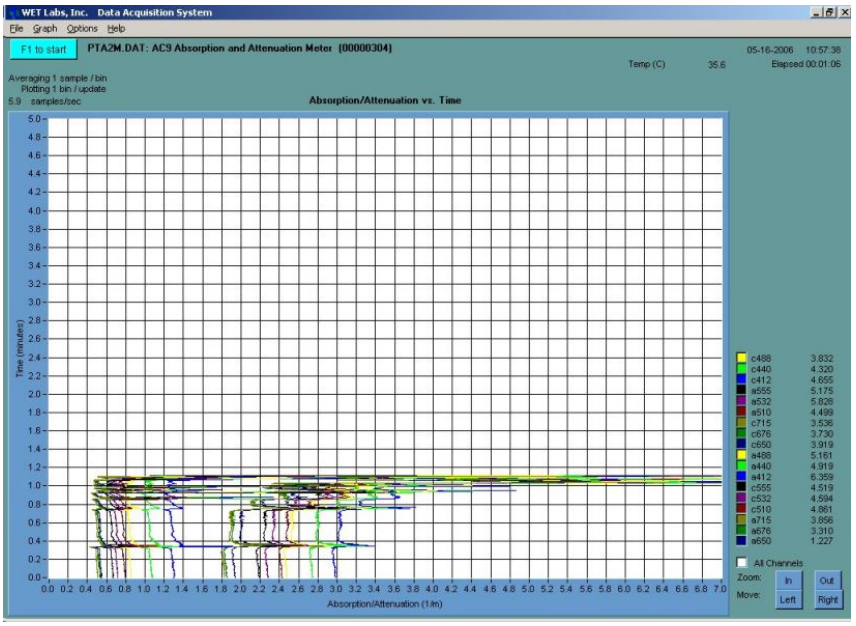

(b) Shows noisy data

FIGURE A.1: Wetview program used to acquire absorption and attenuation data

has to be corrected for scattering effects. The scattering effects are attributed to light being scattered out of path while travelling from the transmitter optics to the detectors. This results in the overestimation of the absorption and requires the correction of the scattering effects due to

suspended particles (Zaneveld et al., 2003) in the curvettes.

The absorption and attenuation channel has to be corrected for temperature difference between blank water reference used to calibrate the AC-9. Also salinity effects has to be corrected. The channels are corrected using the equations below.

$$a_c(\lambda) = a_m(\lambda) - [\psi_t(\lambda)(t - t_r) + \psi_s^a(\lambda)S(\lambda)] \tag{A.1}$$

$$C_c(\lambda) = C_m(\lambda) - [\psi_t(\lambda)(t - t_r) + \psi_s^c(\lambda)S(\lambda)] \tag{A.2}$$

where $a_m(\lambda)$,$C_m(\lambda)$ are measured absorption and attenuation , $a_c(\lambda)$ and $C_c(\lambda)$ are the corrected optical quantities respectively . The equations embodied the effect of temperature and salinty differene between the sea water sampled and the blank(pure water) in the lab for calibration.Salinity and temperature was measured with a refractometer and a sonar sensor that measures the skin temperature of water. The values for correcting the salinity and temperature effects are given in the Table A.1,

The AC-9 has been designed to minmize any error due to scattering from the transmitter to the in-built detector. The scattering in the absorption tube that measures absorption loses signal due to path elongation. Hence the silver lining surround the absorption tube is made of quartz material which is used to reflect any scattered stray light back into the tube. The detector is also made as large as possible to capture all the scattered light and to minimize the errors in measurements. However this may no be suffcient especially if there is a lot of suspended particles that contribute to optical scattering in the sampled water. Therefore there is still a need

TABLE A.1: Values used for correcting effects due to absorption and salinity (Zaneveld et al., 1992)

Wave (nm)	ψ_t^a	$\psi_S^a(\lambda)$	$\psi_t^c(\lambda)$
412	0.0001	0.00018	0.00007
440	0.0000	0.00008	-0.00007
488	0.0000	0.00008	-0.00007
510	0.0002	0.00009	-0.00007
532	0.0001	0.00004	-0.00008
555	0.0001	0.00008	-0.00008
650	-0.0001	0.00011	-0.00005
676	-0.0001	0.00008	-0.00007
715	0.0029	-0.00018	-0.00032

to correct for the error due to particulate scattering that was not handled by the inherent design of the absorption tube. The main assumption used in correcting for the scattering effect due to suspended particles in the absorption tube is that the absorption of bio-optical consituients is zero at the 715 nm channel and the shape of the volume scattering function does not vary with wavelength. If the volume scattering function is not constant with wavelength, the scattering effects of due to the suspended particles in the tube will not be constant with wavelength.The corrected absorption can be written (Zaneveld et al., 1992) as ,

$$a_c(\lambda) = a_m(\lambda) - \frac{a_m(715)}{C_m(715) - a_m(715)} \left[C_m(\lambda) - a_m(\lambda)\right] \tag{A.3}$$

The term $\frac{a_m(715)}{C_m(715)-a_m(715)}$ gives the fraction of the total scattering to be deducted from the ab-

sorption channel. The minimum value for this value is given to be 0.07 by (Kirk, 1992) from Monte Carlo simulations. For the waters that was investigated, the value was close to 0.22, however some co-workers in the field has reported it to be 0.18 (Mueller et al., 2002) for suspended sediment dominated waters.

Before any correction was done to the measured absorption and attenuation, some processing was done to pick up any outliers by simple statistical methods as the raw data of absorption and attenuation are often plaqued with noise either by fluxes of suspended particles or noise induced as the instrument was lowered to different depths. Then the correction described in Eq.(A.3) was applied.

Appendix B

Discussion of challenges faced in field measurements

Field measurements of the IOPs and radiometric measurements were performed using small vessels, hence easily subjected to harsh environmental conditions. One of the challenges that was faced during the measurements was the strong tidal currents which dragged the Ac-9 cage, subtending it at an angle to the surface of the water. In such cases, the sampling was halted as the cage could get trapped and not be recoverable. Moreover the strong flow of the tidal streams causes a lot of noise in the data. There were instances where the attenuation data jumps from 3-4 m^{-1} to 10 m^{-1}. Such similar occurrences were also due to the 10 cm curvette being slightly dislodged from place hence the need to check the live feed of data constantly.

Another challenge was the fast changing sky conditions where a thunderstorm would be at the horizon in a time span difference of a few hours. Passing clouds also pose a great challenge in making radiometric measurements since the downwelling light will change dramatically as

cloud-cover changes rapidly with time. This affects the measurements made with the white reflectance board and that of the sky since clouds are highly reflective. The high variance of downweliing light was overcome by taking as many spectrums over one point as possible.

Measurements made with the ac-9 were also plagued with noise when the environment was not favorable. It was observed that with either a passing vessels or strong tidal current,the data obtained is usually noisy and many times the sampling has to be given up. For shallow waters, it was observed that the attenuation data was extremely noisy, which, could be indicative of sediment being stirred up when the sampling vessel entered into the vicinity.

In order to resolve this, sampling was done after the sediment which is stirred up by our sampling vessel was allowed to settle down. Extra care was also taken to ensure both the ac-9 cage was not touching the bottom and the water inlet is not facing the sea bottom. This is to avoid suspended sediments from the seabed from entering into the Ac-9.

For typical ac-9 measurements, there were spikes in the attenuation data. As such, simple statistical method has to be applied to the data by filtering out these spikes by setting a standard deviation of 0.005 m^{-1} which is the precision of the Ac-9. The standard deviation was computed based on binning data into intervals of 6 secs. From which, data which differs more than 0.01 $m-^{1}$ for each binned data were removed. The value of 0.01 m^{-1} is the accuracy of the Ac-9. As seen from Figure B.1, the spikes in the data were removed by simple statistical selection described previously. However there were situations where the spikes and noise overwhelmed the data thus making them unusable. As such, it is diffcult and time consuming to obtain to

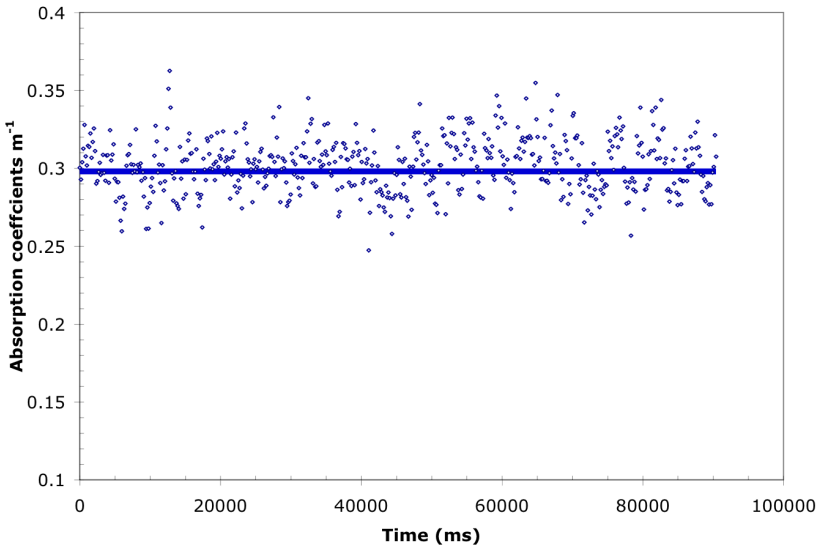

FIGURE B.1: Noise in absorption channel 412 nm, with spikes

obtain good in-situ and radiometric data.

All the precations taken during field trip have allowed a good number of field data for algorithm validation, which is about 25 points in this case . Special care in making measurements of IOPs has reduced the noise in data especially halting the measurements when strong tidal current is prevalent or heavy shipping traffic.